Ultrafast fluorescence of photosynthetic crystals and light-harvesting complexes

Promotor:
Prof. dr. H. van Amerongen
Hoogleraar Biofysica
Wageningen Universiteit, Nederland

Copromotor:
Dr. A.V. Ruban
Lecturer in Biological Chemistry
Queen Mary University of London, United Kingdom

Promotiecommissie:
Prof. dr. R. van Grondelle (Vrije Universiteit, Nederland)
Prof. dr. J.T. Zuilhof (Wageningen Universiteit, Nederland)
Dr. H.J. van Gorkom (Universiteit Leiden, Nederland)
Prof. Dr. A.R. Holzwarth (Max Planck Institute for Bioinorganic Chemistry, Germany)

Dit onderzoek is uitgevoerd binnen de onderzoeksschool EPS.

Ultrafast fluorescence of photosynthetic crystals and light-harvesting complexes

Bart van Oort

Proefschrift
ter verkrijging van de graad van doctor
op gezag van de rector magnificus
van Wageningen Universiteit,
Prof.dr. M.J. Kropff,
in het openbaar te verdedigen
op dinsdag 28 oktober 2008
de namiddags te half twee in de Aula

Bart van Oort, 2008
Ultrafast fluorescence of photosynthetic crystals and light-harvesting complexes

PhD thesis, Wageningen Universiteit, The Netherlands
met een samenvatting in het Nederlands

ISBN: 978-90-8585-205-6

hoppa!

Contents

	Abbreviations	
Chapter 1	Introduction	1
Chapter 2	(Sub)-Picosecond spectral evolution of fluorescence studied with a synchroscan streak-camera system and target analysis	25
Chapter 3	Ultrafast resonance energy transfer from a site-specifically attached fluorescent chromophore reveals the folding of the N-terminal domain of CP29	51
Chapter 4	Aggregation of Light-Harvesting Complex II leads to formation of efficient excitation energy traps in monomeric and trimeric complexes	69
Chapter 5	Equilibrium between quenched and nonquenched conformations of the major plant light-harvesting complex studied with high-pressure time-resolved fluorescence	81
Chapter 6	Picosecond fluorescence of intact and dissolved PSI-LHCI crystals	99
Chapter 7	Summarizing discussion	127
Chapter 8	Nederlandse samenvatting	139
	Acknowledgements	146
	List of publications	148
	Curriculum Vitae	149
	Education Statement of the Graduate School Experimental Plant Sciences	150

Abbreviations

[4Fe4S]	iron sulfur cluster
ADC	analogue-digital converter
Ant	antheraxanthin
apo-4/40/97	apoprotein of CP29 mutant 4/40/97, labeled with TAMRA
ATP	adenosine triphosphate
ADP	adenosine diphosphate
CFD	constant fraction discriminator
Car	carotenoid
Chl	chorophyll
CP24/26/29/43/47	chlorophyll binding protein with apparent molecular mass 24/26/29/43/47 kDa
CP29-4/40/97	CP29 mutant 4/40/97, reconstituted with pigments, and labeled with TAMRA
Cyt b_6f	Cytochrome b_6f
DAS	decay associated spectrum/spectra
DM	dodecyl β-D-maltoside
EAS	evolution associated spectrum
EET	excitation energy transfer
EM	electron microscopy
EPR	electron paramagnetic resonance
Fd	ferrodoxin
fwhm	full width at half maximum
FNR	ferrodoxin $NADP^+$ reductase
FLIM	fluorescence lifetime imaging microscopy
FRET	Förster resonance energy transfer
IRF	instrument response function
HPSEC	high performance size exclusion chromatography
IsiA	iron (limitation) stress induced protein A
LHC	Light Harvesting Complex
LHCI	Light Harvesting Complex I
LHCII	Light Harvesting Complex II
MA	magic angle
MCP	microchannel plate photomultiplier
$NADP^+$	nicotinamide adenine dinucleotide phosphate (oxidized form)
NADPH	nicotinamide adenine dinucleotide phosphate (reduced form)

NPQ	nonphotochemical quenching
PCP	peridinin-chlorophyll protein
PQ	plastoquinon
PQH_2	plastoquinol
PC	plastocyanin
PSI	Photosystem I
PSI-LHCI	Photosystem I - Light Harvesting Complex I supercomplex
PSII	Photosystem II
qE	energy dependent quenching
RC	Reaction Center
S/N	signal-to-noise ratio
SAS	species associated spectrum/spectra
SVD	singular value decomposition
TAC	time-to-amplitude converter
TAMRA	6-Carboxy-tetramethyl-rhodamine
TPA	two-photon absorption
TCSPC	time-correlated single photon counting
Xan	xanthophyll
WT	wild type

Chapter 1

General introduction

Background and scope

Sunlight is the main source of energy for life on earth[1]. A crucial step in the use of light-energy is the conversion of this "raw" energy into chemical energy, via a process called photosynthesis. Organisms capable of oxygenic photosynthesis are plants, algae and cyanobacteria. The major sunlight-driven chemical pathway in oxygenic photosynthesis is the production of sugars from carbon-dioxide and water, releasing oxygen as a by-product. The sugars and oxygen can be consumed by other organisms, thereby producing carbon-dioxide and water, which in turn can be used for photosynthesis, and so on, and so on.

Photosynthesis is therefore of paramount importance for the existence of life on earth. Apart from the fundamental significance, a better understanding of structure, organization, function and flexibility of the photosynthetic apparatus may help increase crop yields, plant fitness, and allow mimicking photosynthesis *in vitro*, aiming at energy production. The focus of this thesis is on an adaptative molecular mechanism, which works in photosystem II to protect it against photo-induced damage.

This thesis describes experiments on photosynthetic complexes that are involved in the early steps of photosynthesis. The first chapters describe light-harvesting and photoprotection. These two functions are fulfilled by the same group of pigment-protein complexes (proteins that bind chlorophyll and carotenoid pigments). Under low-light conditions these pigments "harvest light": They absorb the sunlight that drives photosynthesis. In high light intensities they protect the photosynthetic apparatus against photodamage. The switching between these two functions is studied in the first chapters of this thesis. In the chapter 6, intact photosystem I is studied, and the results help to better understand the processes that lead to the initial photochemical reactions of photosynthesis.

The outline of this introduction is as follows: First, in section 1.1 the process of conversion of light-energy into chemical energy is described. The next sections describe the the pigments involved in light-harvesting (section 1.2), and the pigment-protein complexes studied in this thesis (section 1.3). Section 1.4 describes protection against photodamage, and in sections 1.5 and 1.6 the experimental techniques and data analysis used in this thesis are discussed. Finally, section 1.7 contains a short outline of the thesis.

1.1 Oxygenic photosynthesis

1.1.1 Photosynthetic membranes

The first steps of photosynthesis take place in membrane-bound proteins, pigments and electron carriers. In these initial reactions, light-energy is used to produce energy-rich ATP, and the reducing agent NADPH. In subsequent reactions, outside the membranes, ATP and NADPH are used for carbon fixation, i.e. sugar production. All these reactions can be summarized as a single "master" reaction:

$$6H_2O + 6CO_2 \xrightarrow{light} (CH_2O)_6 + 6O_2$$

In most plants and algae, photosynthesis takes place in cell compartments (organelles) named chloroplasts. Most photosynthetic plant cells contain 40-200 chloroplasts, each measuring 3-10 μm.[2] Chloroplasts contain an elaborate network of interconnected photosynthetic membranes, called the thylakoid membrane. Cyanobacteria contain very similar membranes, which supports the theory that chloroplasts descend from a free-living photosynthetic cyanobacterial ancestor[3]. Thylakoid membranes contain highly organized supercomplexes of proteins, pigments and electron carriers. Figure 1 shows schematically the organization of the thylakoid membrane, with the four major supercomplexes, Photosystem II (PSII), Cytochrome b_6f (Cyt b_6f), Photosystem I (PSI) and ATP synthase.

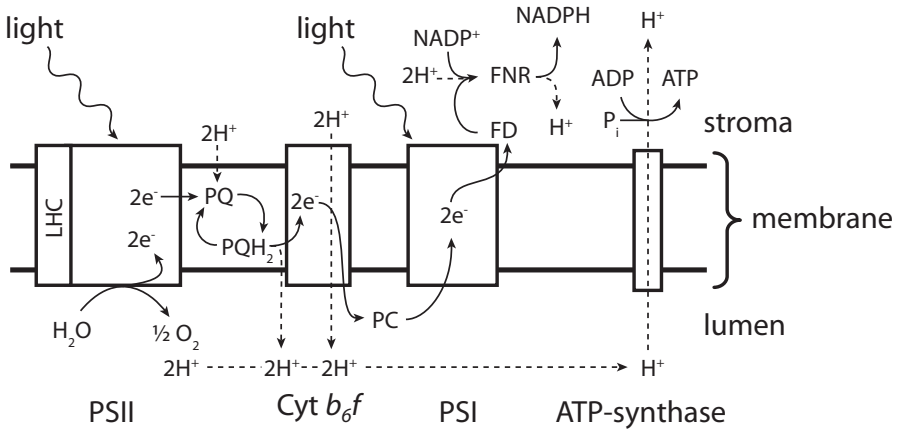

Figure 1. *Simplified model of the first steps of oxygenic photosynthesis, with the four main complexes PSII, Cyt* b_6f*, PSI and ATP synthase, and with the electron (e^-) and proton flows (H^+, dashed lines).*

Figure 1 shows how PSII and PSI work in series to transfer electrons from water to NADPH, and protons from one side of the membrane to the other. Photosynthesis starts with absorption of light-energy by PSII. This energy is used to extract electrons from water, which are then transferred to PSI via several electron carriers (PQ, PQH_2, Cyt b_6f, PC). In PSI additional light-energy is used to drive the electrons to $NADP^+$, via ferrodoxin (Fd) and ferrodoxin-$NADP^+$-reductase (FNR), producing NADPH. The water splitting by PSII produces oxygen and protons, thereby creating a proton gradient across the membrane. This gradient is enlarged during electron transfer, and drives ATP production by ATP-synthase.

ATP and NADPH are used in the Calvin cycle, to produce glyceraldehyde-3-phosphate (G3P: $C_3H_5O_3$-PO_3^{2-}). G3P moves through a series of chemical reactions to form fructose diphosphate, which is used to make glucose, sucrose, starch and other compounds needed by the plant. In this way the "raw" energy of light is converted into chemical energy (ATP and NADPH), and the chemicals that build the plant.

1.1.2 Light-harvesting and charge separation

Before the electron transfer reactions in Figure 1, a chain of events mark the start of photosynthesis: (i) a photon is absorbed, (ii) part of the energy of the absorbed photon is transferred, (iii) the transferred energy is converted into chemical energy. The first step of conversion into chemical energy is charge separation (the photo-induced extraction of an electron from a chlorophyll molecule). Charge separation takes place at a single location in a photosystem, inside a small cluster of pigments and proteins, the reaction centre (RC). The RC is surrounded by large numbers of pigments that "harvest light", thereby increasing the amount of absorbed light. These pigments are organized in light-harvesting pigment-protein complexes (LHCs). Upon absorption of light-energy in the LHCs, the energy can be transferred from pigment to pigment, thus travelling towards the core, and then to the RC. In the RC the energy can be used for charge separation. The resulting electrons are then transferred following the routes shown in Figure 1. Both PSII and PSI contain an RC surrounded by LHCs.

1.2 Light-Harvesting Pigments

The main light-harvesting pigments in plants are chlorophyll (Chl) and a group of compounds called carotenoids (Cars). Algae and cyanobacteria may also contain other light-harvesting pigments, but those pigments are not present in the samples studied in this thesis.

1.2.1 Chlorophyll

Chlorophyll *a* is the primary light-harvesting pigment in oxygenic photosynthesis, and is the site of charge separation. It consists of a tetrapyrrole ring (~1 x 1 nm), that binds a magnesium (Mg) atom in the centre. The long phytol chain attached to the periphery of the ring provides hydrophobicity that aids binding to proteins. Chl *a* further contains a fifth isocyclic ring, and many other structural elements (Figure 2) which may affect the molecule's spectral features. Chlorophyll *b* is a modification of Chl *a*, with one additional keto group (Figure 2).

Chlorophyll *a* and *b* "are green", because they have main absorption bands in the red (~660 nm, low energy) and blue (~450 nm, high energy) regions of the visible spectrum, but hardly absorb green light (~530 nm, intermediate energy). Their absorption spectra are presented in Figure 3. The red-most band represents the Q_y transition to the lowest electronic excited state. The blue band represents Soret transitions to higher excited states. The weaker Q_x transitions around 580-640 nm are partly masked by Q_y vibronic bands. The absorption spectra of Chl *a* and Chl *b* do not completely overlap. Together they cover a bigger part of the solar spectrum, and thereby increase light-harvesting capacity.

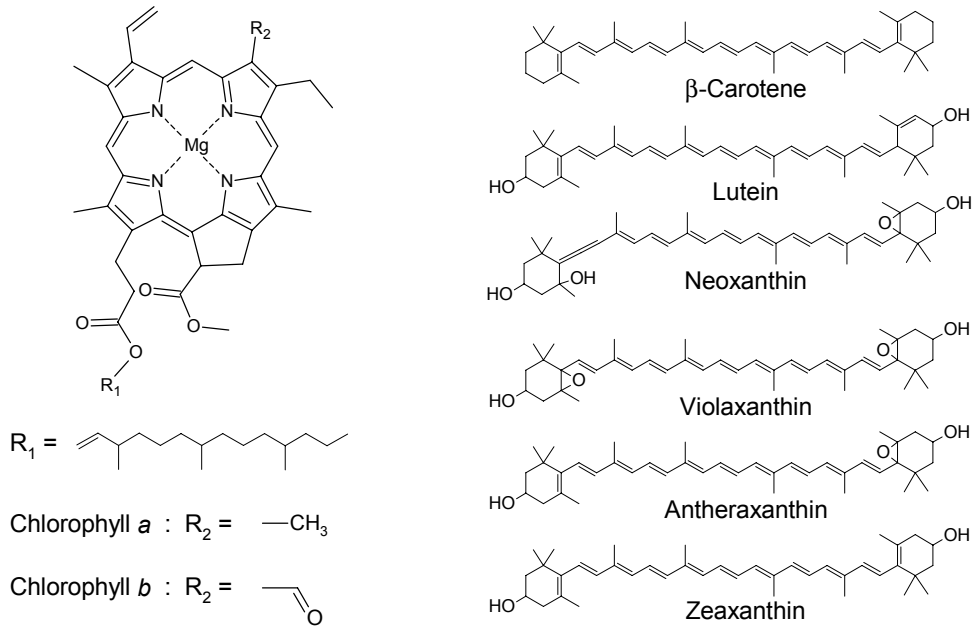

Figure 2. *Chemical structures of photosynthetic pigments: Chlorophylls (left) and carotenoids*

Pigments are influenced by their environment. In *vivo*, Chls are usually bound to specific binding pockets of proteins. The protein influences the spectral properties of Chl both directly and indirectly. Directly, by ligation of the central Mg and the oxygen atoms[4],

by polarity, and by coupling of collective vibrational motions of the protein with the electronic transition[5]. Indirectly, by positioning Chls close together, creating excitonic coupling between nearby Chls[5]. All these interactions can lead to spectral shifts, and a change of absorption and emission line shapes[5], as illustrated by the spectra of PSI-LHCI, PSII core and LHCII in Figure 3. In this thesis such spectral changes are used to gain insight in protein structure and function.

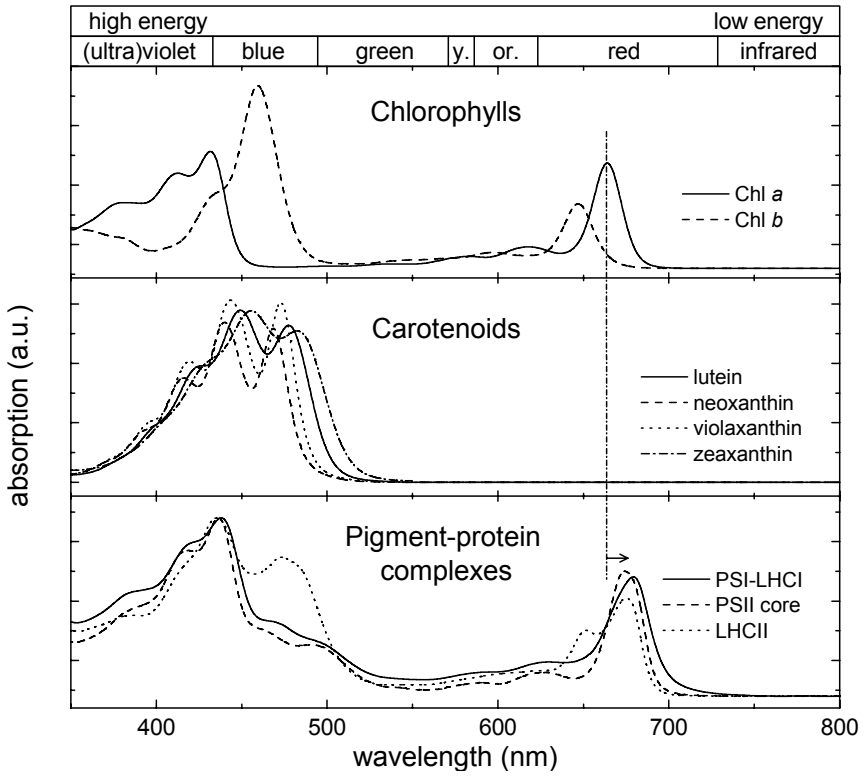

Figure 3. *Visible absorption spectra of photosynthetic pigments in 80% acetone: Chlorophyll a and b (top) and carotenoids (middle); and of photosynthetic complexes in water-based buffer, at room temperature. The vertical dash-dotted line indicates the absorption red-shift of protein-bound Chl relative to Chl in 80% aceton.*

1.2.2 Carotenoids

Carotenoids form another important group of photosynthetic pigments. They consist of a polyene chain of alternating single and double bonds, terminated by two rings (Figure 2). Carotenoids can differ in length, ring type and isomeric form. The pigment-protein complexes studied in this thesis bind two types of carotenoid (Car): (i) xanthophylls (Xan), which contain oxygen; and (ii) carotenes, which consist only of carbon and hydrogen. Xans

are mainly found in light-harvesting complexes, whereas the carotenes are found mainly in the core complexes of PSI and PSII.

The spectroscopic properties of Cars are quite different from those of Chls: For symmetry reasons, the transition from the ground state (S_0) to the first electronic excited state (S_1) is optically forbidden. Therefore the absorption spectrum (Figure 3) only consists of transitions to higher excited states. Car excited-state energy can be transferred to Chl, thereby enlarging light-harvesting capacity. Besides that, Cars serve multiple important functions in photosynthesis: They are essential for assembly and structure stabilization of photosynthetic proteins[6], and for protection against oxidative photodamage[7].

1.2.3 Light absorption and energy transfer

Charge separation takes place the RC of a photosystem. However, most photons are absorbed by pigments outside the RC. After absorption of a photon part of its energy is lost as heat (IC in Figure 8). The remaining energy can be transferred from pigment to pigment; among Chls and from Car to Chl. The pigments are organized in such a way that ultrafast energy transfer to the RC is facilitated. For weakly coupled pigments, energy transfer can be described by the Förster equation[8]:

$$k_{DA} = \frac{9\kappa^2 c^4 \varphi_D}{8\pi n^4 \tau_D R^6} \int \varepsilon_A(\omega) f_D(\omega) \omega^{-4} d\omega \qquad (1)$$

The transfer rate (k_{DA}) from a donor (D) to an acceptor (A) pigment depends on overlap between the normalized fluorescence emission spectrum of the donor (f_D) and absorption spectrum of the acceptor (ε_A), and is inversely related to the centre-to-centre distance (R) between the pigments. The fluorescence emission spectrum of a pigment is generally red-shifted relative to the absorption spectrum. This means that the overlap of absorption and emission is larger for a donor with "blue" absorption (high energy) and an acceptor with "red" absorption (low energy), than *vice versa*. In other words, the Förster equation imposes that energy transfer is mainly energetically downhill: It is faster from a pigment that absorbs more to the blue to a pigment that absorbs more to the red, than *vice versa*. The transfer rate further depends on the relative orientation of the two pigments and their transition dipole moments (κ; the orientation factor), the fluorescence quantum yield of the donor (φ_D), the donor excited state lifetime (τ_D) and the refractive index (n). c is the speed of light in vacuum.

1.3 Pigment-Protein complexes studied in this thesis

1.3.1 Protein structure from X-ray crystallography

Although PSI and PSII have similar macro-organizations, their precise structure, composition and function are quite different. Structural information can be obtained by various types of spectroscopy. One very powerful method involves X-ray diffraction. This method is based on constructive and destructive interference of X-ray waves traveling through an ordered medium. In this case the medium is a crystal of pigment-protein complexes. The X-ray waves traveling through the crystal are scattered by electrons around the atomic nuclei, resulting in a specific interference pattern. From this pattern a three dimensional electron density map can be reconstructed. This is then used to model the mean atomic positions and their chemical bonds. In principle, this method allows atomic resolution, but this is not always achieved, amongst others because of sample heterogeneity, sample dynamics and radiation damage[9]. A major disadvantage of X-ray crystallography is the requirement of crystals. It has turned out to be very complicated to obtain regular crystals of membrane proteins[9]. Thanks to great efforts, the crystal structures of many important photosynthetic proteins have been determined over the last couple of years[10-17].

1.3.2 Photosystem II core

The PSII core complexes of plants and cyanobacteria are very similar[18]. PSII of plants has eluded X-ray crystallography, but the crystal structure of PSII core from the cyanobacterium *Thermosynechococcus elongatus* is shown in Figure 4. It contains two similar proteins (D1 and D2), that together bind the 4 Chl *a* and 2 Pheo *a* of the RC. Two other Chl *a* molecules are at the periphery of D1/D2, and are not involved in charge separation and electron transfer[19]. D1/D2 coordinates the water-splitting manganese cluster and all electron transfer components of PSII. Flanking D1/D2 are the light-harvesting complexes CP43 and CP47. CP43 binds 13 or 14 Chl *a* molecules, and CP47 16 Chl *a* molecules[11,20]. The supercomplex of D1/D2/CP43/CP47 and several smaller subunits[11], is called the PSII core complex, and it naturally occurs as a dimer[21].

One or two Chls in the RC, named P_{680} after their absorption band, function as the primary electron donor. After absorption of one photon, an electron translocates from P_{680} via RC-pigments to an immobilized plastoquinone (PQ), and then to a mobile PQ. In two of these steps PQ is reduced to plastoquinol (PQH_2), and is released into the membrane, and replaced by another PQ. The electron-holes on P_{680} are filled by an electron from a cluster of four manganese ions. With the extraction of four electrons from the manganese cluster, it

oxidizes two water molecules, yielding four electrons, one oxygen molecule and four protons (Figure 1).

1.3.3 Photosystem II light-harvesting complexes

Most of the Chls associated with plant PSII are not bound to the core complex, but to extrinsic light-harvesting complexes (LHCs). PSII core with its extrinsic LHCs form PSII supercomplexes, as described in the next section (see Figure 6). The major LHC is the trimeric LHCII. The high resolution structures from pea[15] (Figure 5), spinach[13] and cucumber[17] are all very similar. Each monomeric unit of LHCII consists of three transmembrane alpha helices and two short amphipathic helices. It binds 8 Chl *a*, 6 Chl *b* and 4 xanthophyll (Xan) molecules. The Chls are orientated roughly perpendicular to the plane of the membrane. They are arranged in two layers parallel to the membrane plane. The 5 Chls *a* and 3 Chls *b* on the stromal side form an elliptical ring, whereas those on the lumenal side form a cluster of 4 Chls and a Chl *a* dimer.

The xanthophylls in LHCII are two luteins (Lut), one neoxanthin (Neo), and one violaxanthin, anteraxanthin or zeaxanthin (Vio, Ant or Zea) (structures in Figure 2, absorption spectra in Figure 3). The two luteins form a transmembrane cross, binding to two helices, which is important for protein stability[13,22]. Unlike all other pigments in LHCII, neoxanthin extends into the membrane. The fourth xanthophyll binding site is occupied by either Vio, Ant or Zea, which are involved in the xanthophyll cycle, playing an important role in photoprotection in plants[23]. This binding site is located at the monomer-monomer interface.

LHCII is connected to the PSII core via the monomeric minor LHCs CP24, CP26 and CP29, which are similar to the LHCII monomer[24]. They each bind 8 to 10 Chls and 2 to 3 Xans[24,25]. The minor light-harvesting complexes may be important for photoprotection[26]. Unfortunately, no crystal structures are available, but they share high sequence homology with LHCII, and therefore LHCII has been used as a template to model their structures (e.g. CP29, ref. 27).

Cyanobacteria and some types of algae do not use the membrane-bound extrinsic light-harvesting complexes, but use water-soluble supercomplexes instead, such as phycobilisomes and peridinin-chlorophyll proteins. These LHCs bind pigments for light-harvesting, and can bind to the membrane surface, where absorbed light-energy can be transferred to PSII and/or PSI.

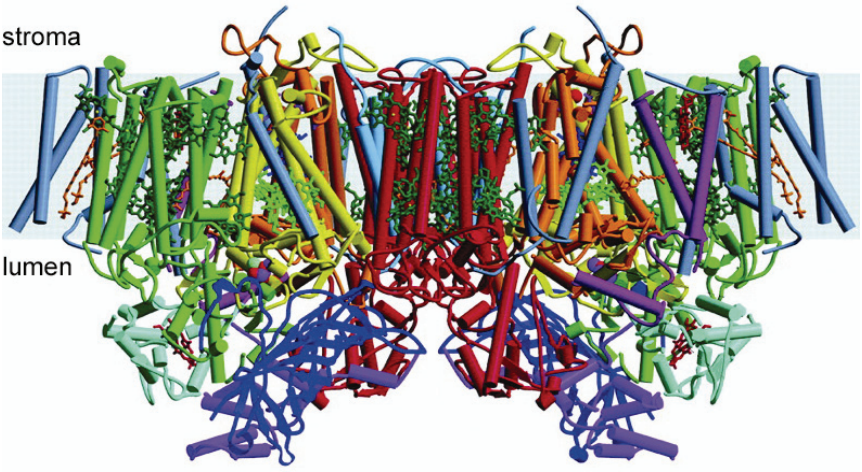

Figure 4. *Structure of PSII core complex of Thermosynechococcus elongatus[11]: Side view through the membrane. Arrangement of protein (ribbons, cylinders and continuous lines) and pigments are indicated.*

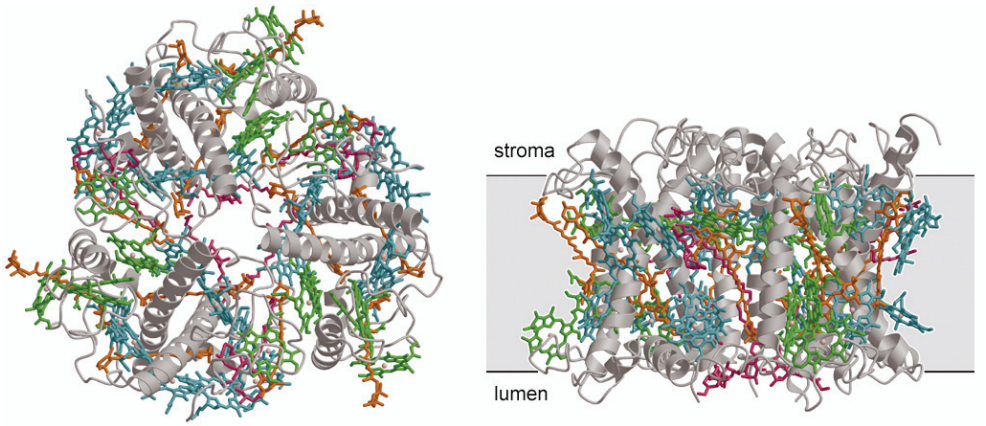

Figure 5. *Structure of LHCII from pea[15]: Top view (left) and side view through the membrane (right). Arrangement of protein (ribbons and continuous lines) and pigments are indicated.*

1.3.4 Photosystem II supercomplex

The PSII supercomplex of plants consists of a core complex, surrounded by several minor light-harvesting complexes (CP24, CP26 and CP29), and one or more major light-harvesting complexes (LHCII)[24]. Structures of cyanobacterial PSII core[11,14] and plant LHCII[13,15,17] are available, but the intact supercomplex has eluded high resolution crystallography. A successful approach to study PSII supercomplex structure, without the need of crystals, turned out to be single particle electron microscopy (EM).

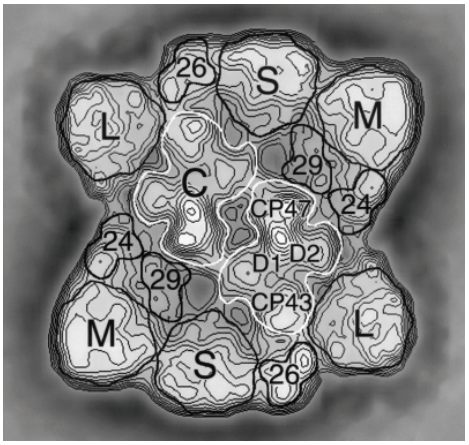

Figure 6. *Model of a top view on the PSII-LHCII supercomplex[28]: The core (C), composed of D1, D2, CP43 and CP47, is surrounded by the minor complexes: CP24, CP26 and CP29. The binding strength of trimeric LHCII at various locations is strong (S), moderate (M) or loose (L).*

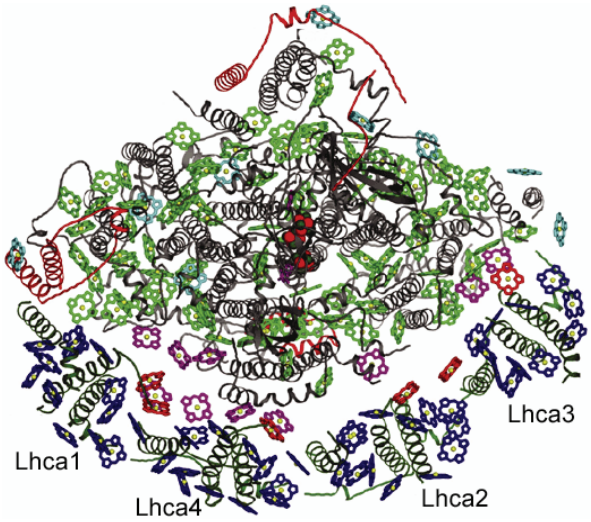

Figure 7. *Structure of PSI-LHCI from pea[1,10]: Top view of the membrane. The arrangement of proteins (ribbons and continuous lines), pigments, and proposed locations of the four types of LHCI (Lhca1-4) are indicated.*

With this approach, PSII membranes are mildly solubilized, and then single PSII particles are measured by EM. The resolution and signal to noise ratio is improved by averaging large numbers of images (typically tens of thousands). This has provided a structural model of the supercomplex[28] (Figure 6). The PSII core (denoted with subunits D1/D2, CP43 and CP47) forms dimers that bind CP24, CP26 and CP29. The number and position of LHCII trimers depends on preparation procedure and may be different for different plant species and growth conditions[21]. They have been named S, M and L, for strong, medium and loosely binding, based on the number of observed supercomplexes with an LHCII at that position, using the mildest preparation method[28]. These supercomplexes can be further organized into megacomplexes, which do not bind LHCII-L, and which are different for different species[21].

1.3.5 Photosystem I supercomplex

The PSI complexes of plants, green algae and cyanobacteria are organized quite differently. In cyanobacteria, PSI is present as monomeric and trimeric core complexes, which can be surrounded by a ring of iron stress-induced (IsiA) light-harvesting complexes[29]. Plants and green algae contain monomeric PSI core complexes. In green algae many copies of Light-Harvesting Complex I (LHCI) bind to the core, thereby extending its light-harvesting capacity[30]. In plants each core consists of 15 proteins, and binds four monomeric LHCI[10]. The total supercomplex is named PSI-LHCI, for which the crystal structure from pea is available at 0.34 nm resolution (Figure 7). The structure of PSI core from cyanobacteria is available at higher resolution[12]. The plant PSI core complex binds ~100 Chls *a*, ~20 Cars (mainly β-carotene), three iron-sulphur clusters, and two phylloquinones[10,12]. The electron transfer chain of the RC is bound between proteins PsaA and PsaB. Analogous to PSII, the primary electron donor P_{700} (absorption at 700 nm), releases an electron upon excitation. This electron is translocated via a Chl *a*, a phylloquinone and the [4Fe4S] clusters to ferrodoxin (Fd). Ferrodoxin $NADP^+$ reductase (FNR) then uses Fd to reduce $NADP^+$ to NADPH (Figure 1). The electrons extracted from P_{700} are replaced by electrons that arrive from PSII, via PQH_2, Cyt b_6f and plastocyanin (PC).

In plants, nine chlorophyll molecules fill the gap between the core and the four LHCI complexes[10]. Each complex is a different pigment-protein complex, named Lhca1 to Lhca4, that binds as dimers Lhca1/4 and Lhca2/3 to specific sites on one side of the core[10]. Together they bind 56 Chls *a* and *b*, and ~10 Cars[10,31]. The structure of LHCI is known at intermediate resolution (0.34 nm) from the PSI-LHCI structure[10], but the structure of LHCII may serve as a template with higher resolution (0.25-0.272 nm[13,15]), because of the high genetic sequence homology of LHCI and LHCII[32].

An important difference between PSI and PSII is the presence of Chls with lower energy than the primary electron donor (P_{700} and P_{680}, respectively) in PSI. These so-called "red Chls" are present both in core and LHCI, although in plants they are mainly associated with LHCI[33]. They compete with P_{700} for energy, thereby significantly affecting PSI's spectral properties, and decreasing the rate of charge separation[30]. Apparently this is a price organisms are willing to pay for the concomitant increase of light-harvesting capacity in shaded leaves under dense canopy[34]. Fluorescence of all Lhca's is red-shifted compared to LHCII, and the minor LHCs of PSII (~680 nm). The extent of the red-shift differs: at 77 K Lhca1 and Lhca2 emit at 701 nm, Lhca3 at 725 nm and Lhca4 at 735 nm[31,35] (note that purification of individual Lhca's has not been achieved yet, and measurements so far were performed on the recombinant proteins).

1.4 Photoprotection

Photosynthetic organisms are highly efficient in capturing light via light-harvesting complexes, and transferring it to reaction centres. However, the involved proteins and pigments can be easily damaged by excess light. The photochemical reactions proceed via high-energy intermediates, and can create highly reactive by-products, which can damage the photosystems[36]. Moreover, when the amount of absorbed light exceeds the capacity of the RCs, the excited state energy resides longer on Chl. This leads to increased intersystem crossing, thereby forming Chl triplet states, which can react with oxygen forming highly reactive singlet oxygen, that can oxidize pigments, proteins and lipids[7]. All these processes together lead to photo-oxidative damage, or, in brief, photodamage. If not repaired, photodamage decreases the efficiency and/or maximum rate of photosynthesis, i.e. it leads to photoinhibition of photosynthetic performance.

Plants have developed several protective mechanisms against photodamage in the course of evolution. These mechanisms range from movement of leaves/cells/chloroplasts, to molecular responses inside chloroplasts. The responses in chloroplasts may be distinguished based on the time scale: (i) Long term responses, which involve *de novo* protein/pigment/lipid production, in order to match the amount of absorbed energy to the RC capacity; (ii) short term responses, which lead to conversion (dissipation) of excited state energy into harmless heat.

The latter processes lead to a decrease of fluorescence from PSII, a phenomenon known as nonphotochemical quenching (NPQ). NPQ consists of qI and qE. qI can appear as photoinhibition, which may actually be a photoprotective mechanism[7]. qE is the process of enhanced dissipation of Chl excited state energy as heat. qE is activated very rapidly upon illumination (seconds to minutes), and can eliminate up to 75 % absorbed photons[37]. It is energy dependent and rapidly reversible. Full qE requires a pH gradient across the photosynthetic membrane[38] and the presence of the Lhc-like PsbS protein[39], that acts as a pH sensor[40]. The light-induced acidification of the thylakoid lumen activates the xanthophyll cycle, converting violaxanthin into zeaxanthin. The resulting increase of zeaxanthin concentration in the thylakoid membrane is correlated with the extent of qE in many plants[7].

Two different (but not mutually exclusive) molecular mechanisms of qE have been proposed recently[41,42]. In both mechanisms a light-harvesting complex can switch between two states, one where the absorbed energy has a long lifetime, and another where the absorbed energy is rapidly lost as heat. The loss as heat would occur either through energy transfer from Chl to a Lut[42], or through charge separation in a Chl-Zea dimer and subsequent rapid relaxation to the ground state[41]. There is further debate on whether the loss occurs in LHCII or CP24/26/29 or in both. Over the years *in vitro* aggregation of LHCII has served as a model for NPQ, because it leads to NPQ-like fluorescence

quenching[43]. Chapter 4 treats LHCII aggregation, and in Chapter 5 hydrostatic pressure is used to induce switching of LHCII between states with different extents of fluorescence quenching.

1.5 Experimental techniques

The results in this thesis were obtained from optical spectroscopy. This section describes the various techniques used for the experiments. Novel is the measurement of time-resolved fluorescence of crystals of pigment-protein complexes. Section 1.6 describes the methods used for data-analysis.

1.5.1 Absorption and fluorescence

Each photosynthetic (super)complex has a unique pigment and protein composition, with unique interactions among them. This leads to spectral features that can be measured by steady-state spectroscopy, like absorption and emission of light (fluorescence). Interpretation of steady-state spectra is aided by the Jablonski-diagram[44] of a pigment, see Figure 8. This diagram shows different energetic states that a pigment can adopt.

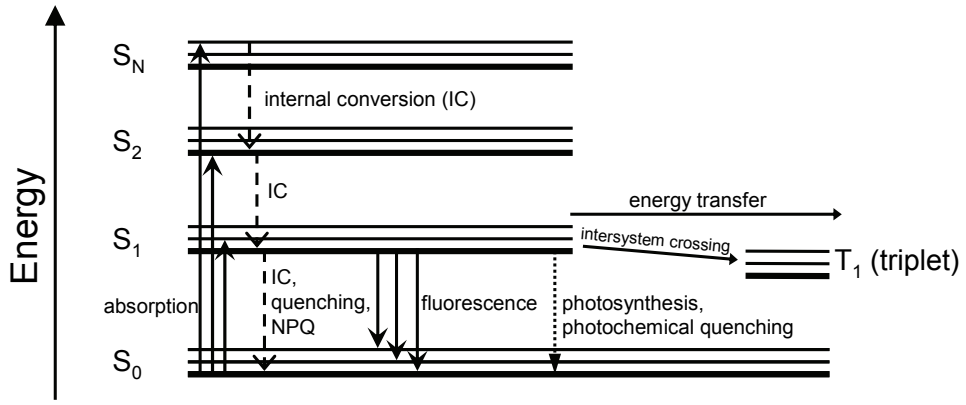

Figure 8. *Jablonski diagram of a pigment molecule. Absorption of a photon corresponds to the transition from the ground state (S_0) to an electronically excited state (S_N). The excited state can loose its energy via internal conversion (IC), via intersystem crossing (forming a triplet state), via photochemical quenching (e.g. charge separation), via fluorescence, via transfer to another pigment. When the pigment is part of a photosystem, energy can also be used for photosynthesis.*

Absorption of a photon leads to transition from the ground state (S_0) to an excited state S_i. An excited pigment rapidly relaxes to the lowest excited state (S_1) via internal conversion (IC), converting electronic energy into heat. From S_1 the pigment can relax to S_0 by IC, by intersystem crossing (forming a triplet state), by photochemical quenching (e.g. release of

an electron to the medium), by energy transfer to another pigment, or by the emission of a photon (fluorescence). In photosynthetic complexes the S_1 energy can also be used for photosynthesis. ISC, IC, photochemical quenching and photon emission compete with photosynthesis for energy. Thereby, the emission of photons (fluorescence) provides a simple and informative way to study photosynthesis.

The fluorescence and absorption spectra result from spectra of the many pigments that bind to photosynthetic systems. The absorption spectrum is simply the sum of the spectra of all individual pigments, given the pigment-pigment and pigment-protein interactions. The fluorescence spectrum is a bit more complex. Once a pigment is excited, the energy will distribute over all pigments, by rapidly "hopping" from one pigment to another. Energy transfer is more likely to occur from pigments with high S_1 energy to low S_1 energy than vice versa (see Section 1.2.3). This results in a higher probability that the excited state energy is on low- than high-energy pigments, or, in other words, the low-energy pigments become more populated. Therefore the fluorescence emission is dominated by the spectra of low-energy pigments (i.e. with "red" fluorescence), and has a smaller contribution from high-energy pigments. In samples containing an RC (e.g. PSII core particles), much of the energy is used for photosynthesis, and therefore the fluorescence is relatively weak. In isolated light-harvesting complexes (e.g. LHCII), no photosynthesis occurs, and therefore the fluorescence is relatively strong.

Absorption and fluorescence spectra are often so complex that interpretation is very challenging. An alternative approach, used in this thesis, can yield more specific information: the measurement of time-resolved fluorescence.

1.5.2 Time-resolved fluorescence emission

Information on the rates of the processes in Figure 8 can be obtained via time-resolved fluorescence: recording the fluorescence as a function of time after absorption of a photon. This enables, for example, measuring the rate of energy transfer from one light-harvesting complex to another. Several methods are available to measure time-resolved fluorescence. The experiments in this thesis were performed with time-correlated single photon counting and a synchroscan streak-camera system. Both methods are based on exciting a sample with a very short light pulse, and then measuring the time of emission, and the energy of the emitted photons.

1.5.2.1 Time-correlated single photon counting

The concept of time-correlated single photon counting (TCSPC, also known as single photon timing) is summarized in Figure 9. An exciting light pulse is absorbed by the sample, inducing fluorescence. Part of the light pulse is diverted before reaching the sample, and starts a clock. This clock stops when a fluorescence photon is detected, and the delay time between light pulse and photon detection is stored. This series of events is

repeated many times, and the frequency histogram of arrival times gives the evolution of the fluorescence in time upon excitation (Figure 9, right). Between sample and detector a filter or a monochromator is placed, which transmits only photons of certain energy (wavelength, color). By repeating an experiment with various filters or monochromator settings, the evolution of the fluorescence emission spectrum in time after excitation can be reconstructed.

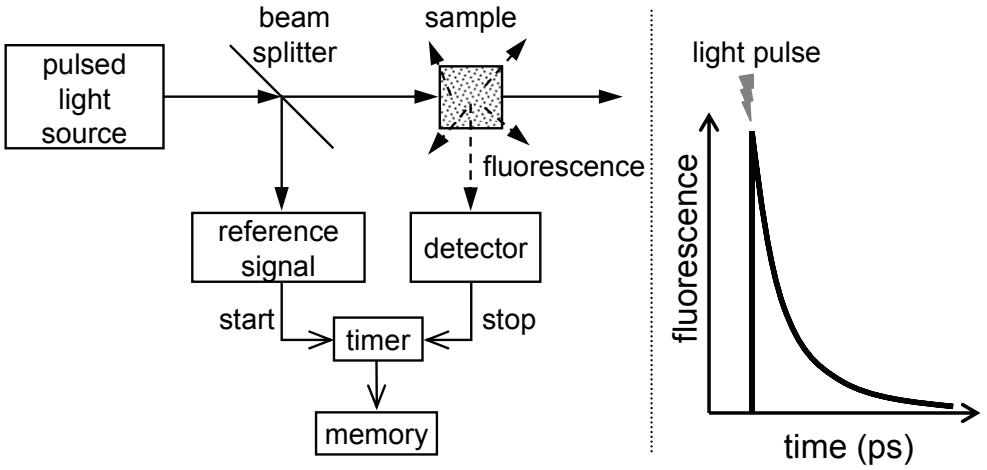

Figure 9. *Simplified scheme of the TCSPC setup (left), and schematic result. Directly after excitation there is strong fluorescence, which decays in time.*

In the setup in Wageningen, laser pulses are generated by a mode-locked titanium:sapphire laser, pumped by a continuous wave diode-pumped, frequency-doubled Nd:YVO_4 laser. The repetition rate was decreased to 3.8 MHz with a pulse-picker, and the frequency doubled. The maximum pulse energy was in general sub-pJ, pulse duration was about 0.3 ps, and polarization was vertical. If necessary the samples were stirred, or a flow cell was used to refresh the sample during the experiments. The sample was in a 10 mm light path silica cuvette, and was temperature controlled by Peltier elements. Fluorescence was detected at 90° angle with respect to the exciting beam, under magic angle polarization.

Part of the laser light excites a fast photodiode, whose output pulses were fed into a constant fraction discriminator (CFD) and used as a stop signal for a time-to-amplitude converter (TAC). A cooled microchannel plate photomultiplier (MCP) detects single photons. The MCP output is analyzed in another channel of the CFD, and then used as a start signal for the TAC. The output pulses of the TAC were analyzed by an analogue-to-digital converter (ADC). The output of the ADC was gathered in 4096 channels of a multichannel analyzer. The channel time spacing was 1.25 ps, 2 ps or 5 ps. The energy of the excitation pulses was reduced with neutral density filters, to less than 30000 per second, to prevent pile-up distortion, and care was taken to minimize data

distortion by other sources[45]. The instrument response function (IRF) of the setup was obtained from the fast single exponential decay of pinacyanol iodide in methanol (see Chapter 6). Data were analyzed with home-built software[46], as described in section 1.6. The setup is described in more detail by Borst et al.[47].

1.5.2.2 Fluorescence Lifetime Imaging Microscopy

Some samples are spatially inhomogeneous, with different fluorescence kinetics in different parts of the sample. A good example is chlorophyll fluorescence from plants with C_4 metabolism. Cells in different parts of leaves of such plants, have different types of chloroplasts, with different amounts of PSI and PSII, that consequently have different fluorescence kinetics. In such cases, bulk experiments give limited information, and it is valuable to combine TCSPC with microscopy. This combination leads to a setup called FLIM, short for fluorescence lifetime imaging microscopy. In FLIM a pulsed light beam is focussed into a very small volume element ('voxel'), typically sized 0.5x0.5x1.5 µm. The resulting fluorescence is detected by TCSPC, as described above. The beam is scanned over the sample, thus conducting a TCSPC experiment in each individual voxel. This results in a three-dimensional dataset, with a fluorescence decay curve in each voxel of a microscopy image.

The FLIM setup used in this thesis will be described below, using our experiments with crystals of LHCII, published in Nature in 2005[48]. The crystals were excited with 860 nm light pulses generated by a titanium:sapphire laser similar to that used for TCSPC experiments. The pulse energy was in general 10 pJ or less, with 150 fs pulse duration, at a rate of $76 * 10^6$ pulses per second. The output of the laser was shaped and its power modulated by a beam conditioning unit, and directly coupled into the microscope. The excitation light was focused into the sample using a 60x objective. Fluorescence was collected with the same objective, and separated from the excitation light by a dichroic mirror. Single photons were then detected, with a nondescanned detector similar to that used in TCSPC experiments. In front of its MCP were filters transmitting either 670 to 730 nm or 710 to 750 nm light. Images were recorded with a frame size of 32x32, 64x64 or 256x256 pixels, with 4096, 1024 or 64 time channels, respectively. The total time-window was always 13.2 ns. The setup is described in more detail in Chapter 6 and by Russinova et al.[49].

LHCII has been studied extensively in the context of photoprotection by nonphotochemical quenching (NPQ, see also Section 1.4). It was shown to switch between an "active state" in which it efficiently harvests light for PSII, and a state in which it dissipates most energy as heat[7,50-55] (see also Chapters 4 and 5 of this thesis). LHCII research was aided by the publication of a crystal structure at 0.272 nm[13] (and later 0.25 nm[15]) resolution, a considerable improvement on the old structure at 0.34 nm resolution[56]. Extensive modelling based on the new structure, could explain many spectral

features of LHCII[57]. In structure-based modelling, it is usually tacitly assumed that the structure is the same when the protein is dissolved in buffer, and when it is in a crystal lattice. In the case of LHCII this is particular interesting, because of its ability to switch between states with different fluorescence properties. To test to which of these states LHCII in its crystal lattice corresponds most strongly, the time-resolved fluorescence of LHCII crystals was measured by FLIM, and then the crystals were mildly dissolved and remeasured on the same setup. Next the dissolved LHCII was aggregated by removal of detergent, a procedure known to induce NPQ-like fluorescence quenching[43], and again measured on the same setup. The results of these experiments are summarized in Figure 10.

Figure 10A shows a fluorescence image of a crystal of LHCII, after excitation at 860 nm. LHCII hardly absorbs light of this wavelength; however, under special conditions two-photon absorption (TPA) is possible. In TPA, the energy of two simultaneously absorbed photons brings a pigment to an excited state, from where it relaxes following the

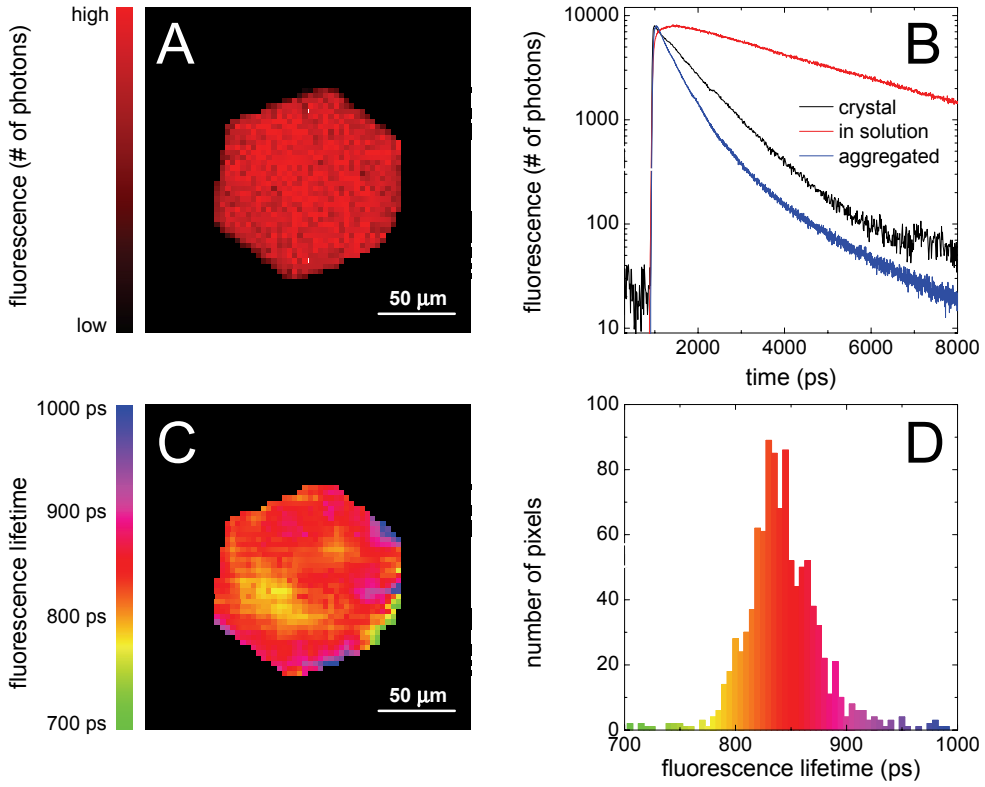

Figure 10. *Fluorescence lifetime imaging of LHCII crystals. A: steady state fluorescence emission microscopy image, B: fluorescence decay trace of one pixel of the image in A, in addition traces are shown of LHCII in solution and of aggregated LHCII, C: result of analysis of the FLIM image, color codes for the fluorescence lifetime obtained from a mono-exponential fit of the decay trace in each pixel, D: frequency histogram of the fluorescence lifetimes in C.*

Jablonski diagram (Figure 8), possibly by fluorescence. Simultaneous absorption requires the two photons to interact with the pigment within one femtosecond (10^{-15} s). This is very unlikely to occur under most light conditions, and requires special efforts. The probability of TPA increases when the photon density in time and space becomes high. The photon density is maximized by using pulsed light: in this way photons are closely together in time. The pulsed light is focussed on the sample, thus bringing photons close together in space. Although generating TPA requires considerable effort, it is worthwhile: pigments will only be excited in the spot with the highest photon density. In other words, only in the voxel (typically sized 1.5x0.5x0.5 μm) into which the objective focuses the laser beam, pigments are excited. This point is in fact a small volume, called voxel,. When the laser beam is moved, pigments in a different voxel are excited. By scanning the laser beam through a sample, and recording fluorescence from each voxel, a three-dimensional fluorescence image can be obtained. In the experiments in this thesis the laser was scanned in two directions, yielding a two-dimensional image.

In FLIM, in each pixel/voxel of an image a fluorescence decay trace is recorded. The black curve in Figure 10B is the trace from one of the pixels in Figure 10A. The other traces are those of LHCII in solution, and aggregates of LHCII, measured on the same setup. Such traces can be fitted with an exponential decay: $F(t) = a * e^{-t/\tau}$, with fitting parameters amplitude (a) and fluorescence lifetime (τ). In FLIM analysis the traces of all pixels are fitted. The result is presented in Figure 10C, where the color codes for the fluorescence lifetime. Figure 10D, shows the frequency histogram of the fluorescence lifetimes. From Figure 10C and D it follows that the fluorescence lifetime is approximately 0.85+/-0.05 ns, and is roughly the same throughout the crystal. The fluorescence lifetime of LHCII in solution was 4 ns, that of aggregates of LHCII was 0.65 ns (fits of traces in Figure 10B). Thus it is clear that the crystal structure does not correspond to the “active state” in which it efficiently harvests light for PSII, but rather to a state in which it dissipates most energy as heat[48].

Interestingly, also the Raman and low temperature fluorescence emission spectra of the crystals were different from those of LHCII in solution. These spectra are sensitive to the structure and organization of the pigments in the protein. So fluorescence quenching and structural differences between crystallized LHCII and LHCII in solution could be related, and further interpreted with the structure[48]. There appeared two candidates for the site of quenching: a Chl *a* dimer in close proximity of a lutein, and a Chl *b* close to neoxanthin. It was later confirmed that in aggregated LHCII excited-state energy is transferred from Chl to Lut, supporting the role of Lut in fluorescence quenching in the crystals[42].

1.5.2.3 Streak-camera

Another method of time-resolved fluorescence spectroscopy that relies on pulsed excitation of the sample, uses detection with a synchroscan streak-camera system. This detector records simultaneously a photon's wavelength, and its delay time relative to the exciting pulse. It has several advantages and disadvantages with respect to TCSPC. The main advantage is the ability to measure the temporal evolution of the entire fluorescence spectrum, rather than recording the fluorescence decay at a single wavelength interval. Moreover, the time resolution is better than that of TCSPC, as indicated by the width of the IRF: ~30-50 ps for TCSPC (and FLIM), and ~3 ps for the streak-camera. The main disadvantage is the lower sensitivity of the streak-camera. The theory and experimental aspects of the streak-camera are discussed elaborately in Chapter 2, and the specifications of the setup in Wageningen are discussed in Chapter 3.

1.6 Data analysis

Data analysis may be as important as data acquisition. The previous sections described various methods of data acquisition (mainly time-resolved fluorescence). This section describes the analysis of the acquired data. Time-resolved fluorescence data can be analyzed in several ways. In general, the fluorescence decay traces are fitted with an exponential function *f(t)*, resulting in amplitudes a_i and fluorescence lifetimes τ_i, which equal by definition the inverse of the decay rates k_i.

$$f(t) = \sum_{i=1,2,..}^{N} a_i \cdot e^{-t/\tau_i} = \sum_{i=1,2,..}^{N} a_i \cdot e^{-k_i t} \qquad (2)$$

These fitting parameters can then be interpreted in terms of which pigments are present in the sample, and which physical processes take place (Figure 8). In many cases a lot of fluorescence decay traces are recorded, for example at difference excitation and emission wavelengths, or in different pixels/voxels (FLIM). In such cases, fitting yields amplitudes and lifetimes for each combination of excitation-wavelength/emission-wavelength/pixel-coordinate. Often, however, (some) fluorescence lifetimes are known to be the same for some or all traces. In that case the data can be analyzed globally. In global analysis all data are fitted simultaneously, thereby forcing some fitting parameters to be equal for multiple traces. Global analysis has several advantages over trace-by-trace analysis. In general it will yield a more accurate estimation of the fitting parameters, and it enables resolving more kinetic components (more rates k_i)[58]. Global analysis is discussed extensively in Chapter 3, and in several reviews[59,60].

One special case of global analysis will be described here, yielding decay associated spectra (DAS). Determination of DAS requires fluorescence decay traces at

several emission wavelengths (λ_{em}), measured for example by TCSPC or with a streak-camera. The fluorescence lifetimes τ_i ($\equiv 1/k_i$) are assumed to be identical at each λ_{em}. The total dataset is then fitted with function $g(t,\lambda_{em})$, analogous to $f(t)$ in equation (2).

$$g(t,\lambda_{em}) = \sum_i \sum_{\lambda_{em}} a_i(\lambda_{em}) \cdot e^{-t/\tau_i} = \sum_i \sum_{\lambda_{em}} a_i(\lambda_{em}) \cdot e^{-k_i t} \quad (3)$$

Note that, in accordance with the assumption mentioned above, a but not τ and k depend on λ_{em}. This is correct, for example, for a mixture of two non-interacting pigments, that decay with fluorescence lifetimes τ_1 and τ_2, and have emission spectra $F_1(\lambda_{em})$ and $F_2(\lambda_{em})$. At t=0, when the light pulse has just hit the sample, the observed spectrum is $f^{t=0}(\lambda_{em}) = f_1{}^{t=0}(\lambda_{em}) + f_2{}^{t=0}(\lambda_{em})$, where f_1 has the same shape as F_1 and f_2 the same as F_2. The intensity of the each spectrum decreases exponentially, so at t=T, the observed spectrum is $f^{t=T}(\lambda_{em}) = f_1{}^{t=T}(\lambda_{em}) * e^{-T/\tau_1} + f_2{}^{t=T}(\lambda_{em}) * e^{-T/\tau_2}$. Comparing this with equation (3), it is clear that $a_1(\lambda_{em}) = c_1 * F_1{}^{t=0}(\lambda)$ and $a_2(\lambda_{em}) = c_2 * F_2{}^{t=0}(\lambda)$, with c_1 and c_2 constants that are independent of time and wavelength. $a_1(\lambda_{em})$ and $a_2(\lambda_{em})$ are associated with decays of lifetimes τ_1 and τ_2, and they are therefore called decay associated spectra (DAS). In this specific case, each DAS originates from one "species" (pigment), and therefore the DAS are species associated spectra (SAS). In more complicated systems, with for example energy transfer taking place, the DAS no longer originate from individual species, and more complicated fitting models are required to obtain the SAS. This can be done in a procedure called target analysis, which is described in Chapter 2.

1.7 This thesis

The work in this thesis concerns early steps of the photosynthetic process: the steps from absorption of a photon, to the first stable charge separation. Chapter 2 describes in detail the streak-camera setup, and methods to analyze the resulting data. The same analysis methods were used for the TCSPC and FLIM data in the other chapters.

Chapters 4 and 5 describe experiments aimed at understanding the mechanism(s) of fluorescence quenching of LHCII, which is reminiscent of nonphotochemical quenching *in vivo*. These chapters show two ways in which quenching can be induced. In Chapter 3, the structure of the unusually long N-terminal tail of the minor light-harvesting complex CP29 was studied. This tail is phosphorylated during stress[61], and CP29 may be a site of quenching during NPQ[26].

The comparison between LHCII in crystal form and in solution (see Section 1.5.2.2) was also used for PSI (Chapter 6). A novel method of analysis in Chapter 6 enables direct determination of the trapping rate from PSI core inside the PSI-LHCI supercomplex, and the wavelength-dependent energy transfer rate from LHCI to PSI core and *vice versa*.

1.8 References

1. Nelson, N. and Ben-Shem, A. (2004), *Nat. Rev. Mol. Cell Biol.* **5**, 971-982.
2. Moore, R., Clark, W. D. and Vodopich, D. S. 1998. Botany. WCB/McGraw-Hill, Burr Ridge, IL, United States of America. 919 p.
3. Schopf, J. W. 1992. The oldest fossils and what they mean. In Major Events in the History of Life, editor Schopf, J. W., Jones and Bartlett, USA, Boston. p. 29-63.
4. Krawczyk, S. (1989), *Biochim. Biophys. Acta* **976**, 140-149.
5. van Amerongen, H., Valkunas, L. and van Grondelle, R. 2000. Photosynthetic excitons. World Scientific Publishing, Singapore. 590 p.
6. Plumley, F. G. and Schmidt, G. W. (1987), *Proc. Natl. Acad. Sci. U. S. A.* **84**, 146-150.
7. Niyogi, K. K. (1999), *Annu. Rev. Plant Physiol. Plant Mol. Biol.* **50**, 333-359.
8. Förster, T. (1949), *Zeitschrift für Naturforschung* **4a**, 321-327.
9. Drenth, J. 2007. Principles of Protein X-Ray Crystallography. Springer, New York, NY. 332 p.
10. Amunts, A., Drory, O. and Nelson, N. (2007), *Nature* **447**, 58-63.
11. Ferreira, K. N., Iverson, T. M., Maghlaoui, K., Barber, J. and Iwata, S. (2004), *Science* **303**, 1831-1838.
12. Jordan, P., Fromme, P., Witt, H. T., Klukas, O., Saenger, W. and Krauss, N. (2001), *Nature* **411**, 909-917.
13. Liu, Z. F., Yan, H., Wang, K., Kuang, T., Zhang, J., Gui, L. and Chang, W. (2004), *Nature* **428**, 287-292.
14. Loll, B., Kern, J., Saenger, W., Zouni, A. and Biesiadka, J. (2005), *Nature* **438**, 1040-1044.
15. Standfuss, J., Terwisscha van Scheltinga, A. C., Lamborghini, M. and Kühlbrandt, W. (2005), *EMBO Journal* **24**, 919-928.
16. Kamiya, N. and Shen, J.-R. (2003), *Proc. Natl. Acad. Sci. U. S. A.* **100**, 98-103.
17. Yan, H. C., Zhang, P. F., Wang, C., Liu, Z. F. and Chang, W. R. (2007), *Biochem. Biophys. Res. Commun.* **355**, 457-463.
18. Barber, J. (2002), *Curr. Opin. Struct. Biol.* **12**, 523–530.
19. Dekker, J. P. and van Grondelle, R. (2000), *Photosynth. Res.* **63**, 195-208.
20. Vasil'ev, S., Orth, P., Zouni, A., Owens, T. G. and Bruce, D. (2001), *Proc. Natl. Acad. Sci. U. S. A.* **98**, 8602-8607.
21. Dekker, J. P. and Boekema, E. J. (2005), *Biochim. Biophys. Acta* **1706**, 12-39.
22. Croce, R., Weiss, S. and Bassi, R. (1999), *J. Biol. Chem.* **274**, 29613-29623.
23. Horton, P., Wentworth, M. and Ruban, A. V. (2005), *FEBS Letters* **579**, 4201-4206.
24. van Amerongen, H. and Dekker, J. P. 2003. Light-Harvesting in Photosystem II. In Light-Harvesting Antennas in Photosynthesis, editors: Green, B. R. and Parson, W. W., Kluwer Academic Publishers, Dordrecht. p. 219-251.
25. Sandona, D., Croce, R., Pagano, A., Crimi, M. and Bassi, R. (1998), *Biochim. Biophys. Acta* **1365**, 207-214.
26. Ahn, T. K., Avenson, T. J., Ballottari, M., Cheng, Y.-C., Niyogi, K. K., Bassi, R. and Fleming, G. R. (2008), *Science* **320**, 794-797.
27. Bassi, R., Croce, R., Cugini, D. and Sandona, D. (1999), *Proc. Natl. Acad. Sci. U. S. A.* **96**, 10056-10061.
28. Boekema, E. J., van Roon, H., van Breemen, J. F. L. and Dekker, J. P. (1999), *Eur. J. Biochem.* **266**, 444-452.
29. Fromme, P., Schlodder, E. and Jansson, S. 2003. Structure and Function of the Antenna System in Photosystem I. In Light-Harvesting Antennas in Photosynthesis, editors: Green, B. R. and Parson, W. W., Kluwer Academic Publishers, Dordrecht. p. 253-279.
30. Jensen, P. E., Bassi, R., Boekema, E. J., Dekker, J. P., Jansson, S., Leister, D., Robinson, C. and Scheller, H. V. (2007), *Biochim. Biophys. Acta* **1767**, 335-352.

31. Croce, R., Morosinotto, T., Castelletti, S., Breton, J. and Bassi, R. (2002), *Biochim. Biophys. Acta* **1556**, 29-40.
32. Jansson, S. (1994), *Biochim. Biophys. Acta* **1184**, 1-19.
33. Mullet, J. E., Burke, J. J. and Arntzen, C. J. (1980), *Plant Physiol.* **65**, 814-822.
34. Rivadossi, A., Zucchelli, G., Garlaschi, F. M. and Jennings, R. C. (1999), *Photosynth. Res.* **60**, 209-215.
35. Castelletti, S., Morosinotto, T., Robert, B., Caffarri, S., Bassi, R. and Croce, R. (2003), *Biochemistry* **42**, 4226-4234.
36. Barber, J. and Andersson, B. (1992), *Trends Biochem. Sci.* **17**, 61-66.
37. Demmig-Adams, B., Adams III, W. W., Barker, D. H., Logan, B. A., Bowling, D. R. and Verhoeven, A. S. (1996), *Physiol. Plant.* **98**, 253-264.
38. Horton, P., Ruban, A. V. and Walters, R. G. (1996), *Annu. Rev. Plant Physiol. Plant Mol. Biol.* **47**, 655-684.
39. Li, X. P., Bjorkman, O., Shih, C., Grossman, A. R., Rosenquist, M., Jansson, S. and Niyogi, K. K. (2000), *Nature* **403**, 391-395.
40. Li, X.-P., Gilmore, A. M., Caffarri, S., Bassi, R., Golan, T., Kramer, D. and Niyogi, K. K. (2004), *J. Biol. Chem.* **279**, 22866-22874.
41. Holt, N. E., Zigmantas, D., Valkunas, L., Li, X.-P., Niyogi, K. K. and Fleming, G. R. (2005), *Science* **307**, 433-436.
42. Ruban, A. V., Berera, R., Ilioaia, C., van Stokkum, I. H. M., Kennis, J. T. M., Pascal, A. A., van Amerongen, H., Robert, B., Horton, P. and van Grondelle, R. (2007), *Nature* **450**, 575-578.
43. Ruban, A. V. and Horton, P. (1999), *Plant Physiol.* **119**, 531-542.
44. Jabłoński, A. (1935), *Zeitschrift für Physik* **94**, 38-46.
45. van Hoek, A. and Visser, A. J. W. G. (1985), *Anal. Instrum.* **14**, 359-378.
46. Digris, A. V., Skakoun, V. V., Novikov, E. G., van Hoek, A., Claiborne, A. and Visser, A. J. W. G. (1999), *Eur. Biophys. J.* **28**, 526-531.
47. Borst, J. W., Hink, M. A., van Hoek, A. and Visser, A. J. W. G. (2005), *J. Fluoresc.* **15**, 153-160.
48. Pascal, A. A., Liu, Z. F., Broess, K., van Oort, B., van Amerongen, H., Wang, C., Horton, P., Robert, B., Chang, W. R. and Ruban, A. (2005), *Nature* **436**, 134-137.
49. Russinova, E., Borst, J.-W., Kwaaitaal, M., Cano-Delgado, A., Yin, Y., Chory, J. and de Vries, S. C. (2004), *Plant Cell* **16**, 3216-3229.
50. van Oort, B., van Hoek, A., Ruban, A. V. and van Amerongen, H. (2007), *J. Phys. Chem. B* **111**, 7631-7637.
51. van Oort, B., van Hoek, A., Ruban, A. V. and van Amerongen, H. (2007), *FEBS Letters* **581**, 3528-3532.
52. Horton, P., Ruban, A. V., Rees, D., Pascal, A. A., Noctor, G. and Young, A. J. (1991), *FEBS Letters* **292**, 1.
53. Ruban, A. V. and Horton, P. (1992), *Biochim. Biophys. Acta* **1102**, 30.
54. Mullineaux, C. W., Pascal, A. A., Horton, P. and Holzwarth, A. R. (1993), *Biochim. Biophys. Acta* **1141**, 23-28.
55. Ruban, A. V., Young, A. and Horton, P. (1994), *Biochim. Biophys. Acta* **1186**, 123-127.
56. Kühlbrandt, W., Wang, D. N. and Fujiyoshi, Y. (1994), *Nature* **367**, 614-621.
57. Novoderezhkin, V. I., Palacios, M. A., van Amerongen, H. and van Grondelle, R. (2005), *J. Phys. Chem. B* **109**, 10493-10504.
58. Beechem, J. M., Brand, L. and Johnson, M., L. 1992. Global analysis of biochemical and biophysical data. In Methods in Enzymology, Academic Press, San Diego. p. 37-54.
59. Holzwarth, A. 1996. Data Analysis of Time-Resolved Measurements. In Biophysical Techniques in Photosynthesis, editors: Amesz, J. and Hoff, A. J., Kluwer Academic Press, Dordrecht. p. 75-92.
60. van Stokkum, I. H. M., Larsen, D. S. and van Grondelle, R. (2004), *Biochim. Biophys. Acta* **1657**, 82-104.

61. Testi, M. G., Croce, R., Polverino-De Laureto, P. and Bassi, R. (1996), *FEBS Letters* **399**, 245-250.

Chapter 2

(Sub)-Picosecond spectral evolution of fluorescence studied with a synchroscan streak-camera system and target analysis

based on:
I.H.M. van Stokkum, B. van Oort, F. van Mourik, B. Gobets, and H. van Amerongen, 2008. (Sub)-Picosecond Spectral Evolution of Fluorescence Studied with a Synchroscan Streak-Camera System and Target Analysis. In Biophysical Techniques in Photosynthesis, Volume II, editors: Aartsma, T. J. and Matysik, J., Springer, Dordrecht. p. 223-240.

Summary

A synchroscan streak camera in combination with a spectrograph can simultaneously record temporal dynamics and wavelength of fluorescence representable as an image with time and wavelength along the axes. The instrument response width is about 1% of the time range (of typically 200 ps to 2 ns). The spectral window of 250 nm may lie between 250 and 850 nm. Such spectrotemporal measurements using low excitation intensities have become routine. Sophisticated data analysis methods are mandatory to extract meaningful physicochemical parameters from the wealth of information contained in the streak image. In target analysis a kinetic scheme is used in combination with assumptions on the spectra of the species to describe the system. In this chapter the principals of operation of a streak-camera setup are described, along with the fundamental and technical limitations that one encounters. The correction and calibration steps that are needed as well as data processing and analysis are discussed. Several case studies of bioluminescence are presented, with a particularly in-depth analysis of trimeric Photosystem I core particles of the cyanobacterium *Spirulina platensis*.

2.1 Introduction

Time-resolved fluorescence spectroscopy has proven to be extremely useful in photosynthesis research in the past decades[2]. Time-correlated single photon counting (TCSPC) has often been the method of choice, since it is relatively cheap, provides excellent signal-to-noise ratios and is rather standardized. It is particularly useful for determining the overall charge-separation time of a variety of photosynthetic systems, and can even be applied to entire cells and chloroplasts. Like all methods TCSPC, has its limitations: the instrument response time is several tens of picoseconds, which is a serious draw-back, for instance when studying individual pigment-protein complexes where relevant processes occur on sub-ps and ps time scales. Extremely careful measurements and deconvolution of the time traces are needed to resolve a time constant of at best ~5 ps. A second limitation of TCSPC is that, commonly, one selects one detection wavelength at a time, and recording the spectral evolution of the fluorescence requires subsequent measurements at different wavelengths. This restriction determines to a large extent the minimum time for data recording.

The temporal instrument response of a synchroscan streak-camera system has a full width at half maximum (FWHM) of a few picoseconds. With deconvolution it is even possible to measure at sub-ps time resolution, which is approaching the resolution of fluorescence upconversion[4]. Although the streak camera is generally used to record time-resolved fluorescence, it has also been applied to measure time-resolved absorption spectra

in the range from ps to ns[5]. In this chapter, we discuss fluorescence detection with a streak camera in combination with a spectrograph. This allows for simultaneous registration of both the time of emission of a fluorescence photon and the emission wavelength, reducing the measuring time substantially. The fluorescence photons eventually lead to a two-dimensional image on a CCD camera, of which the vertical position indicates the emission time whereas the horizontal position corresponds to the emission wavelength. An example of such an image (from Gobets et al.[6]) is given in Figure 1, in which the grey levels reflect the fluorescence intensity as a function of time and wavelength. Such an image contains a wealth of information and it will be discussed in detail how this information can be extracted. Throughout this chapter we will refer to these data as "the PSI trimer data".

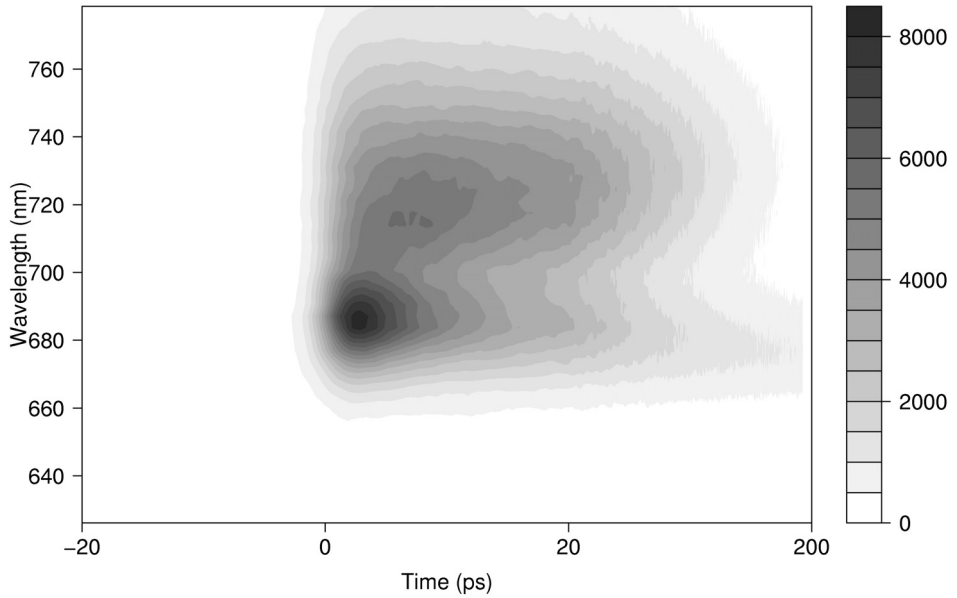

Figure 1. *Filled contour plot of emission data from trimeric core particles of PSI of Spirulina platensis (from Gobets et al.[6]) after excitation at 400 nm. Note that the time axis is linear from –20 to +20 ps relative to the maximum of the IRF, and logarithmic thereafter.*

Two decades ago Campillo and Shapiro wrote an excellent review on the history and possibilities of the streak camera, including its application to photosynthesis.[7] Measurements were performed without wavelength dispersion and only in a few cases several wavelengths were probed. In the same year Freiberg and Saari published a detailed article on the possibilities and limitations of obtaining simultaneously time and wavelength information[8]. Ohtani et al. performed one of the first fluorescence experiments in photobiology in which excellent time resolution (3 ps) was combined with measuring complete spectra, studying bacteriorhodopsin from purple membranes of

Halobacterium halobium[9]. There are several later reports on similar preparations[10-14]. Such single-chromophore systems are generally easier to study than chlorophyll-containing photosynthetic complexes: in photosynthetic systems excitation-energy transfer between chromophores takes place, which in case of too high excitation energies can result in singlet-singlet annihilation, a process that can distort the fluorescence kinetics (see e.g. Sauer and Debreczeny[2]).

Gilmore et al. nicely demonstrated the application of the streak camera to obtain time-resolved fluorescence spectra of leaves[15-17]. Spectral and kinetic differences between Photosystems I and II could be discerned but relevant spectral evolution was only observed for times longer than 100 ps. Donovan et al. used a streak camera with 4–9 ps time resolution to study isolated PSII reaction centers[18]. Measuring at multiple wavelengths they concluded that the charge separation time should be either faster than 1.25 ps or slower than 20 ps. Later studies by van Mourik et al.[19] and Andrizhiyevskaya et al.[20] on isolated PSII reaction centers revealed at least four different lifetimes. For excitation at 681 nm lifetimes of 6 ps, 34 ps, 160 ps and 7 ns were observed. The corresponding decay-associated spectra (DAS) were all different except for the 160 ps and 7 ns DAS, indicating that relatively slow excitation energy transfer (EET) takes place. The 34 ps component was assigned to partly represent EET. Further evidence for slow EET was obtained by the fact that excitation at 690 nm resulted in different DAS. In addition, the data indicated that charge separation is ultrafast (<1 ps) and that relatively slow radical pair relaxation takes place.

The streak camera has been particularly useful for the study of fast kinetics in PSI[6,21-26]. Much spectral evolution occurs on a time scale of several ps and higher, which makes PSI an ideal candidate for streak-camera measurements. Below we will make use of some of these results to demonstrate the experimental possibilities of the setup and the power of advanced data analysis.

The streak camera was also used for the study of light-harvesting complexes. It was for instance used to measure lifetimes on the order of many hundreds of ps to several ns and fluorescence quantum yields[27-30]. Gobets et al. studied LHC-I by fluorescence upconversion at five different wavelengths (IRF 150 fs, timerange 5 ps) and with the streak camera (IRF 3 ps/20 ps , time range 200 ps/2.2 ns) and at common wavelengths the kinetic traces of both techniques joined smoothly in the overlapping time interval[21]. A multitude of decay times was observed ranging from 150 fs to 2 ns (four orders of magnitude) and the corresponding spectra revealed many pathways of EET between carotenoids, Chls *b*, Chls *a* and "red" Chls *a*, the fluorescence of which is shifted to the red by tens of nm as compared to "normal" Chls *a*. Analogously, Kennis et al. demonstrated the applicability of combining fluorescence upconversion and streak data on PSI core complexes[25].

One more streak-camera study on a light-harvesting complex is worth mentioning. Kleima et al. measured the polarized fluorescence of the peridinin-chlorophyll protein

(PCP) and EET between isoenergetic Chl *a* molecules over various distances was reflected by different depolarization times[31]. These results will be discussed in more detail below.

In this chapter we will first describe the principals of operation of a streak-camera setup, followed by a more detailed description of the experimental setup in Wageningen and a discussion of the fundamental and technical limitations that one encounters. In particular, special precautions have to be taken to prevent sample degradation and one has to be aware of the possible occurrence of unwanted nonlinear effects such as singlet-singlet annihilation. In order to exploit the full potential of the setup and the recorded data, several correction and calibration steps are needed as well as advanced data processing and fitting, which will be discussed subsequently.

2.2 Principle of operation of the streak-camera setup

The basic goal of the streak-camera setup (Figure 2) is to determine the wavelength and time of emission of each fluorescence photon detected. A pulsed light source induces fluorescence photons from the sample, which are diffracted by a grating in a horizontal plane after which they hit a horizontal photocathode, producing photo-electrons. These photo-electrons from the photocathode are accelerated and imaged by electrostatic or magnetic lenses onto a 2D detector consisting of a micro-channel plate (MCP) electron multiplier, a phosphor screen, and a cooled CCD camera. On their way from the cathode to the MCP the electrons produced at different times experience a time-dependent vertical electric field (the deflection field or sweep field). Thus photo-electrons generated at different times experience a changed electric field, and therefore hit the MCP at different vertical positions. In the MCP each accelerated photo-electron causes a cascade of electrons (electron multiplication) which in turn hit the phosphor screen, causing a number of photons then detected by the CCD camera. Thus, the vertical and horizontal axes of the 2D CCD-image code respectively for time and wavelength. The time-dependence of the magnitude of the deflection field is sinusoidal and its frequency is locked to the frequency of the same optical oscillator that produces the exciting laser pulses (synchroscan). Thus the streak image on the CCD camera can be accumulated over many successive laser pulses, whilst maintaining a good temporal resolution.

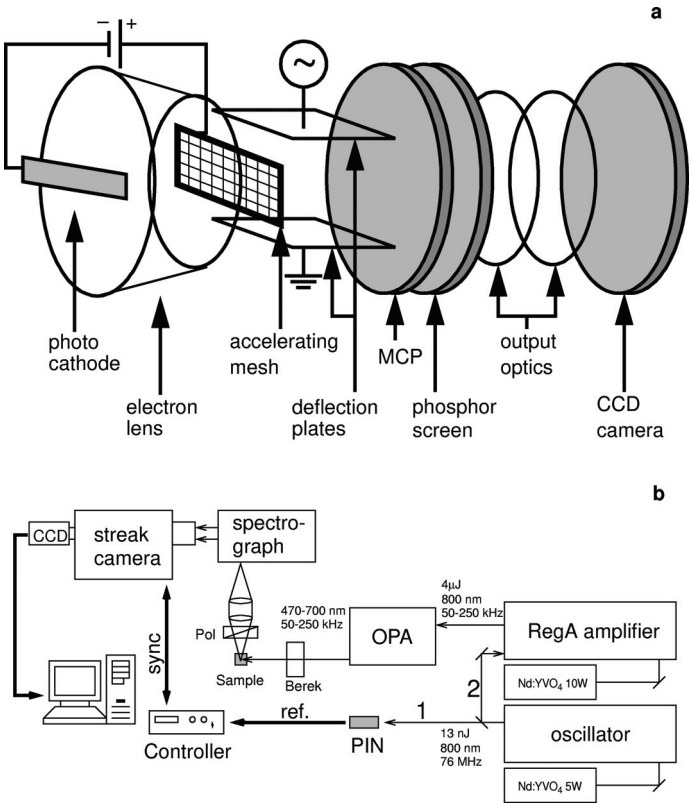

Figure 2. *Schematic representation of a streak camera (a) and of the synchroscan streak-camera setup (b). Further explanation in text.*

2.2.1 Excitation

In the setup in Wageningen, which is comparable to the one in Amsterdam, a mode-locked titanium sapphire laser, pumped by a 5 W cw diode pumped frequency doubled Nd:YVO_4 laser, provides light pulses at a repetition rate of 75.9 MHz, wavelength 800 nm, 1 W average power and 0.2 ps pulse width. The laser beam is split into two paths: Path 1 is used for synchronization of the deflection field. Path 2 enters a regenerative amplifier (RegA), pumped by a 10 W cw diode-pumped frequency-doubled Nd:YVO_4 laser. The amplifier increases the pulse energy to ~4 µJ at a repetition rate of 250 kHz (0.2 ps, 800 nm). These pulses are fed into an Optical Parametric Amplifier (OPA). In the OPA the beam is split: it is partially frequency-doubled and partially used to generate white light. Mixing of these beams leads to selective and tunable amplification of light at any selected wavelength in the range of 470 to 700 nm. This light can be used directly for excitation or after frequency doubling to 235–350 nm. Alternatively, the Ti:sapphire laser can be tuned in the range from 700 to 1000 nm and applying frequency doubling, this allows excitation at "all"

wavelengths longer than 235 nm. The excitation light is directed through a Berek variable waveplate to control its polarization direction and is focussed into the sample by a lens of 15 cm focal length, leading to a focal spot of ~100 μm diameter.

2.2.2 Polarization

Anisotropic measurements can be performed in two ways: by adjusting the polarization of either the detected light, or the exciting light. In the first case one excites with vertically polarized light and turns a polarizer in the detection branch either horizontally or vertically, to obtain the perpendicular and parallel components of the emission. However, in this case one needs to correct for the difference in sensitivity of the detection system for horizontally and vertically polarized light. In particular the gratings of the spectrograph may introduce such a polarization-dependence of the sensitivity of the detection. The second way to record anisotropic measurements is by detecting only the vertical component of the emission, and using the Berek variable waveplate to turn the polarization of the excitation light to either horizontal or vertical, to obtain the perpendicular and parallel components of the emission. The advantage of this method is that one does not have to correct for the polarization-dependence of the detection, however, great care has to be taken not to move the excitation beam by adjusting the variable waveplate, since a change of the position of the focus in the sample will lead to unwelcome intensity changes. For isotropic measurements, one uses vertically polarized excitation light, and a detection polarizer set to the magic angle (54.74º). Finally, if the sample is contained in a rotating cell (see below) that is placed at an angle with the exciting light, one has to be aware that due to the refraction in the sample the direction of both the exciting light and the fluorescence is changed, which will affect both anisotropic and isotropic measurements.

2.2.3 Detection

Light following path 1 hits a reference diode, a tunnel diode, which as a consequence oscillates with a frequency forced to the repetition rate of the laser oscillator. The output of the tunnel diode is used to phase-lock the sweep frequency of the streak camera to the pulses of the laser oscillator. For timing stability on a timescale of minutes, cancellation of drift of the timing is necessary[32]. The deflection field is a sine function of time, with period 1/75.9 MHz = 13.2 ns. The controller can phase-shift the deflection field to move the relevant part of the fluorescence decay into the time window recorded on the CCD camera. The controller can also change the amplitude of the signal to set the time range. In our setup four time-windows can be selected ranging from 180 ps to 2 ns. Instead of phase-locking the deflection field frequency to the frequency of the laser oscillator, like in this setup, the opposite is also feasible: the laser oscillator could be phase locked to the frequency of the

streak camera, in a way similar to the way lasers are being synchronized to synchrotrons or free-electron lasers[33].

Light from the sample is collected at right angle to the excitation beam through an achromatic lens and the detection polarizer, and focussed by a second achromatic lens onto the input slit of a modified Czerny-Turner polychromator. This is equipped with a turret of three gratings with different blazing (spectral window 250 nm) which together span the wavelength range of 250–850 nm. Using concave mirrors after the slit the light is collimated towards the grating and after that the diffracted light is focused onto the photocathode, where the photons induce photo-electrons. These electrons are accelerated by an accelerating mesh and then deflected by the sweeping field. Since the amplitude and sign of the deflection field are functions of time (varying between +V and –V), the extent of deflection depends on the time of arrival of the photon at the photocathode. Only electrons travelling through a field between $+V_c$ and $-V_c$ (V_c = critical deflection field strength) reach the MCP, all other electrons are deflected too much. The electric field is within the detection range every half period of the oscillation frequency, with alternating field sweep direction, so the overall MCP signal is the sum of multiple forward and backward decay trace fragments. This is the so-called backsweep effect. The photons arriving during the backsweep contain information on longer-lived species.

2.2.4 Sample cell

Stable fluorescent chromophores can be measured in a normal cuvette but photosynthetic samples usually require special measuring cells to prevent photo damage and/or a build-up of long-lived triplet or charge-separated states. We mention two types of cells that can be used to measure photosynthetic preparations: a flow-through cell, and a spinning cell. In the case a flow-cell is used, the solute is pumped through a 1x1 mm cuvette with a typical speed of 100 ml/min. Using a repetition rate of 250 kHz, the sample is hit by 15 pulses while passing the excitation spot.

In the case a spinning cell (diameter ~0.1 m, 20–50 Hz rotation) is used, also under the repetition rate of 250 kHz, the sample is hit by 1.5 pulses while passing the excitation spot. This allows for higher intensities and triplet (typical lifetimes µs-ms) build-up is easily avoided. However, the sample returns to the same position with a frequency of 50 Hz, so the build-up of longer-lived (>10 ms) species may still occur. Also the cell is not suitable for larger particles like thylakoid membranes, since the centrifugal forces will spin the particles to the rim of the cell.

2.2.5 Fundamental and technical limitations.

First we will estimate the number of photons detected per laser shot, which is the motivation for synchroscan averaging. Then we will investigate the different sources of time broadening of the instrument response function (IRF), which ultimately result in an IRF width of about 1% of the selected time range.

2.2.5.1 Light limitations.

The detection with a streak camera in combination with a spectrograph (polychromator) puts an important restriction on the size of the illuminated spot of the sample. First of all the horizontal slit of the streak camera typically needs to be closed down to less than 100 μm in order to obtain an instrument response width of a few ps. Alternatively, a narrow width photocathode (70 μm) can be used. This restricts the spot from which fluorescence is collected vertically. The vertical slit of the spectrograph restricts the spot horizontally. In order to maintain good temporal resolution low dispersion gratings, typically 50 grooves/mm, must be used. In order to obtain the desired spectral resolution, also the entrance slit of the spectrograph must be closed down (for a 1/4 m spectrograph, with 50 grooves/mm the dispersion is ~60 nm/mm) (note that some imaging spectrographs enlarge the image of the entrance slit onto the output focal plane by 20%). Therefore, the spot in the sample that is monitored by the detection system typically has a diameter of 100 μm. The spectrograph also dictates the light collection optics. Typically a numerical aperture of *f*/4 is used (*f* is the focal length of the spectrograph).

To get an idea of the best case performance we presume front face detection, of a concentrated sample (in practice detection under an angle of 90 degrees is used, which reduces the detection efficiency significantly). How much light can we get in and out of the small spot monitored in the sample?

For isotropic emission, *f*/4 optics collect <0.5% of the emitted light. Given the restrictions imposed by the spot-sizes and slit-widths, deviating from 1:1 imaging of the fluorescence would not help, because a larger collection angle that can be attained would be spoiled by the magnification of the spot onto the entrance slit. Larger collection angles would require a spectrograph with a larger numerical aperture. This can be reached by using larger mirrors and gratings, but, as will become clear in section 2.2.5.2, the broadening in the spectrometer is proportional to the size of the beam inside the spectrometer. The other way to get a larger collection angle would be to use a shorter focal length spectrograph, but this would further reduce the spectral resolution. The saturation fluence for a laser dye is typically 1 mJ/cm^2, which corresponds to about 75 nJ for a 100 μm spot size. Of course this excitation density cannot be used in a proper fluorescence experiment (except when studying lasing phenomena) and one typically needs to stay at

least one order of magnitude below this value. Things are even worse for most photosynthetic systems where annihilation and other non-linear effects can occur. To avoid these effects, we will make some estimates for 1 nJ excitation pulses. Around 500 nm this corresponds to $2.5*10^9$ photons. If these are all absorbed, the initial fluorescence intensity will be ~$2.5*10^5$ photons/ps (assuming a strongly emitting molecule with a radiative lifetime of 10 ns). Less than 0.5% of these photons are collected using with *f*/4 optics, so we are left with ~10^3 photons/ps entering the slit of the spectrograph. The efficiency of the spectrograph is typically 10-50%, and the quantum yield of the photocathode of the streak camera is 1-20%, so this leaves us with about 1–100 photoelectrons per ps, spread out along the spectral axis.

This demonstrates that substantial averaging is required in order to get good spectro-temporal data, i.e., a large number of shots is required. This is where the main difference between single shot and synchroscan streak cameras comes to light. Single shot devices are optically triggered by the excitation laser and the deflection field is directly generated by a fast photoconductive switch. The maximal switching frequency of such a device is in the kHz range. In a synchroscan camera the deflection field is an oscillatory function synchronized to the repetition rate of the laser oscillator. Therefore, repetition rates up to 76 MHz (and of course sub harmonics of this frequency) can be employed. With a high repetition rate system like the RegA (250 kHz), fluorescence signals from laser dyes can be obtained within seconds, and emission data from less luminant samples in tens of minutes.

2.2.5.2 Time resolution

Together with the electronic contribution of the setup, the major limitation to the time resolution (on the fastest time base) comes from the dispersion in the spectrograph. This phenomenon is related to pulse broadening in pulse stretchers/compressors[34], and stems from the fact that after angular dispersion the wave front of a light pulse exhibits a tilt (with respect to the phase front) given by Hebling[35]:

$$\tan(\theta) = -\lambda \frac{\partial \alpha}{\partial \lambda} \tag{1}$$

where λ is the average wavelength of the light, and α the wavelength-dependent dispersion angle. This can be included in the grating equation

$$\alpha = \arcsin\left(\frac{m\lambda}{d} - \sin(\beta)\right) \tag{2}$$

in which *m* represents the order of diffraction (for all practical purpose here +/– 1), β the incoming angle, and *d* the grating constant. This gives

$$\tan(\theta) = -\lambda \frac{m}{d} \left(\frac{1}{\sqrt{1-(\frac{m\lambda}{d} - \sin(\beta))^2}} \right) \tag{3}$$

In other work the term between brackets is ignored, which corresponds with taking the phase velocity of the light instead of the group velocity[36,37]. For the example given here the difference is insignificant, but this would not be the case for more dispersive gratings.

The total spatial stretch that occurs is $W \tan(\theta)$, where W represents the width of the beam after the grating. This is where the numerical aperture of the detection and spectrograph enter. For an 1/4 m spectrograph, with f/4 optics, W=~5 cm, and for λ=600 nm, m=1, β=0, d=20 μm (50 grooves/mm) this amounts to a spread $\Delta_{dispersion}$ of 1.5 mm, which corresponds to a temporal spread of 5 ps. Therefore, even when using a 50 grooves/mm grating one needs to reduce the f-number of the spectrograph (or the light collection) to get a time response that is close to the limits of the electronic part as described below.

The time resolution limits of the streak camera itself are given by the spread in transit time of the photoelectrons in the streak tube. The transit time spread is mainly generated in the region near the photocathode where the electrons still have a relatively low speed[7,38,39]. The resulting distribution of transit times has a half width of

$$\Delta\tau_c = m\frac{\Delta v}{eE} \tag{4}$$

where m and e are the mass and charge of the electron, Δv is the halfwidth of the initial photoelectron velocity distribution, and E is the field strength in the vicinity of the photocathode. Clearly it is important to have a high acceleration voltage near the photocathode, typically fields of ~10 kV/cm are used. For this extraction field a kinetic energy spread of 1 eV (a blue photon on a red-sensitive photocathode) would lead to a time spread of ~4 ps, which is significant when operating the streak camera on the fastest time base. Near the cut-off wavelength of the photocathode the energy spread becomes much smaller (and fortunately most fluorescence experiments are performed there), but in general there is a noticeable increase of the width of the instrument response when detecting blue photons.

For a higher time resolution higher extraction fields are required, but this comes at the cost of field emission (field induced dark current from the photocathode) and reduced reliability. Significantly higher pulsed extraction voltages can be used for single shot devices but this is not possible at the sweep rate of synchroscan streak cameras. Moreover, once below the 1 ps resolution other factors start to become limiting, like the quality of the imaging of the photocathode onto the MCP. Any aberrations of the electrostatic or

electromagnetic electron lens (like the chromatic aberration $\Delta\tau_c$ caused by differences in electron speeds) will have adverse effects on the width of the instrument response.

The timing errors described here are independent. Therefore the error calculus for the total temporal instrument response width Δ becomes

$$\Delta^2 = (\Delta\tau_c)^2 + (\Delta_{imaging})^2 + (\Delta_{dispersion})^2 + (\Delta_{width})^2 \quad (5)$$

where $\Delta_{imaging}$ is the imaging error due to the electrostatic or magnetic lenses, $\Delta_{dispersion}$ is the dispersion error, and Δ_{width} is the error due to the streak-slitwidth or the cathode width. At time bases larger than 400 ps $\Delta_{imaging}$ and Δ_{width} dominate. Imaging a 70 µm photocathode on a 7 mm wide CCD yields an IRF width of ≈1% of the time base used. At shorter time bases the contribution of the other two terms becomes appreciable, resulting in an IRF width of 3 ps (at 700 nm) for the 200 ps time base (which is 1.5%). At short wavelengths the IRF has broadened to 4 ps because of the larger $\Delta\tau_c$, see Figure 3a. The broadening of the IRF (to 24 ps) with the 2.2 ns time base is clearly visible in Figure 6.

2.2.6 Averaging and correction of images

Typically, the sample is excited with pulses of 0.2 ps FWHM at a repetition rate of 50-250 kHz, which is much lower than the laser oscillator frequency (typically 76 MHz). Synchroscan streak cameras are generally chosen for their ability to do signal integration over extended periods, in which case the time resolution will generally be limited by the drift between the laser and the camera clock. Often individual datasets contain internal tell-tales for absolute timing and of drift e.g. Rayleigh or Raman scattering signals of the excitation pulse can be used to pin down the exact timing of the dataset. A fool-proof method for eliminating all sources of electronic drifts and jitter consists of directly illuminating a spot of the photocathode with the excitation pulse so as to obtain a fiducial, which is an absolute timing reference[32,40]. Using drift compensation electronics, up to 1000 seconds of accumulation on the CCD chip can be performed without significant deterioration of the temporal resolution. Typically, the full time and wavelength ranges are 200 ps and 250 nm, respectively. In the dark the CCD chip accumulates a dark current, which can be minimized by using a Peltier cooling element. Data must be corrected by subtracting the measured dark current contribution. The sensitivity of the entire detection system is quite strongly position dependent. In particular at the edges of the streak-image the signal shows a pronounced drop. To account for this spatial variation of the sensitivity, streak images are divided by a shading image. This shading image consists of a streak image of the light emitted by a halogen lamp, which is directed into the spectrograph. This shading correction directly accounts for the sensitivity variation along the time-axis, since the intensity of the lamp is constant in time. For the sensitivity variation along the wavelength-axis the emission spectrum of the lamp has to be taken into account, which is

done prior to the analysis of the data. Thus, the data is also corrected for the spectral sensitivity of the system.

Because of the limited wavelength resolution of the spectrograph (7 nm FWHM), the curvature-corrected and averaged images can be reduced to a matrix of ≈1000 points in time and 30-60 points in wavelength. In this same averaging step outliers (e.g. resulting from cosmic rays) can be removed. To deal with the small remaining drift after compensation multiple data sets can be collected. Instead of averaging e.g. 30 minutes and suffering from drift induced time broadening, it is better to collect six averages of 5 minutes and correct them for slow drift of time zero. Then, after scrutinous inspection, to check for trends like sample degradation, the series of images can be averaged. Figure 1 depicts a filled contour plot of the PSI trimer data derived from 48 traces between 625 and 785 nm, resulting from an average of 20 images, which will be globally analyzed below. Other visualizations of these data can be found in Gobets et al.[41].

2.2.7 Calibrations

Because of the sinusoidal nature of the deflection field, the "time per pixel"is not a constant, but varies over time. For the shortest (200 ps) time range the time per pixel is practically constant (because the sinusoid is practically linear near the zero-crossing), but for longer time ranges the time per pixel varies significantly. Calibration of the time base can be done by fitting the train of imaged pulses from an etalon, to estimate a polynomial function that describes the time per pixel over the whole time base. Calibration of the wavelength axis can be done with the help of the lines of a calibration lamp, to estimate a linear function. Images of continuous narrow-band sources are also instrumental for checking that the sweep axis is parallel to the vertical axis of the CCD. A crucial procedure for the analysis of the two-dimensional data sets is the characterization of the curvature of the image, i.e. the spatial dependence of "time zero" on the CCD image, caused by the different path lengths of the photo-electrons in the streak camera. Additionally, the light-collecting optics and the spectrograph cause wavelength-dependent temporal shifts. To assess this curvature, scattering of the white light from the OPA is recorded with the streak camera, resulting in an IRF limited curved line on the streak image. In its turn, the intrinsic dispersion of the white light light itself is measured using the optical Kerr signal in carbon disulphide[42]. The combination of both these measurements yields the spatial dependence of time zero during a measurement.

2.2.8 Further exploitation of the horizontal dimension

Streak tubes generally contain a second set of deflection plates, to facilitate the horizontal deflection of photoelectrons. In commercial instruments these plates are e.g. used for blanking (blocking) the detection in between sweeps, or during the back sweep of the

camera. These horizontal plates can also be exploited to perform 2D experiments other than the ones we focused on above, and consequently, spectral information will be lost. In Buhler et al.[43] and Ohtani et al. [12] the horizontal sweep plates were used to provide a secondary, slow, time axis. In combination with a stopped-flow apparatus, the time-evolution of the ps fluorescence lifetime of a sample could thus be measured on a ms time scale. In van Mourik et al. [19] the horizontal sweep direction was synchronized to the electric field applied in a Stark fluorescence experiment, and thus the effect of the Stark field on the fluorescence intensity and lifetime of the sample could be measured.

2.3 Data analysis

When the streak image has been corrected for the instrumental curvature it is ready for data analysis. The aim is to obtain a model-based description of the full data set in terms of a model containing a small number of precisely estimated parameters, of which the rate constants and spectra are the most relevant. With polarized-light experiments also anisotropy parameters come into play. Description of the basic ingredient of kinetic models, the exponential decay, will be given first, followed by a description of how to use these ingredients for global and target analysis (see e.g. the reviews by Holzwarth[44] and van Stokkum et al.[45,46]) of the full data. Our main assumption here is that the time and wavelength properties of the system of interest are separable, which means that spectra of species or states are constant. For details on parameter estimation techniques the reader is also referred to the above cited reviews and references cited therein, and to van Stokkum[47]. Software issues are discussed in van Stokkum and Bal[48]. We will describe in depth the analysis of typical streak data, with the analysis of the PSI trimer data serving as the main example.

2.3.1 Modeling an exponential decay

Here an expression is derived for describing the contribution of an exponentially decaying component to the streak image. The instrument response function (IRF) *i(t)* can usually adequately be modeled with a Gaussian with parameters μ and Δ for, respectively, location and full width at half maximum (FWHM):

$$i(t) = \frac{1}{\tilde{\Delta}\sqrt{2\pi}} \exp(-\log(2)(2(t-\mu)/\Delta)^2) \qquad (6)$$

where $\tilde{\Delta} = \Delta/(2\sqrt{2\log(2)})$. The adequacy of the Gaussian approximation of the IRF shape is depicted in Figure 3. The convolution (indicated by an *) of this IRF with an exponential decay (with rate *k*) yields an analytical expression which facilitates the estimation of the IRF parameters μ and Δ:

$$c(t,k,\mu,\Delta) = \exp(-kt) * i(t)$$
$$= \frac{1}{2}\exp(-kt)\exp(k(\mu + \frac{k\widetilde{\Delta}^2}{2}))\{1 + erf(\frac{t-(\mu + k\widetilde{\Delta}^2))}{\sqrt{2}\widetilde{\Delta}}\} \quad (7)$$

The periodicity of the synchroscan results in detection of the fluorescence that remains after multiples of half the synchroscan period *T* (typically T≈13 ns). Therefore, if lifetimes longer than ~1 ns occur in a sample, the above expression should be extended with a summation over the signal contributions that result from forward and backward sweeps:

$$c(t,k,T) = \sum_{n=0}^{\infty} e^{-kTn}\{e^{-k(t-\mu+T)} + e^{-k(T/2-t-\mu)}\}$$
$$= \{e^{-k(t-\mu+T)} + e^{-k(T/2-t-\mu)}\}/(1-e^{-kT}) \quad (8)$$

Note that it is assumed here that time zero of the time base corresponds to the zero crossing of the sweep, and that the convolution with the IRF is no longer necessary at times longer than T/2. Adding the previous expressions provides the full model function for an exponential decay recorded with a synchroscan streak camera and will henceforth be denoted by $c^I(k)$:

$$c^I(k) \equiv c(t,k,\mu,\Delta,T) = c(t,k,\mu,\Delta) + c(t,k,T) \quad (9)$$

Examples of $c^I(k)$ are depicted in Figure 4c, and fits of traces with linear combinations of decays are shown in Figure 3b, where an ultrafast lifetime of 1.2 ps is detected, and Figure 3c, which is dominated by a 17 ns lifetime (note the huge backsweep signal apparent from the signal "before time zero"). Figure 4a and b depict the fits of two traces from the data shown in Figure 1, using 5 lifetimes. The simultaneous estimation of up to 5 lifetimes in the range of (sub)ps to ns is common routine.

Because fluorescence samples are relatively dilute, elastic scattering or Raman scattering of the excitation light by water (or of other solvents) can complicate the measurement, if they occur within the analyzed wavelength interval. Such contributions can be modeled with an extra component with a time course identical to the IRF *i(t)*. Usually it is possible to restrict the contribution of scattering to a limited wavelength region.

If the streak image has not been corrected for the instrumental curvature the wavelength dependence of the IRF location μ can be modeled with a polynomial (usually a parabola is adequate). Sometimes the IRF shape is better described by a superposition of two Gaussians, leading to a superposition description of the exponential decay[47].

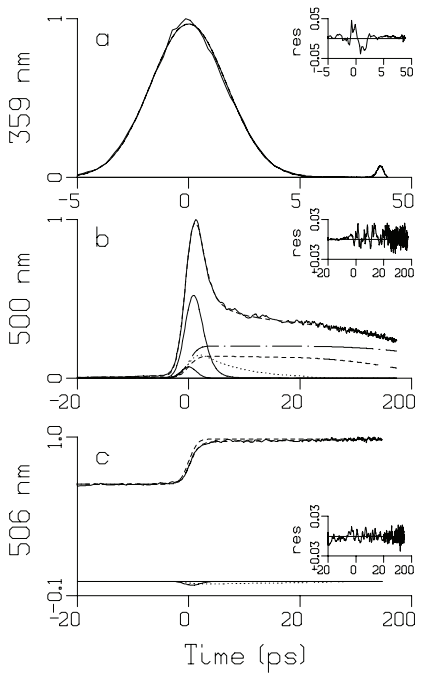

Figure 3. *a: IRF of streak scope measured from scattered white light fitted with a Gaussian. Estimated FWHM Δ = 4 ps, note a small (7%) reflection after 26 ps. Detection wavelength is indicated along the ordinate. Dashed lines indicate fit. Insets show residuals. Time axis is linear from -5 to +5 ps relative to the maximum of the IRF, and logarithmic thereafter. In (b) and (c) it is linear from –20 to +20 ps. b: Emission from thioredoxin reductase mutant C138S (from van den Berg et al.[1]) showing a dominant 1.2 ps decay (solid line). Other contributions to the fit have lifetimes of 7.3 ps (dotted), 0.18 ns (dashed), 0.74 ns (dot dashed), and pulse follower (chain dashed). The sum of these contributions is the fit of the trace, shown as a dashed line. c: Emission from lumazine protein (from Petushkov et al.[3]) showing a dominant 17 ns decay (dashed line). Other contributions to the fit have lifetimes of 0.7 ps (solid) and 24 ps (dotted).*

2.3.2 Global and target analysis

The basis of global analysis is the superposition principle, which states that the measured data $\psi(t,\lambda)$ result from a superposition of the spectral properties $\varepsilon_l(\lambda)$ of the components present in the system of interest weighted by their concentration $c_l(t)$.

$$\psi(t,\lambda) = \sum_{l=1}^{n_{comp}} c_l(t)\varepsilon_l(\lambda) \tag{10}$$

The $c_l(t)$ of all n_{comp} components are described by a compartmental model, that consists of first-order differential equations, with as solution sums of exponential decays. We will consider three types of compartmental models: (1) a model with components decaying monoexponentially in parallel, which yields Decay Associated Spectra (DAS), (2) a sequential model with increasing lifetimes, also called an unbranched unidirectional model, giving Evolution Associated Spectra (EAS), and (3) a full compartmental scheme which may include possible branchings and equilibria, yielding Species Associated Spectra (SAS). The latter is most often referred to as target analysis, where the target is the proposed kinetic scheme, including possible spectral assumptions.

(1) With parallelly decaying components the model reads:

$$\psi(t,\lambda) = \sum_{l=1}^{n_{comp}} c^I(k_l) DAS_l(\lambda) \tag{11}$$

The DAS thus represent the estimated amplitudes of the above defined exponential decays $c^I(k_l)$. The DAS estimated from the PSI trimer data are shown in Figure 4d. Several observations can be made: the 0.4 ps DAS (solid) represents the rise due to the relaxation from the initially excited Soret state (higher excited state, of which the emission is outside the detection range) excitation to the Q_y emission (lowest excited state). The next DAS of 3.9 ps (dotted) is conservative, i.e., the positive and negative area are more or less equal. It represents decay of more blue and rise of more red emission, and can be interpreted as energy transfer from Bulk to Red Chlorophyll *a* (Chl *a*), i.e. Chl *a* that absorb at wavelengths longer than the primary electron donor P700. The 15 ps DAS (dashed) is not conservative, although it does show some rise above 730 nm. Apparently some trapping of excitations takes place on this time scale, concurrently with energy transfer. The 50 ps DAS (dot dashed) represents the trapping spectrum. The long lived (4.9 ns) DAS (chain dashed) is attributed to a small fraction free Chl *a* in the preparation. Clearly, the first three DAS do not represent pure species, and they are interpreted as linear combinations (with positive and negative contributions) of true species spectra.

(2) A sequential model reads:

$$\psi(t,\lambda) = \sum_{l=1}^{n_{comp}} c_l^{II} EAS_l(\lambda) \tag{12}$$

where each concentration is a linear combination of the exponential decays,

$$c_l^{II} = \sum_{j=1}^{l} b_{jl} c^I(k_l) \tag{13}$$

and the amplitudes b_{jl} are given by $b_{11} = 1$ and for $j \le l$:

$$b_{jl} = \prod_{m=1}^{l-1} k_m \Big/ \prod_{n=1, n\neq j}^{l} (k_n - k_j) \tag{14}$$

Examples of c_l^{II} are depicted in Figure 4e, whereas the EAS estimated from the PSI trimer data are shown in Figure 4f. With increasing lifetimes, and thus decreasing rates k_l, the first EAS (equal to the sum of DAS) corresponds to the spectrum at time zero with an ideal infinitely small IRF, $i(t) = \delta(t)$. In Figure 4f, this first EAS is zero in the Q_y region. The second EAS (dotted), which is formed in 0.4 ps and decays in 3.9 ps, represents the sum of the spectra of all excitations that have arrived from the Soret region, and is dominated by Bulk Chl *a*. The third EAS, which is formed in 3.9 ps and decays in 15 ps, is already

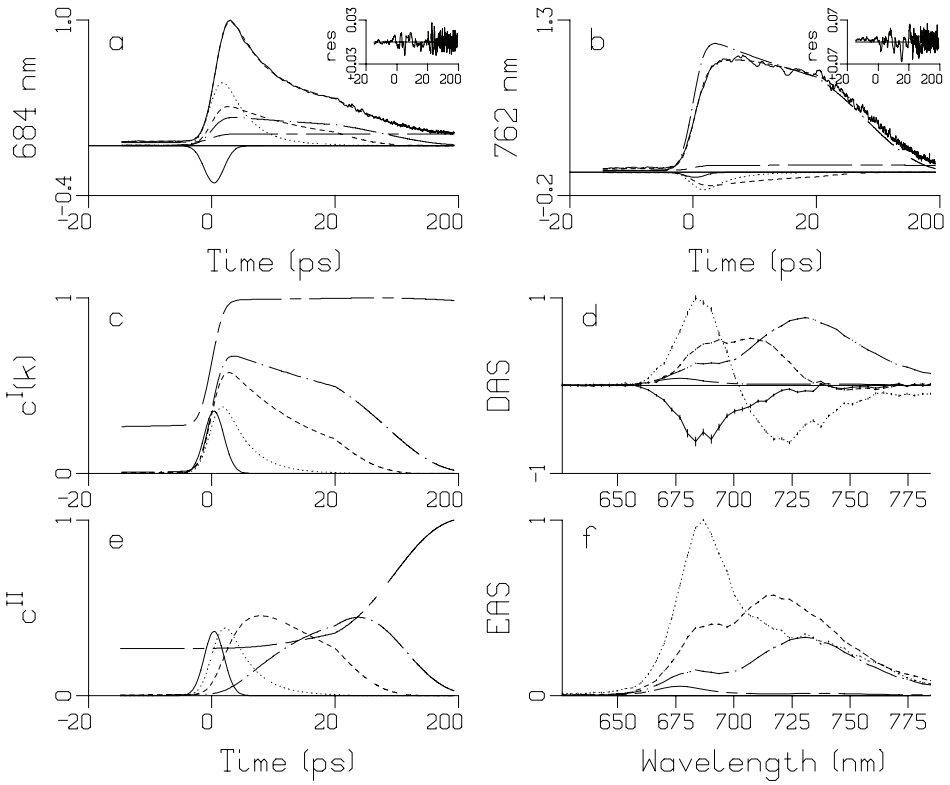

Figure 4. *Results from global analysis of PSI data depicted in Figure 1. Note that in a–c and e the time axis is linear from –20 to +20 ps relative to the maximum of the IRF, and logarithmic thereafter. Insets in a, b show residuals. a: Fit of bulk Chl a emission trace showing multiexponential decay. Contributions of the five exponential decays with different lifetimes (shown in c) are indicated by line type. b: Fit of red Chl a emission trace showing multiexponential rise and decay. c: Exponential decays* $c^I(k_l)$. *Estimated lifetimes: 0.4 ps (solid), 3.9 ps (dotted), 15 ps (dashed), 50 ps (dot dashed), and 4.9 ns (chain dashed). d: Decay Associated Spectra (DAS), note that the first DAS which represents overall rise has been multiplied by 0.2. Vertical bars indicate estimated standard errors. e: Evolutionary concentration profiles* c_l^{II} *(assuming a sequential kinetic scheme with increasing lifetimes). f: Evolution Associated Spectra (EAS). Note that the first EAS is zero, since excitation was in the Soret band.*

dominated by Red Chl *a* emission, which is even more the case with the fourth EAS (dot dashed, formed in 15 ps, decays in 50 ps). The final EAS (chain dashed, formed in 50 ps) is proportional to the final DAS, and represents the spectrum of the longest living component (4.9 ns). Clearly, these EAS do not represent pure species, except for the final EAS, and they are interpreted as a weighted sum (with only positive contributions) of true species spectra.

When neither of these two simple models is applicable, a full kinetic scheme may be appropriate. The problem with such a scheme is that while the kinetics are described by microscopic rate constants, the data only allows for the estimation of decay rates (or lifetimes). Thus additional information is required to estimate the microscopic rates, which can be spectral constraints (zero contribution of SAS at certain wavelengths) or spectral relations. This is detailed in van Stokkum et al.[45].

Now the model reads

$$\psi(t,\lambda) = \sum_{l=1}^{n_{comp}} c_l^{III} SAS_l(\lambda) \tag{15}$$

where the concentrations c_l^{III} are again linear combinations of the exponential decays, with coefficients that depend upon the microscopic rate constants that describe the transitions between all the compartments. Figure 5a depicts the kinetic scheme that was applied to the trimeric PSI data of Figure 1. The concentrations of all compartments are collated in a vector: $c(t) = \left[c_1(t) \quad c_2(t) \quad \ldots \quad c_{n_{comp}}(t) \right]^T = \left[S(t) \quad B(t) \quad R_1(t) \quad R_2(t) \quad F(t) \right]^T$ which obeys the differential equation:

$$\frac{d}{dt} c(t) = Kc(t) + j(t) \tag{16}$$

where the transfer matrix K contains off-diagonal elements k_{pq}, representing the microscopic rate constant from compartment p to compartment q. The diagonal elements contain the total decay rates of each compartment. The input to the compartments is $j(t) = i(t)\left[1 \quad 0 \quad 0 \quad 0 \quad 0\right]^T$. The K matrix from Figure 5a reads:

$$K = \begin{bmatrix} -(k_{SB} + k_{S1} + k_{S2} + k_{SF}) & & & & \\ k_{SB} & -(k_{TB} + k_{B1} + k_{B2}) & k_{1B} & k_{2B} & \\ k_{S1} & k_{B1} & -(k_{T1} + k_{1B}) & & \\ k_{S2} & k_{B2} & & -(k_{T2} + k_{2B}) & \\ k_{SF} & & & & -k_F \end{bmatrix} \tag{17}$$

In Figure 5b the c_l^{III} have been drawn, calculated from the estimated parameters, whereas the estimated SAS are shown in Figure 5c. Note that it has been assumed that the two red Chl *a* compartments only contribute above 690 and 697 nm, respectively. Therefore, the forward and backward rate constants between the Bulk Chl *a* compartment and both compartments of Red Chl *a* can be estimated from the multiexponential decay of the Bulk Chl *a*.

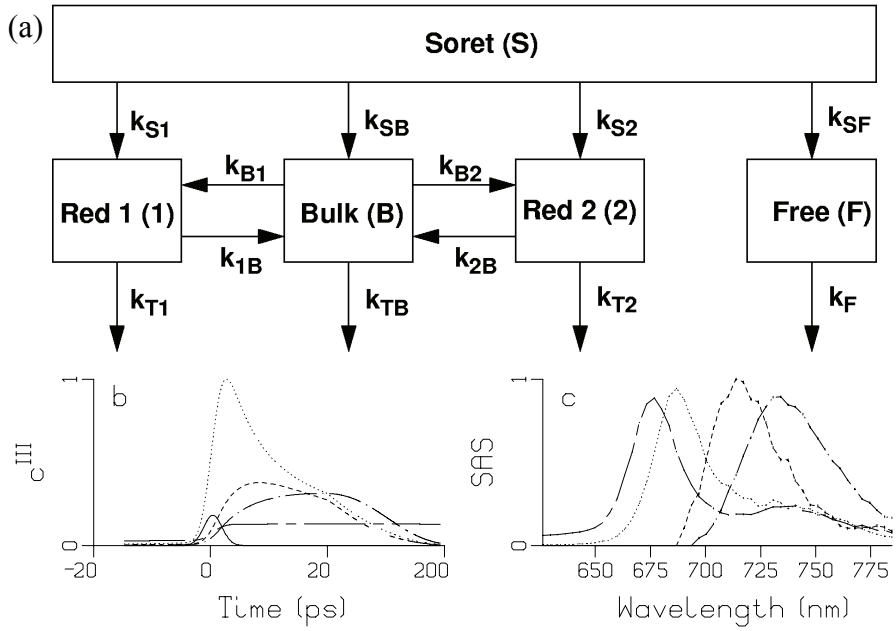

Figure 5. *a: Kinetic scheme used for the target analysis of PSI data depicted in Figure 1. After excitation in the Soret band four compartments are populated: bulk Chl a (B), two pools of red Chl a (1 and 2) and a small fraction of free Chl a (F). The first three compartments equilibrate, and excitations are trapped with different rates. b: concentration profiles* c_l^{III}*, note that the time axis is linear from –20 to +20 ps relative to the maximum of the IRF, and logarithmic thereafter. c: Species Associated Spectra (SAS). Key in b and c: bulk Chl a (dotted), red Chl a 1 (dashed), red Chl a 2 (dot dashed), free Chl a (chain dashed).*

The SAS in Figure 5c are considered satisfactory, because the shapes of the Bulk and Red SAS resemble the free Chl *a* SAS, and the areas, and thus the oscillator strengths, of the different Chls *a* are equal within 10%. This area constraint was instrumental in determining the branching ratios from Soret to the four different Chl *a* pools, and the trapping ratios.

2.3.2.1 Target analysis of anisotropic data

When in addition to magic angle (MA) data also parallel (VV) and perpendicular (VH) data are collected, more information is available to disentangle the complex kinetics, and estimate the SAS. In such an extended target analysis the magic angle concentrations c_l^{III} are multiplied by the anisotropic properties of the components.

$$\begin{bmatrix} MA(t,\lambda) \\ VV(t,\lambda) \\ VH(t,\lambda) \end{bmatrix} = \sum_{l=1}^{n_{comp}} c_l^{III} SAS_l(\lambda) \begin{bmatrix} 1 \\ 1+2r_l \\ 1-r_l \end{bmatrix} \tag{18}$$

Note that here the anisotropy r_1 is assumed to be constant. When an anisotropy decay rate is present, each isotropic exponential decay has to be multiplied by the associated anisotropy decay rate before the convolution with the IRF[49,50]. Figure 6 shows a representative trace from Kleima et al.[31] who used a biexponential anisotropy decay

$$r(t) = A_1 \exp(-t/\tau_1) + A_2 \exp(-t/\tau_2) + r_\infty \tag{19}$$

An isotropic lifetime of ≈4.2 ns was estimated from this target analysis, in combination with depolarization times of about 7 and 350 ps, which are clearly visible in the data measured on the different time scales (Figure 6).

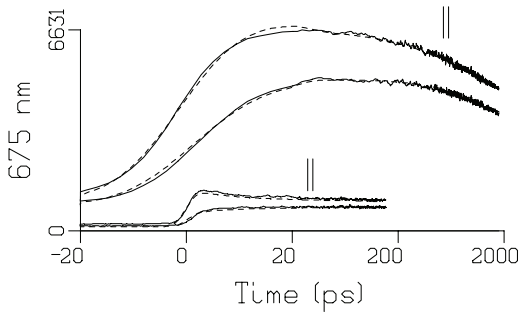

Figure 6. *Parallel (‖, upper curves) and perpendicular (lower curves) time traces measured at 675 nm after exciting PCP at 660 nm, from Kleima et al.[31]. The smaller curves were measured on the shortest time base. The dashed lines indicate the fit. Note that the time axis is linear from –20 to +20 ps relative to the maximum of the IRF, and logarithmic thereafter.*

2.3.3 Spectral modeling

SAS can sometimes be fitted with a spectral model consisting of a skewed Gaussian in the energy domain ($\bar{\nu} = 1/\lambda$):

$$SAS(\bar{\nu}) = \bar{\nu}^5 S_{\max} \exp(-\ln(2)\{\ln(1 + 2b(\bar{\nu} - \bar{\nu}_{\max})/\Delta\bar{\nu})/b\}^2) \tag{20}$$

where the parameter $\bar{\nu}_{max}$ is the Franck-Condon wavenumber of maximum emission. The FWHM is given by $\Delta\bar{\nu}_{1/2} = \Delta\bar{\nu}\sinh(b)/b$. Note that with skewness parameter b equal to zero the expression simplifies to a Gaussian. The average wavenumber of this function is given by

$$\bar{\nu}_{av} = \bar{\nu}_{\max} + \frac{\Delta\bar{\nu}}{2b}\left(\exp\left(-\frac{3b^2}{4\ln(2)}\right) - 1\right) \tag{21}$$

The spectral evolution description of solvation approximates a gradual change with an average spectral change associated with a time constant. Alternatively, solvation occurring on sub-ps timescales can be described using a time-dependent shift of $\bar{\nu}_{max}$ [51,52]. This requires data with a higher time and wavelength resolution, e.g. from fluorescence

upconversion[51,53,54], for which excitation intensities are required that are too. high for the study of photosynthetic systems.

Figure 7 shows DAS estimated from the multiexponential decay of the excited state of the D85S mutant of bacteriorhodopsin. Both DAS possessed almost identical shapes, and thus show no evidence for solvation on the picosecond timescale. The DAS were well described by a skewed Gaussian, and the multiexponentiality is ascribed to heterogeneity of the protein.

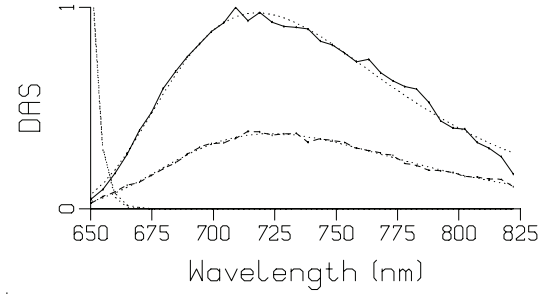

Figure 7. *Decay Associated Spectra from global analysis of bacteriorhodopsin mutant D85S excited at 635 nm, from van Stokkum et al.[14]. Key: 5.2 ps (solid), 19.1 ps (dashed), scatter (dotted). Fits of the DAS using a skewed Gaussian shape are indicated by dots. The estimated* $\bar{\nu}_{av}$ *were both 13000* cm^{-1} *and the FWHM was 2540* cm^{-1}.

2.3.4 Usage of the singular value decomposition

The matrix structure of the streak data enables the usage of matrix decomposition techniques, in particular the singular value decomposition (SVD). Formally the data matrix can be decomposed as

$$\psi(t,\lambda) = \sum_{l=1}^{m} u_l(t) s_l w_l(\lambda) \tag{22}$$

where u_l and w_l are the left and right singular vectors, s_l the sorted singular values, and m is the minimum of the number of rows and columns of the data matrix. The singular vectors are orthogonal, and provide an optimal least squares approximation of the matrix.

From the SVD the rank of the data matrix can be estimated, as judged from the singular values and singular vector pairs significantly different from noise. This rank corresponds to the number of spectrally and temporally independent components. When the data matrix has not been corrected for dispersion, this is no longer true. Furthermore SVD of the residual matrix is useful to diagnose shortcomings of the model used, or systematic errors in the data. Figure 8a-c depicts the SVD of the trimeric PSI data, where four singular values and singular vector pairs are significantly different from noise. These first four singular values account for 99.923% of the variance of the data matrix. The left and right

singular vectors are both linear combinations of the true concentration profiles and SAS, and are hard to interpret. The first pair (squares) represents a kind of average. The SVD of the residual matrix (shown in Figure 8d-f) shows that its singular values are comparable to the noise singular values in Figure 8c, and that there is no clear structure in the first singular vector pair. The sum of squares of the residuals is 0.088% of the variance of the data matrix, indicating a small lack of fit. The root mean square error of the fit was 41, which is 0.5% of the peak in Figure 1.

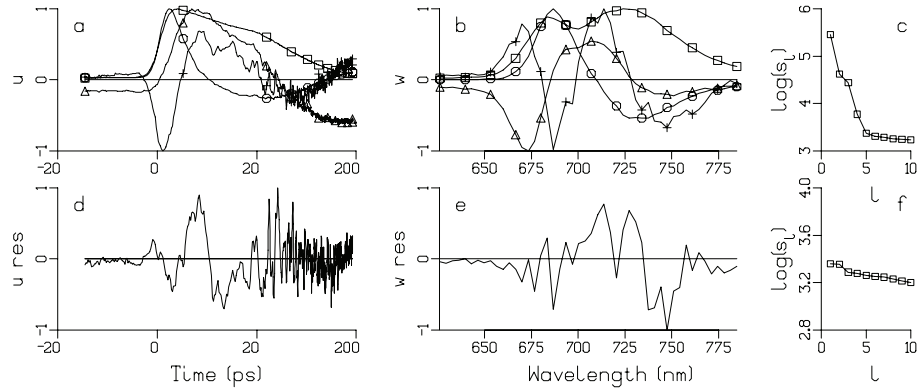

Figure 8. *SVD of the PSI trimer data matrix (top) and matrix of residuals (bottom). (a) first four (order squares, circles, triangles, plus symbols) left singular vectors* u_l*, (b) first four right singular vectors* w_l*, (c) first ten singular values* s_l *on a logarithmic scale, (d) first left singular vector* $u_{res,1}$*, (e) first right singular vector* $w_{res,1}$*, (f) first ten singular values* $s_{res,1}$ *on a logarithmic scale.*

2.4 Conclusions

When comparing the present state of the art with the excellent review of Campillo and Shapiro[7] the most striking developments are the utilization of the horizontal dimension, in particular using a spectrograph, and the improvement of the data analysis methods. The collection and analysis of true spectrotemporal measurements with (sub)ps time resolution using low excitation intensities have become routine, and the promises of the technique have largely been fulfilled. It has now become possible to functionally describe the complicated energy transfer and trapping processes in photosynthetic complexes with the help of a compartmental model, characterized by SAS and microscopic rate constants. The streak measurements of spectral evolution of fluorescence can be combined with fluorescence upconversion measurements[21,25] to extend the number of time scales covered, or with femtosecond difference absorption measurements[55] to uncover also nonemitting states. The complementary information contained in data obtained with different techniques is optimally extracted in a simultaneous target analysis.

Acknowledgements

Marloes Groot, Kate Mullen, Arie van Hoek, Janne Ihalainen and Rienk van Grondelle are thanked for critically reading the text. This research was supported by the Netherlands Organization for Scientific Research (NWO) via the Dutch Foundation of Earth and Life Sciences (ALW) and via the Netherlands Organization of Fundamental Research of Matter (FOM).

References

1. van den Berg, P. A. W., Mulrooney, S. B., Gobets, B., Van Stokkum, I. H. M., Van Hoek, A., Williams, C. H. and Visser, A. J. W. G. (2001), *Protein Science* **10**, 2037-2049.
2. Sauer, K. and Debreczeny, M. 1996. Fluorescence. In Biophysical Techniques in Photosynthesis, editors: Amesz, J. and Hoff, A. J., Kluwer Academic Press, Dordrecht. p. 41-61.
3. Petushkov, V. N., van Stokkum, I. H. M., Gobets, B., van Mourik, F., Lee, J., van Grondelle, R. and Visser, A. (2003), *J. Phys. Chem. B* **107**, 10934-10939.
4. Jimenez, R. and Fleming, G. R. 1996. Ultrafast spectroscopy of photosynthetic systems. In Biophysical Techniques in Photosynthesis, editors: Amesz, J. and Hoff, A. J., Kluwer Academic Press, Dordrecht. p. 63-73.
5. Ito, T., Hiramatsu, M., Hosoda, M. and Tsuchiya, Y. (1991), *Rev. Sci. Instrum.* **62**, 1415-1419.
6. Gobets, B., van Stokkum, I. H. M., Rogner, M., Kruip, J., Schlodder, E., Karapetyan, N. V., Dekker, J. P. and van Grondelle, R. (2001), *Bioph. J.* **81**, 407-424.
7. Campillo, A. J. and Shapiro, S. L. (1983), *IEEE J. Quantum Electron.* **19**, 585-603.
8. Freiberg, A. and Saari, P. (1983), *IEEE J. Quantum Electron.* **19**, 622-630.
9. Ohtani, H., Ishikawa, M., Itoh, H., Takiguchi, Y., Urakami, T. and Tsuchiya, Y. (1990), *Chem. Phys. Lett.* **168**, 493-498.
10. Haacke, S., Vinzani, S., Schenkl, S. and Chergui, M. (2001), *ChemPhysChem* **2**, 310-315.
11. Kamiya, N., Ishikawa, M., Kasahara, K., Kaneko, M., Yamamoto, N. and Ohtani, H. (1997), *Chem. Phys. Lett.* **265**, 595-599.
12. Ohtani, H., Kaneko, M., Ishikawa, M., Kamiya, N. and Yamamoto, N. (1999), *Chem. Phys. Lett.* **299**, 571-575.
13. Ohtani, H., Naramoto, S. and Yamamoto, N. (1994), *Photochem. Photobiol.* **60**, 394-398.
14. van Stokkum, I. H. M., Gobets, B., Gensch, T., van Mourik, F., Hellingwerf, K. J., van Grondelle, R. and Kennis, J. T. M. (2006), *Photochem. Photobiol.* **82**, 380-388.
15. Gilmore, A. M., Itoh, S. and Govindjee (2000), *Phil. Trans. R. Soc. Lond. B* **355**, 1371-1384.
16. Gilmore, A. M., Larkum, A. W. D., Sallh, A., Itoh, S., Shibata, Y., Bena, C., Yamasaki, H., Papina, M. and Van Woesik, R. (2003), *Photochem. Photobiol.* **77**, 515-523.
17. Gilmore, A. M., Matsubara, S., Ball, M. C., Barker, D. H. and Itoh, S. (2003), *Plant Cell Environ.* **26**, 1021-1034.
18. Donovan, B., Walker, L. A., Kaplan, D., Bouvier, M., Yocum, C. F. and Sension, R. J. (1997), *J. Phys. Chem. B* **101**, 5232-5238.
19. van Mourik, F., Frese, R. N., van der Zwan, G., Cogdell, R. J. and van Grondelle, R. (2003), *J. Phys. Chem. B* **107**, 2156-2161.
20. Andrizhiyevskaya, E. G., Frolov, D., van Grondelle, R. and Dekker, J. P. (2004), *Phys. Chem. Chem. Phys.* **6**, 4810-4819.

21. Gobets, B., Kennis, J. T. M., Ihalainen, J. A., Brazzoli, M., Croce, R., van Stokkum, L. H. M., Bassi, R., Dekker, J. P., van Amerongen, H., Fleming, G. R. and van Grondelle, R. (2001), *J. Phys. Chem. B* **105**, 10132-10139.
22. Ihalainen, J. A., Jensen, P. E., Haldrup, A., van Stokkum, I. H. M., van Grondelle, R., Scheller, H. V. and Dekker, J. P. (2002), *Bioph. J.* **83**, 2190-2201.
23. Ihalainen, J. A., Klimmek, F., Ganeteg, U., van Stokkum, I. H. M., van Grondelle, R., Jansson, S. and Dekker, J. P. (2005), *FEBS Lett.* **579**, 4787-4791.
24. Ihalainen, J. A., van Stokkum, I. H. M., Gibasiewicz, K., Germano, M., van Grondelle, R. and Dekker, J. P. (2005), *Biochim. Biophys. Acta* **1706**, 267-275.
25. Kennis, J. T. M., Gobets, B., van Stokkum, I. H. M., Dekker, J. P., van Grondelle, R. and Fleming, G. R. (2001), *J. Phys. Chem. B* **105**, 4485-4494.
26. Andrizhiyevskaya, E. G., Frolov, D., van Grondelle, R. and Dekker, J. P. (2004), *Biochim. Biophys. Acta* **1656**, 104-113.
27. Ihalainen, J. A., Croce, R., Morosinotto, T., van Stokkum, I. H. M., Bassi, R., Dekker, J. P. X. and van Grondelle, R. (2005), *J. Phys. Chem. B* **109**, 21150-21158.
28. Ihalainen, J. A., D'Haene, S., Yeremenko, N., van Roon, H., Arteni, A. A., Boekema, E. J., van Grondelle, R., Matthijs, H. C. P. and Dekker, J. P. (2005), *Biochemistry* **44**, 10846-10853.
29. Monshouwer, R., Abrahamsson, M., van Mourik, F. and van Grondelle, R. (1997), *J. Phys. Chem. B* **101**, 7241-7248.
30. Palacios, M. A., de Weerd, F. L., Ihalainen, J. A., van Grondelle, R. and van Amerongen, H. (2002), *J. Phys. Chem. B* **106**, 5782-5787.
31. Kleima, F. J., Hofmann, E., Gobets, B., van Stokkum, I. H. M., van Grondelle, R., Diederichs, K. and van Amerongen, H. (2000), *Bioph. J.* **78**, 344-353.
32. Uhring, W., Zint, C. V., Summ, P. and Cunin, B. (2003), *Rev. Sci. Instrum.* **74**, 2646-2653.
33. Knippels, G. M. H., van de Pol, M. J., Pellemans, H. P. M., Planken, P. C. M. and van der Meer, A. F. G. (1998), *Opt. Lett.* **23**, 1754-1756.
34. Martinez, O. E. (1987), *IEEE J. Quantum Electron.* **23**, 59-64.
35. Hebling, J. (1996), *Opt. Quantum Electron.* **28**, 1759-1763.
36. Schiller, N. H. and Alfano, R. R. (1980), *Opt. Commun.* **35**, 451-454.
37. Wiessner, A. and Staerk, H. (1993), *Rev. Sci. Instrum.* **64**, 3430-3439.
38. Bradley, D. J. and New, G. H. C. (1974), *Proc. IEEE* **62**, 313-345.
39. Zavoisky, E. K. and Fanchenk.Sd (1965), *Appl. Opt.* **4**, 1155-1167.
40. Jaanimagi, P. A., Dasilva, L., Gregory, G. G., Hestdalen, C., Kiikka, C. D., Kotmel, R. and Richardson, M. C. (1986), *Rev. Sci. Instrum.* **57**, 2189-2191.
41. Gobets, B. 2002. The life and times of Photosystem I. Excitation energy transfer and trapping unravelled. [PhD thesis]: Vrij Universiteit Amsterdam. 215 p.
42. Greene, B. I. and Farrow, R. C. (1983), *Chem. Phys. Lett.* **98**, 273-276.
43. Bühler, C. A., Graf, U., Hochstrasser, R. A. and Anliker, M. (1998), *Rev. Sci. Instrum.* **69**, 1512-1518.
44. Holzwarth, A. 1996. Data Analysis of Time-Resolved Measurements. In Biophysical Techniques in Photosynthesis, editors: Amesz, J. and Hoff, A. J., Kluwer Academic Press, Dordrecht. p. 75-92.
45. van Stokkum, I. H. M., Larsen, D. S. and van Grondelle, R. (2004), *Biochim. Biophys. Acta* **1657**, 82-104.
46. van Stokkum, I. H. M., Larsen, D. S. and van Grondelle, R. (2004), *Biochim. Biophys. Acta* **1658**, 262-262.
47. van Stokkum, I. H. M. 2005. Global and target analysis of time resolved spectra. In Lecture notes Troisième Cycle de la Physique en Suisse Romande, March 14-24, p. 88.
48. van Stokkum, I. H. M. and Bal, H. E. (2006), *Concurr. Comp. Pract. Exp.* **18**, 263-269.
49. Beechem, J. M. (1989), *Chem. Phys. Lip.* **50**, 237-251.
50. Yatskou, M. M., Koehorst, R. B. M., van Hoek, A., Donker, H. and Schaafsma, T. J. (2001), *J. Phys. Chem. A* **105**, 11432-11440.

51. Horng, M. L., Gardecki, J. A., Papazyan, A. and Maroncelli, M. (1995), *J. Phys. Chem.* **99**, 17311-17337.
52. Vilchiz, V. H., Kloepfer, J. A., Germaine, A. C., Lenchenkov, V. A. and Bradforth, S. E. (2001), *J. Phys. Chem. A* **105**, 1711-1723.
53. Pal, S. K., Peon, J. and Zewail, A. H. (2002), *Proc. Natl. Acad. Sci. U. S. A.* **99**, 1763-1768.
54. Vengris, M., van der Horst, M. A., Zgrablic, G., van Stokkum, I. H. M., Haacke, S., Chergui, M., Hellingwerf, K. J., van Grondelle, R. and Larsen, D. S. (2004), *Bioph. J.* **87**, 1848-1857.
55. Groot, M. L., Pawlowicz, N. P., van Wilderen, L., Breton, J., van Stokkum, I. H. M. and van Grondelle, R. (2005), *Proc. Natl. Acad. Sci. U. S. A.* **102**, 13087-13092.

Chapter 3

Ultrafast resonance energy transfer from a site-specifically attached fluorescent chromophore reveals the folding of the N-terminal domain of CP29

based on:
B. van Oort, S. Murali, E. Wientjes, R.B.M. Koehorst, R.B. Spruijt, A. van Hoek, R. Croce, H. van Amerongen, submitted. Ultrafast resonance energy transfer from a site-specifically attached fluorescent chromophore reveals the folding of the N-terminal domain of CP29.

Abstract

The photosynthetic minor antenna complex CP29 of higher plants was singly mutated, overexpressed in *E. coli*, selectively labeled with the fluorescent dye TAMRA at three positions in the N-terminal domain, and reconstituted with its natural pigments. Picosecond fluorescence experiments revealed rapid excitation energy transfer (~20 ps) from TAMRA covalently attached to a cysteine at either position 4 or 97 (near the beginning and end of the N-terminal domain) to the chlorophylls in the hydrophobic part of the protein. This indicates that the N-terminus is folded back on the hydrophobic core. In 20% of the complexes, efficient transfer was lacking, indicating that the N-terminus can adopt different conformations. Time-resolved polarized fluorescence measurements demonstrate that the non-transferring conformations only allow restricted rotational motion of the dye molecule. When TAMRA was attached to a cysteine at position 40, the overall transfer efficiency was far lower, reflecting a larger distance to the hydrophobic region.

3.1 Introduction

In higher plants sunlight is harvested by two multiprotein complexes, photosystem (PS) I and II and it is used to drive electron transfer reactions. The photosystems are composed of a core complex, which contains all the cofactors of the electron transport chain and of an external antenna, which harvests light and transfers excitation energy to the reaction centers. In Photosystem II the antenna system consists of 4 complexes: LHCII, the major antenna subunit, present as a trimer in the membrane, and three minor monomeric complexes CP24, CP26 and CP29. The minor complexes together contain 15% of the pigments of PSII and they are located between LHCII and the core proteins[1]. Besides playing a role in light harvesting they are also involved in photoprotective mechanisms (e.g. nonphotochemical quenching) that are used by plants to dissipate excess energy under high-light conditions[2-4]. It has been proposed that a change in structure of the minor complexes is responsible for a switch between the light-harvesting state and the quenching state[2].

Amongst the three minor complexes, CP29, the product of the Lhcb4 gene, is the best characterized one. The spectroscopic properties of each pigment in each binding site have been determined with the help of mutation analysis followed by *in vitro* reconstitution[5-8] and by applying different spectroscopic techniques[9-12]. Several time-resolved studies have been performed on the complex, allowing to elucidate the energy transfer rates and pathways between Chls and between carotenoids and Chls[4,13-18]. CP29 is the largest of the outer antenna complexes of PSII and it is special because it contains an

unusually long N-terminal domain (~100 amino acids, see Figure 1). Under cold stress the N-terminus becomes phosphorylated at Thr83[19] increasing the resistance of the plants to cold stress[20,21]. It was demonstrated that phosphorylation leads to a change in conformation of the protein[22], possibly favoring the dissipative form. More recently, a second phosphorylation site, corresponding to Thr6, was observed in the Lhcb4.2 gene product[23]. Although the structure of CP29 has not been resolved, the high sequence homology, especially in the transmembrane domain, suggests an organization similar to that of LHCII, the structure of which has been obtained at 2.5-2.72 Å[24,25]. However, no information is available about the organization of the N-terminal domain, which differs completely from that of LHCII.

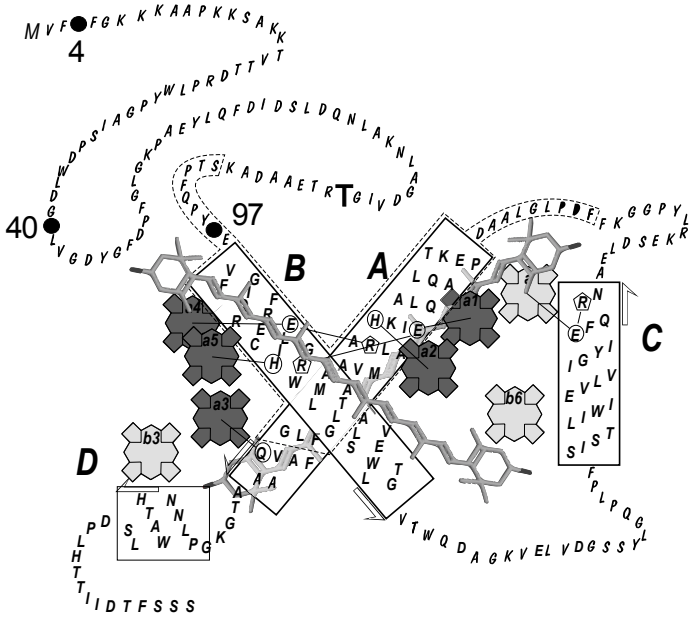

Figure 1. *Schematic representation of the structure of CP29 (sequence of Lhcb4.1 of Arabidopsis thaliana) with positions of Chl a (dark grey), positions of Chl a or b (light grey) and the two central carotenoids (grey)[5]. The black dots and numbers indicate the position of the labeled residues used in this work. The big T indicates the site of phosphorylation[19].*

The aim of the present work is to develop an alternative method to obtain structural and dynamical information on CP29 and in particular on its N-terminal domain. Mutagenesis techniques are used to produce single cysteine mutants at selected positions (4, 40 and 97) of the N-terminus. The mutated apoproteins were labeled with the fluorophore TAMRA, which can selectively be excited around 530-550 nm, and reconstituted with the natural pigments, chlorophylls *a* and *b* (Chl *a*/*b*) and carotenoids. In

principle TAMRA might influence the protein's structure but the effect is probably minor because protein folding of the homologous protein LHCII is not affected by attachment of a similar label[26]. With the use of picosecond fluorescence techniques, resonance energy transfer (FRET) was measured from TAMRA to the Chl molecules, providing information about distances between specific sites of the N-terminal domain and the chlorophyll molecules.

3.2 Materials and Methods

3.2.1 Construction and isolation of overexpressed CP29 apoprotein

Lhcb4.1 cDNA of *A. thaliana* (from Arabidopsis Biological Resource Center DNA Stock Center) was subcloned into a pT7-7 expression vector. The construct contains the sequence of the mature CP29 protein with an additional methionine at the N-terminus and a 6 His-tag at the C-terminus

Mutations were introduced using the Stratagene Quik Change Site Directed Mutagenesis Kit. First, the natural occurring cysteine (position 108) was replaced by alanine. On this template, cysteine mutations were introduced in the N-terminal peptide at position 4, 40, and 97. The constructs were checked by DNA-sequencing. The plasmids were amplified in the super competent *Escherichia coli* XL-1 Blue strain and the proteins overexpressed in the *E.coli* BL21(*DE3*) strain[27,28].

3.2.2 Pigment isolation, labeling and reconstitution of CP29-pigment complexes

Purified pigments were obtained from spinach thylakoids. Concentrations of pigments were determined spectroscopically; Chls as described by Porra[29] and Cars as described by Davies[30]. CP29 apoprotein mutants and wild-type were labeled with MTS-TAMRA, (2-((5(6)-Tetramethylrhodamine)carboxylamino)ethyl Methanethiosulfonate from TRC, Toronto, Canada), and purified from the excess of TAMRA using HPSEC and affinity chromatography on a His-Trap column[31]. Reconstitution and purification of protein-pigment complexes were performed as reported in ref. 15. The average labelling efficiency was 70 ± 20%. Concentrated stock solutions of the CP29, containing dodecyl β-D-maltoside (DM; 0.06 % W/V) and sucrose remaining from sucrose gradient purification, were diluted in sucrose-free DM buffer (0.06 % W/V + 10 mM Na_2HPO_4 pH 7.6) for the fluorescence measurements.

3.2.3 Steady-state spectra

Steady-state absorption spectra were recorded on a Varian Cary 5E spectrophotometer. Steady-state fluorescence emission spectra (535 nm excitation) and steady-state fluorescence excitation spectra (680 nm detection) were recorded on a Spex-Fluorolog 3.2.2 spectrofluorimeter (Jobin-Yvon).

3.2.4 Time-resolved fluorescence using the streak-camera setup

For the picosecond fluorescence measurements excitation was performed with a set of lasers and optical amplifiers from Coherent Inc., Santa Clara, CA, U.S.A. The output of a passively mode-locked titanium sapphire laser model Mira 900 (output wavelength 800 nm, average power 0.5 W, pulse width 130 fs, repetition rate 75.9 MHz) was used for seeding a regenerative amplifier model RegA 9000 (output wavelength 800 nm, average power 1.2 W, pulse width 130 fs, repetition rate 253 kHz). Continuous wave diode pumped solid-state Nd:YVO_4 lasers model Verdi V5 and Verdi V10 (wavelength 532 nm) were used for pumping the Mira and the RegA respectively. The output of the RegA fed an optical parametric amplifier (model OPA 9400). The average power output of the OPA was up to tens of mW at wavelengths ranging from 470 to 720 nm. Furthermore the frequency-doubled 800 nm light (400 nm), and a frequency doubler (APE GmbH, Berlin, Germany, model fs OPA-SHG) for the OPA output (then 210-360 nm wavelength) were available for excitation purposes. The light intensity was modulated with neutral density filters, and residual white light from the OPA was removed with an interference filter. The polarization was set vertical with a Berek polarizer (New Focus, San Jose, CA, USA model 5540), and further optimized using a Glan Taylor polarizer. A lens of 15 cm focal length then focused the light into the sample in a static fluorescence cuvette, resulting in a spot diameter of 150 μm. Care was taken to avoid internal reflections in the sample cells.

In front of the streak-camera an imaging spectrograph was mounted (Chromex, Albuquerque, NM, U.S.A model 250is). Fluorescence emission was collected from the sample cell and focused onto the input slit of the spectrograph using two identical achromatic lens assemblies (Sill Optics, Wendelstein, Germany, model UV APO special, f = 70 mm, d = 22 mm) placed in a complementary manner with a Glan Taylor polarizer (Leysop Ltd., Essex, England model GT20) and optionally an optical filter (to suppress scatter) in between. The polarizer was set at magic angle orientation. The spectrograph was equipped with a turret, carrying three gratings with different ruling and blaze wavelength. The output mirror of the spectrograph focused the output light directly onto the stripe-shaped (height 70 μm) cathode of the streak-camera (Hamamatsu Photonics K.K., Hamamatsu City, Japan model C5680 with model M5675 Synchroscan unit). Wavelength dispersion of the spectrograph was in a horizontal direction, the time dispersion of the

streak tube was in a vertical direction. Four time windows are available for the streak camera: 160, 800, 1500 and 2100 ps. Scale, linearity and curving of the time and wavelength axes were extensively treated in correction procedures using the following references: Fabry-Perot etalons, fixed wavelength light sources and a white light source (Optronic Laboratories, Orlando, FL, U.S.A. model 65A ultra precise current source with model OL 220C 200W quartz halogen tungsten reference lamp).

Spectral resolution is typically 2 nm, and temporal resolution ~1 ps. For more details on streak camera experiments and data analysis, see Chapter 2[32]. For the experiments described in this Chapter, the time window was 160 ps, and the spectral window ranged from 540 to 700 nm (using the grating with 50 grooves/mm ruling and 600 nm blaze).

3.2.5 Streak-camera data analysis

The streak-camera data were corrected for jitter if necessary, averaged, and background and shading corrected using the software package High Performance Digital Temporal Analyzer (HPDTA, version 6.4, Hamamatsu Photonics). The streak-camera images are two-dimensional data sets of fluorescence intensity as a function of time and wavelength. The images were sliced up into time traces of 6 nm width. These traces were fitted to a sum of exponentials. using global analysis, with software described in ref. 33. The resulting wavelength-dependent amplitudes provide the Decay-Associated Spectra (DAS).

3.2.6 Time-correlated-single photon counting

Time-correlated single photon counting was performed with a homebuilt setup, as described in ref. 34. Samples, placed in a static cuvette holder and maintained at 283 K, were excited with vertically polarized 540 nm pulses of around 0.2 ps duration at a repetition rate of 3.8 MHz, and measurements were done by collecting repeated sequences of 10 s vertically (parallel) and 10 s horizontal (perpendicular) polarized fluorescence emission. Fluorescence was collected through a Schott OG570 long pass filter, in combination with either a Schott IL585.1 interference filter (TAMRA fluorescence) or a Balzers 679nm interference filter (Chl fluorescence). The excitation density was reduced to obtain a count-rate below 30000 per second (sub-pJ pulse energy) and care was taken to minimize data distortion[35]. Data were acquired until the number of counts in the peak channel was ~15000. The instrument response function (~50 ps FWHM) was obtained at 585 nm with erythrosine B in water (80 ps fluorescence lifetime[36]), and at 679nm with pinacyanol iodide in methanol (6 ps fluorescence lifetime[37]). Data were corrected for background signal (less than 1%) by subtracting the signal of DM buffer measured directly after the sample.

Individual photons were detected by a microchannel plate photomultiplier, and arrival times were stored in 4096 channels (5 ps channel width) of a multichannel analyzer. Isotropic fluorescence decay curves $F_{iso}(t)$ were calculated from the decay curves of parallelly ($F_{//}(t)$) and perpendicularly ($F_{\perp}(t)$) polarized emission: $F_{iso}(t) = F_{//}(t) + 2gF_{\perp}(t)$, using the relative sensitivity g of the detection branch for parallelly and perpendicularly polarized light (g equals unity for this setup[38]). $F_{iso}(t)$ was fitted to a sum of exponentials, convoluted with the instrument response function[39]. Time resolved anisotropy was analyzed by global fitting of $F_{//}(t)$ and $F_{\perp}(t)$, with fit parameters τ_j (fluorescence lifetimes), a_j (fluorescence decay amplitudes), φ_k (anisotropy correlation times), β_k (anisotropy amplitudes) and β_{inf} (residual anisotropy), using fit functions

$$I_{//}(t) = \tfrac{1}{3}\sum_j a_j e^{-t/\tau_j} * \left(1 + 2\left(\beta_{\inf} + \sum_k \beta_k e^{-t/\varphi_k}\right)\right)$$

$$I_{\perp}(t) = \tfrac{1}{3}\sum_j a_j e^{-t/\tau_j} * \left(1 - \left(\beta_{\inf} + \sum_k \beta_k e^{-t/\varphi_k}\right)\right)$$

convoluted with the instrument response function, as described in detail by Visser et al.[40]. The quality of a fit was judged by the chi-square value and by the quality of residuals and autocorrelation thereof.

3.3 Results

The naturally occurring cysteine (position 108) was replaced by alanine, and single-point mutations were introduced in the N-terminal loop of CP29 at 3 different positions. In the three mutated proteins, a cysteine replaced the wild-type amino acids at positions 4, 40 and 97 respectively (see also Figure 1) and this cysteine was labeled with TAMRA with an average efficiency of 70 ± 20%. For all complexes, absorption and steady-state excitation and emission spectra were measured as well as time-resolved fluorescence kinetics upon excitation in the TAMRA absorption region. Below the results on labeled CP29 mutated at position 4 (CP29-4) will first be presented in detail. The data analysis of the other complexes was done in an analogous way and the results will be summarized afterwards.

3.3.1 Absorption

The absorption spectra of wild-type CP29 (CP29-WT) and labeled CP29-4 are given in Figure 2A. The spectra are nearly identical over the entire wavelength range with the exception of the region around 550 nm, where the labeled protein shows the additional absorption of TAMRA. For the time-resolved measurements an excitation wavelength of

535 nm (and not 550 nm which corresponds to the absorption maximum of TAMRA) was used in order to avoid overlap of the Raman scattering peak with the Chl *a* fluorescence. For the labeled complex 35 ± 5% of the absorption at 535 nm is due to TAMRA, whereas 65 ± 5% is due to Chl *b* and Chl *a*. Therefore, in the steady-state and time-resolved fluorescence measurements it can be expected that at least 65% of the Chl fluorescence is due to directly excited Chl molecules.

3.3.2 Steady-state fluorescence emission

The fluorescence emission spectra of CP29-WT and CP29-4 after excitation at 535 nm are shown in Figure 2B. For CP29-4 some fluorescence can be discerned around 580 nm which is due to TAMRA but the majority of the fluorescence stems from Chl *a*, peaking around 680 nm. The shape of the fluorescence spectrum in the Chl Q_y region is identical for both complexes, indicating that the TAMRA fluorescence is negligible around 680 nm. However, there is a clear increase of the Chl *a* fluorescence intensity for CP29-4, which must be ascribed to excitation energy transfer from TAMRA to Chl *a* and *b*. It should be noted that around 100% energy transfer from Chl *b* to Chl *a* occurs on a time scale of hundreds of femtoseconds to several picoseconds[14,17,18] and therefore, Chl *b* fluorescence is

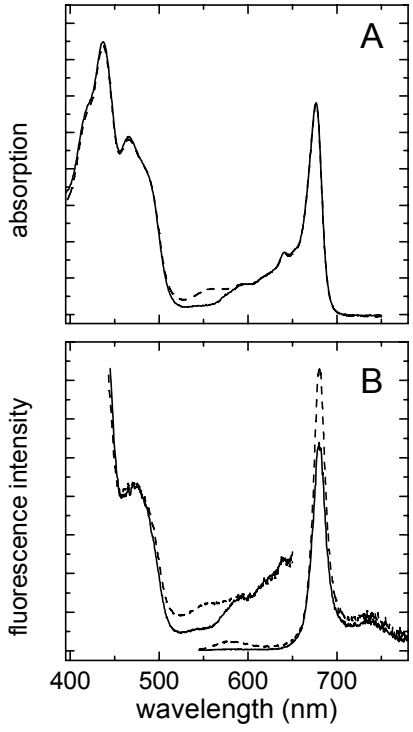

Figure 2. *Steady-state spectra of CP29-WT (solid) and CP29-4 (dashed). A) Absorption spectra normalized at 676 nm. B) Fluorescence emission (right, excitation at 535 nm) and excitation (left, detection at 680 nm) spectra normalized to the Chl concentration.*

virtually absent from the steady-state emission spectrum. The increase of Chl *a* fluorescence is substantially larger than the amount of TAMRA fluorescence around 580 nm, indicating that a large fraction of the excitations that are created on TAMRA has been transferred. At 535 nm the amount of directly excited Chl was estimated to be around 65 ± 5% whereas comparison of the intensities of the two fluorescence spectra at 680 nm indicates that approximately 75% of the fluorescence is due to directly excited Chl. This confirms that FRET from TAMRA to Chl is substantial but not "perfect", i.e. less than 100%.

3.3.3 Steady-state fluorescence excitation spectra

The fluorescence excitation spectra of CP29-WT and CP29-4 upon detection at 680 nm are given in Figure 2B. At 680 nm Chl fluorescence is detected selectively. The labeled complex shows a shoulder at 550 nm, which can be ascribed to TAMRA that is transferring excitation energy to Chl. Exact quantification of the energy transfer is complicated by the Raman scatter contribution upon excitation at 550 nm, which may not have been completely removed with background subtraction. The emission spectra indicate a transfer efficiency of ~80%. From the steady-state spectra it cannot be determined whether in all complexes the transfer efficiency is 80% or whether there is heterogeneity in the efficiencies. In order to resolve this issue, time-resolved fluorescence measurements were performed.

3.3.4 Time-resolved streak-camera fluorescence measurements

In Figure 3A the time-resolved fluorescence at 585 nm (TAMRA) is shown for CP29-4 and CP29 apoprotein which was labeled at the 4 position (apo-4). The apoprotein shows a decay of hundreds of picoseconds. This is faster than the 3.2 ns of TAMRA in methanol (Table 1). So TAMRA, bound to apo-4 is quenched, presumably by the protein environment (because the protein does not contain pigments, quenching due to FRET can not occur). Fluorescence quenching by a protein environment has been reported before for TAMRA and similar dyes[41,42]. CP29-4 shows much faster decay than apo-4, which must be due to FRET to the Chls. The time-resolved fluorescence of Chl *a* at 680 nm is shown in Figure 3A; a substantial amount of fluorescence arises from direct Chl excitation. Also a rise component can be observed on a time scale of several tens of picoseconds, which is due to FRET from TAMRA to Chl.

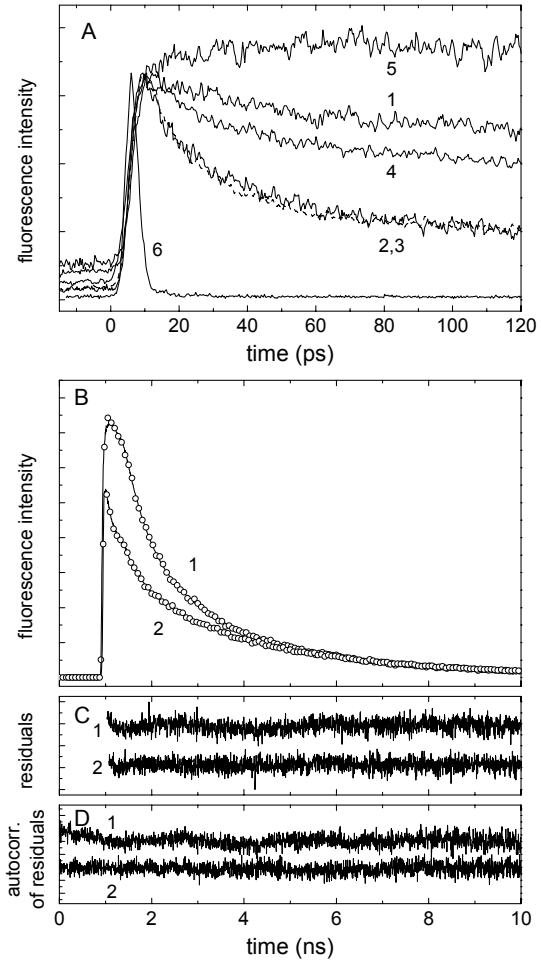

Figure 3. *Time-resolved fluorescence kinetics. A) Measured by streak camera (averaged over 565-605 nm, excited at 535 nm): apo-4 (1), CP29-4 (2, solid), CP29-97 (3, dashed), CP29-40 (4) and a trace of mutant CP29-4 averaged over 665 - 705 nm (5). Curve 6 represents the excitation pulse. B) Measured by TCSPC (detected at 680 nm, excited at 540 nm): experimental curves (markers for every 15th data point) and fitted curves (lines) of apo-4 (1) and CP29-4 (2), scaled differently for presentation purposes. C) residuals of the fits. D) autocorrelation of the residuals. C and D have offsets for presentation purpose*

Table 1. *Results of fitting TCSPC fluorescence decay curves of TAMRA in methanol (MeOH), attached to the apoproteins, and attached to holoproteins: Fluorescence lifetimes (τ) and relative amplitudes (between square brackets).*

	MeOH	apo-4	CP29-4	CP29-40	CP29-97
τ_1 (ns)	3.2 [1]	0.34 [0.54]	0.020 [0.76]	0.078 [0.37]	0.019 [0.77]
τ_2 (ns)	-*	1.46 [0.32]	0.204 [0.12]	0.323 [0.22]	0.206 [0.09]
τ_3 (ns)	-*	3.81 [0.14]	1.39 [0.05]	1.35 [0.24]	1.49 [0.06]
τ_4 (ns)	-*	-*	3.81 [0.07]	3.48 [0.17]	3.92 [0.09]

* *not observed*

Figure 4 shows the result of a global analysis of the fluorescence kinetics. The fluorescence of apo-4 decays mono-exponentially with a decay time of ~360 ps (note that time window in this experiment is only 200 ps, TCSPC measurements below show the presence of some additional slow components with small amplitudes) The data of the reconstituted, labeled mutants were each globally fitted with 2 time constants. In the TAMRA region the spectrum of CP29-4 shows a decrease in intensity with a time constant of 19 ps and a concomitant rise is observed in the Chl *a* region. This can be interpreted as energy transfer from TAMRA to Chl with a time constant of 19 ps, although it should be kept in mind that there is also some contribution from protein quenching to this time constant. Thus the real transfer time (τ) depends on the observed transfer time (τ_{obs}), and on the rate of protein quenching (k_q): $\tau^{-1} = \tau_{obs}^{-1} - k_q$. However, the rate of quenching by the protein is considerably slower ((~360 ps)$^{-1}$ in apo-4) than τ_{obs}^{-1}, so the real transfer time is probably only slightly slower (~5%) than the observed transfer time. The area of the decaying component in the TAMRA region is larger than that of the (negative) rise component in the Chl region. This is due to some singlet-singlet annihilation of Chl excited states. Annihilation takes place when a laser pulse leads to multiple excitations within a single CP29 complex. A singlet excited state can then act as a mobile quencher for other singlet excited states in the same complex, resulting in an additional fluorescence decay component. At the applied light intensities (approximately 10 mW, lower intensities gave a too weak signal) some annihilation takes place. Annihilation in CP29 is expected to result in a decay component of tens of picoseconds[43], which is close to the observed energy transfer time. Therefore annihilation may partly mask the amplitude of the rise of Chl fluorescence due to FRET. However, the transfer time is almost identical to the one measured by TCSPC in the absence of annihilation (see below). Therefore, annihilation appears to have a relatively small effect on the observed transfer time. The second spectrum in Figure 4 decays with a time constant of 3.3 ns, reflecting the "normal" excited-state decay of TAMRA and Chl *a*. There are several additional points to be noticed. 1) A fraction of the TAMRA molecules is not transferring its energy (~15%). This is in rather good agreement with the transfer efficiency estimated from the steady-state fluorescence measurements. Apparently, there is some structural heterogeneity and different conformations are present. 2) The fluorescence spectrum of the non-transferring (slowly decaying) TAMRA molecules is red-shifted with respect to that of the transferring molecules (see inset in Figure 4), indicating that the non-transferring molecules are relatively far away from the Chl molecules and are in a more hydrophilic environment. Alternatively, the red-shift can be caused by slow solvent relaxation that can only occur in the absence of fast excitation transfer. 3) A fit with only two components represents an oversimplification of the real situation (see also below) but clearly demonstrates that a large fraction of the excitations are transferred with a time constant of ~20 ps.

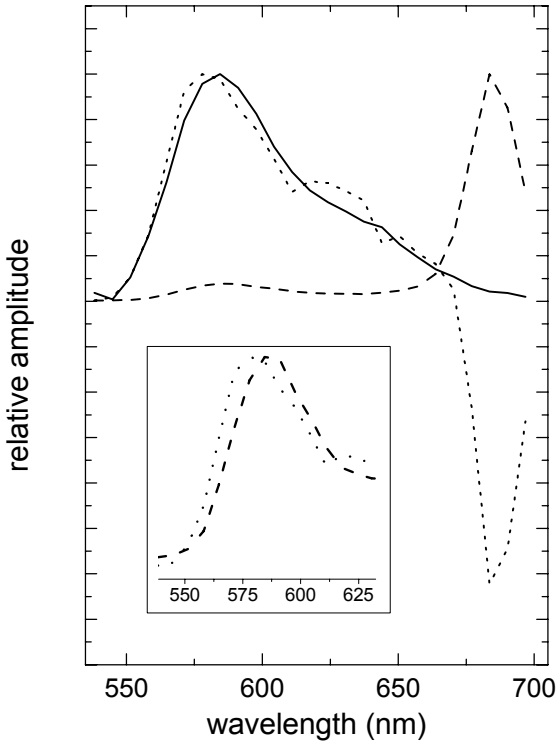

Figure 4. *Decay Associated Spectra (DAS) resulting from global analysis of streak images of apo-4 (solid line, τ = 360 ps), and CP29-4 (dotted line, τ = 19 ps [5.0]; dashed line, τ = 3.3 ns [1]), normalized to the maximum. The inset shows the 19 ps [0.38] and 3.3 ns [1] components normalized to the maximum in this wavelength region. Scaling factors of each DAS are shown between square brackets.*

Table 2. *Results of global fitting of fluorescence decay curves recorded between 540 and 700 nm, measured with the streak-camera setup: Fluorescence lifetimes (τ) and relative areas under the DAS of TAMRA attached to apo-4 and holoproteins*

	apo-4	CP29-4	CP29-40	CP29-97
τ_1 (ns)	0.36 [1]	0.019 [0.73]	0.029 [0.42]	0.019 [0.76]
τ_2 (ns)	-*	3.3 [0.27]	3.3 [0.58]	3.6 [0.24]

* *not observed*

3.3.5 Time-correlated single photon counting measurements

Time-resolved measurements of CP29-4 were also performed with the TCSPC technique, which offers higher S/N but lower time resolution. Upon detection at 585 nm decay times of 20 ps (76%), 204 ps (12%), 1.39 ns (5%) and 3.81 ns (7%) were obtained (see also Figure 3B and Table 1). The first component is in good agreement with the streak-camera results, which confirms that a large fraction of the excitations is rapidly transferred to the Chl molecules. Possibly also the 204 ps and 1.39 ns time constants correspond to energy transfer to the Chls but there is no unambiguous proof for that because similar rise times are

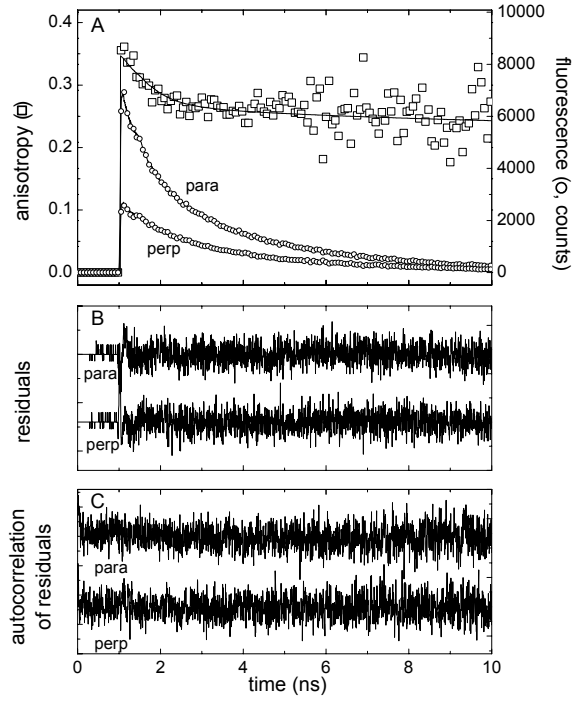

Figure 5. *Fluorescence anisotropy kinetics measured by TCSPC (detected at 585 nm, excited at 540 nm). A) Anisotropy decay curve (squares) and decay curves of parallelly (para) and perpendicularly (perp) polarized fluorescence (markers for every 15th point) and fitted curves (lines) of CP29-4. B) Residuals of the global fit of the polarized fluorescence decay curves. C) Autocorrelation of the residuals. B and C have offsets for presentation purpose.*

Table 3. *Results of fitting TCSPC anisotropy decays of TAMRA in methanol and bound to the reconstituted mutants: Anisotropy correlation times (φ_i), with amplitudes in square brackets, and residual anisotropy (β_{inf}).*

	methanol	CP29-4	CP29-40	CP29-97
φ_1 (ns)	0.16 [0.34]	0.55 [0.07]	0.80 [0.04]	0.48 [0.04]
φ_2 (ns)	-*	7.0 [0.03]	4.2 [0.02]	11 [0.07]
β_{inf}	0.00	0.24	0.26	0.23

* *not observed*

not observed in the Chl region. Alternatively, these decay processes might be due to direct quenching of TAMRA (see above). When TAMRA is measured in apo-4, the decay times are 336 ps (54%), 1.46 ns (32%) and 3.81 ns (14%). It is interesting to note that the 336 ps decay time is close to the 360 ps that was obtained from a global analysis fit of the streak-camera data.

The fluorescence anisotropy of TAMRA in CP29-4 was determined using the TCSPC setup and is given in Figure 5. The anisotropy was analyzed by global fitting of the parallelly and perpendicularly polarized fluorescence decay curves, as described in the

Materials and Methods section. Anisotropy correlation times of 550 ps (with amplitude 0.07) and 7 ns (with amplitude 0.03) and a residual anisotropy value of 0.24 (Table 3) were obtained. It should be noted that the polarized fluorescence decay curves are fitted in a non-associative way, i.e. there is no correlation assumed between the isotropic decay times and the anisotropy correlation times. Although this is not necessarily the case, associative fitting does not lead to meaningful results. However, the observed correlation times are so slow that they cannot originate from TAMRA molecules that transfer to Chl, because fluorescence of those molecules disappears in tens of picoseconds, and therefore hardly contributes to the anisotropy decay. So the observed anisotropy correlation times and the residual anisotropy originate from non-transferring TAMRA molecules, which demonstrates that the rotational motion of these molecules is strongly restricted. This indicates that the N-terminus for this subset of conformations adopts a rather static structure. No conclusion can be drawn about the dynamics in the case of fast energy transfer.

3.3.6 Labeled CP29 mutants 97 and 40

The results of time-resolved streak-camera measurements on labeled CP29-97 are very similar to those obtained for labeled CP29-4 (Figure 3A and Table 2). Global analysis with 2 components leads to lifetimes of 18.6 ps (transfer) and 3.6 ns (overall excited-state decay). TCSPC data of CP29-97 show four decay components in the TAMRA fluorescence region: 19 ps (77%), 206 ps (9%), 1.49 ns (6%) and 3.92 ns (9%) (see Table 1). The anisotropy data reveal two correlations times of 479 ps (amplitude 0.04) and 11 ns (amplitude 0.07) and a residual anisotropy of 0.23 (see Table 3). These results are again similar to those of CP29-4.

Figure 3A also shows the fluorescence decay of TAMRA in CP29-40. In this case the decay resembles mostly that of the non-transferring apo-4. Global analysis with 2 components reveals a lifetime of 29 ps but its amplitude is only 40%, probably largely due to protein quenching (see Table 2). No rise could be detected in the Chl region suggesting absence of energy transfer although it can not be excluded that singlet-singlet annihilation is masking a small rise. TCSPC data of CP29-40 show four decay components in the TAMRA fluorescence region: 78 ps (37%), 323 ps (22%), 1.35 ns (24%) and 3.48 ns (17%) (see Table 1). No rise could be detected in the Chl region. The anisotropy data reveal two correlations times of 797 ps (amplitude 0.04) and 4.2 ns (amplitude 0.02) and a residual anisotropy of 0.26 (see Table 3). These values are similar to those of CP29-4.

3.4 Discussion

The presented fluorescence kinetics data reveal fast (tens of ps) excitation energy transfer in some cases, possibly some transfer in the hundreds of ps but also some TAMRA molecules that do not or hardly show any energy transfer. In order to interpret the meaning of these observations it is important to apply the Förster equation[44]: $\tau/\tau_F = (R/R_0)^6$, where R_0 is the Förster radius, R is the center-to center distance between donor and acceptor, τ equals the inverse of the energy transfer rate from a donor molecule (TAMRA) to an acceptor molecule (Chl *a*) and τ_F is the fluorescence lifetime of the donor (3.2 ns in methanol, see Table 1) and was measured in the solvent that was used for calculating the fluorescence quantum yield. The latter is needed for the calculation of the Förster radius, which is defined as:

$$R_0 = 0.211 * \left[\kappa^2 * n^{-4} * Q_D * J(\lambda)\right]^{1/6}$$

where κ is the orientation factor, n the refractive index (its exact meaning in this equation is extensively discussed in ref. 45), Q_D is the quantum yield of the donor in absence of acceptor, and J(λ) is the overlap integral of the fluorescence emission spectrum of the donor and the absorption spectrum of the acceptor. R_0 was calculated with κ^2=2/3, n=1.4 (a value typical for a dye, between n≈1.33 of buffer and n≈1.5 of proteins[46]), Q_D=0.66 (MTS-TAMRA measured in methanol, using as a reference TAMRA (Invitrogen) in methanol, with a reported value of Q_D=0.68). J(λ) was calculated from the absorption spectrum of Chl *a* in a protein environment[47] (scaling extinction coefficient of the red-most peak to 8630 $m^2\,mol^{-1}$ [48]) and the emission spectrum of TAMRA in DM buffer. The absorption spectrum of Chl *a* was used, instead of Chl *b,* for the following reasons: Chl *a* is probably closer to TAMRA than Chl *b* (see Figure 1), CP29 contains 3 times more Chl *a* than Chl *b*, and the spectra of Chl *a* and *b* are very similar in the region of TAMRA emission. This leads to a value of R_0 = 5.0 nm. The rate of transfer is very sensitive to the distance between the chromophores and for instance a transfer time of 10 ps corresponds to a distance of 1.9 nm whereas a time of 300 ps corresponds to 3.4 nm. It should be kept in mind that in the case of CP29 there are several potential acceptors available and the observed transfer rate is simply the sum of the individual transfer rates to the various Chls. Note that an uncertainty in the transfer rate of 5% (see Results) leads to an uncertainty in the distance R which is smaller than 1% because the transfer rate is proportional to R^{-6}.

In the case of CP29-4, a large fraction of the excitations (around 80%) is transferred to the Chls with a rate of $(20\ ps)^{-1}$, indicating that the distance to one or more of the Chls is of the order of 2 nm. If the secondary structure of the N-terminus would be an α-helix, the distance from amino acid 4 and 105 (which is near the beginning of the Chl-containing part of the protein) would be around 15 nm (with a calculated transfer time of

~2 μs). Therefore, it is immediately clear that in approximately 80% of the complexes, the end of the N-terminal loop is folded back to the hydrophobic part of the protein. It is however unclear as to why in the remaining 20% of the cases no energy transfer is observed. One straightforward explanation is that in these cases the loop is not folded back. However, the observed kinetics for CP29-97 is nearly identical to that of CP29-4 and in that case it is more difficult to imagine how TAMRA bound to residue 97, which is close to the transmembrane region, can be far away from the Chls. The latter observations suggest that detailed structural modeling would be needed to investigate this possibility. Whatever the exact reason may be, it is clear that TAMRA is in a rather rigid environment when it is not transferring its excitations in CP29-4 and CP29-97 as can be concluded from the slow anisotropy correlation times and the large value of the residual anisotropy. The energy transfer from TAMRA bound at position 40 is clearly less efficient than that from the other reconstituted samples, leading to the conclusion that residue 40 is farther away from the Chls. Position 40 is close to the region which, based on the primary structure, was suggested to bind one of the central carotenoids[5], indicating its proximity to the transmembrane domain. However, this region later turned out not to be involved in carotenoid binding[7], which is in agreement with the reduced amount of energy transfer from the label at position 40 to Chl.

In conclusion, it turned out to be possible to attach a chromophore with high efficiency at a specific position in the N-terminal domain of CP29 and to measure the ultrafast energy transfer from this label to the Chls. This opens up the possibility to probe the entire N-terminal loop and determine distances and heterogeneity and also local mobility/flexibility when the energy transfer is not very efficient. These first measurements indicate qualitatively that the end of the N-terminus is folded back on the hydrophobic part of the protein but they also show that there is some structural heterogeneity. Further experiments and data analysis combined with structural calculations are in progress, and may yield more quantitative results.

Acknowledgements

This work is part of the research program of the ‘‘Stichting voor Fundamenteel Onderzoek der Materie (FOM)’’, which is financially supported by the ‘‘Nederlandse Organisatie voor Wetenschappelijk Onderzoek (NWO)’’. B.v.O. was supported by FOM. RC acknowledges support (visitor grant) from the “Nederlandse Organisatie voor Wetenschappelijk Onderzoek (NWO)”. SM gratefully acknowledges the graduate school Experimental Plant Sciences for financial support.

References

1. Boekema, E. J., van Roon, H., van Breemen, J. F. L. and Dekker, J. P. (1999), *Eur. J. Biochem.* **266**, 444-452.
2. Ahn, T. K., Avenson, T. J., Ballottari, M., Cheng, Y.-C., Niyogi, K. K., Bassi, R. and Fleming, G. R. (2008), *Science* **320**, 794-797.
3. Avenson, T. J., Ahn, T. K., Zigmantas, D., Niyogi, K. K., Li, Z., Ballottari, M., Bassi, R. and Fleming, G. R. (2008), *J. Biol. Chem.* **283**, 3550-3558.
4. Mozzo, M., Passarini, F., Bassi, R., van Amerongen, H. and Croce, R. (2008), *Biochim. Biophys. Acta* **in press (doi: 10.1016/j.bbabio.2008.04.036)**.
5. Bassi, R., Croce, R., Cugini, D. and Sandona, D. (1999), *Proc. Natl. Acad. Sci. U. S. A.* **96**, 10056-10061.
6. Caffarri, S., Passarini, F., Bassi, R. and Croce, R. (2007), *FEBS Lett.* **581**, 4704-4710.
7. Gastaldelli, M., Canino, G., Croce, R. and Bassi, R. (2003), *J. Biol. Chem.* **278**, 19190-19198.
8. Simonetto, R., Crimi, M., Sandona, D., Croce, R., Cinque, G., Breton, J. and Bassi, R. (1999), *Biochemistry* **38**, 12974-12983.
9. Leupold, D., Teuchner, K., Ehlert, J., Irrgang, K.-D., Renger, G. and Lokstein, H. (2006), *J. Biol. Chem.* **281**, 25381-25387.
10. Pascal, A., Gradinaru, C., Wacker, U., Peterman, E., Calkoen, F., Irrgang, K.-D., Horton, P., Renger, G., van Grondelle, R., Robert, B. and van Amerongen, H. (1999), *Eur. J. Biochem.* **262**, 817-823.
11. Pieper, J., Irrgang, K. D., Ratsep, M., Voigt, J., Renger, G. and Small, G. J. (2000), *Photochem. Photobiol.* **71**, 574-581.
12. Ratsep, M., Pieper, J., Irrgang, K. D. and Freiberg, A. (2008), *J. Phys. Chem. B* **112**, 110-118.
13. Cinque, G., Croce, R., Holzwarth, A. and Bassi, R. (2000), *Biophys. J.* **79**, 1706-1717.
14. Croce, R., Müller, M. G., Bassi, R. and Holzwarth, A. R. (2003), *Biophys. J.* **84**, 2508-2516.
15. Croce, R., Müller, M. G., Caffarri, S., Bassi, R. and Holzwarth, A. R. (2003), *Biophys. J.* **84**, 2517-2532.
16. Gradinaru, C. C., Pascal, A. A., van Mourik, F., Robert, B., Horton, P., van Grondelle, R. and van Amerongen, H. (1998), *Biochemistry* **37**, 1143-1149.
17. Gradinaru, C. C., van Stokkum, I. H. M., Pascal, A. A., van Grondelle, R. and van Amerongen, H. (2000), *J. Phys. Chem. B* **104**, 9330-9342.
18. Salverda, J. M., Vengris, M., Krueger, B. P., Scholes, G. D., Czarnoleski, A. R., Novoderezhkin, V. I., van Amerongen, H. and van Grondelle, R. (2003), *Biophys. J.* **84**, 450-465.
19. Testi, M. G., Croce, R., Polverino-De Laureto, P. and Bassi, R. (1996), *FEBS Lett.* **399**, 245-250.
20. Bergantino, E., Sandonà, D., Cugini, D. and Bassi, R. (1998), *Plant Mol. Biol.* **36**, 11-22.
21. Mauro, S., Dainese, P., Lannoye, R. and Bassi, R. (1997), *Plant Physiol.* **115**, 171-180.
22. Croce, R., Breton, J. and Bassi, R. (1996), *Biochemistry* **35**, 11142-11148.
23. Hansson, M. and Vener, A. V. (2003), *Mol. Cell. Proteomics* **2**, 550-559.
24. Liu, Z. F., Yan, H., Wang, K., Kuang, T., Zhang, J., Gui, L. and Chang, W. (2004), *Nature* **428**, 287-292.
25. Standfuss, J., Terwisscha van Scheltinga, A. C., Lamborghini, M. and Kühlbrandt, W. (2005), *EMBO J.* **24**, 919-928.
26. Horn, R. and Paulsen, H. (2004), *J. Biol. Chem.* **279**, 44400-44406.
27. Nagai, K. and Thøgersen, H. C. (1987), *Methods Enzymol.* **153**, 461-481.
28. Paulsen, H., Rümler, U. and Rüdiger, W. (1990), *Planta* **181**, 204-211.
29. Porra, R. J., Thompson, W. A. and Kriedemann, P. E. (1989), *Biochim. Biophys. Acta* **975**, 384-394.

30. Davies, B. H. 1965. Analysis of carotenoid pigments. In Chemistry and biochemistry of plant pigments, editor Goodwin, T. W., Academic Press, New York. p. 489-532.
31. Spruijt, R. B., Meijer, A. B., Wolfs, C. J. A. M. and Hemminga, M. A. (2000), *Biochim. Biophys. Acta* **1509**, 311-323.
32. van Stokkum, I. H. M., van Oort, B., van Mourik, F., Gobets, B. and van Amerongen, H. 2008. (Sub)-Picosecond Spectral Evolution of Fluorescence Studied with a Synchroscan Streak-Camera System and Target Analysis. In Biophysical Techniques in Photosynthesis, Volume II, editors: Aartsma, T. J. and Matysik, J., Springer, Dordrecht. p. 223-240.
33. van Stokkum, I. H. M., Larsen, D. S. and van Grondelle, R. (2004), *Biochim. Biophys. Acta* **1657**, 82-104.
34. Borst, J. W., Hink, M. A., van Hoek, A. and Visser, A. J. W. G. (2005), *J. Fluoresc.* **15**, 153-160.
35. van Hoek, A. and Visser, A. J. W. G. (1985), *Anal. Instrum.* **14**, 359-378.
36. Lin, H.-J., Szmacinski, H. and Lakowicz, J. R. (1999), *Anal. Biochem.* **269**, 162-167.
37. van Oort, B., Amunts, A., Borst, J. W., van Hoek, A., Nelson, N., van Amerongen, H. and Croce, R. (2008), *Biophys. J.* **in press**.
38. van Hoek, A., Vos, K. and Visser, A. J. W. G. (1987), *IEEE J. Quantum Electron.* **QE-23**, 1812-1820.
39. Digris, A. V., Skakoun, V. V., Novikov, E. G., van Hoek, A., Claiborne, A. and Visser, A. J. W. G. (1999), *Eur. Biophys. J.* **28**, 526-531.
40. Visser, N. V., Westphal, W. G., van Hoek, A., van Mierlo, C. P. M., Visser, A. J. W. G. and van Amerongen, H. (2008), *Biophys. J.* **95**, 2462-2469.
41. Cha, A. and Bezanilla, F. (1998), *J. Gen. Physiol.* **112**, 391-408.
42. Marmé, N., Knemeyer, J. P., Sauer, M. and Wolfrum, J. (2003), *Bioconjug. Chem.* **14**, 1133-1139.
43. Barzda, V., Gulbinas, V., Kananavicius, R., Cervinskas, V., van Amerongen, H., van Grondelle, R. and Valkunas, L. (2001), *Biophys. J.* **80**, 2409-2421.
44. Förster, T. (1949), *Zeitschrift für Naturforschung* **4a**, 321-327.
45. Knox, R. S. and van Amerongen, H. (2002), *J. Phys. Chem. B* **106**, 5289-5293.
46. Lakowicz, J. R. 1999. Principles of Fluorescence Spectroscopy. Kluwer Academic/Plenum Publishers, New York.
47. Croce, R., Cinque, G., Holzwarth, A. R. and Bassi, R. (2000), *Photosynth. Res.* **64**, 221-231.
48. Strain, H. H., Thomas, M. R. and Katz, J. J. (1963), *Biochim. Biophys. Acta* **75**, 306-311.

Chapter 4

Aggregation of Light-Harvesting Complex II leads to formation of efficient excitation energy traps in monomeric and trimeric complexes

based on:
B. van Oort, A. van Hoek, A.V. Ruban, and H. van Amerongen, 2007. Aggregation of Light-Harvesting Complex II leads to formation of efficient excitation energy traps in monomeric and trimeric complexes. FEBS Letters, 581, p. 3528-3532

Abstract

Nonphotochemical quenching (NPQ) protects plants against photodamage by converting excess excitation energy into harmless heat. *In vitro* aggregation of the major Light-Harvesting Complex (LHCII) induces similar quenching, the molecular mechanism of which is frequently considered to be the same. However, a very basic question regarding the aggregation-induced quenching has not been answered yet. Are excitation traps created upon aggregation, or do existing traps start quenching excitations more efficiently in aggregated LHCII where trimers are energetically coupled? Time-resolved fluorescence experiments presented here demonstrate that aggregation creates traps in a significant number of LHCII trimers, which subsequently also quench excitations in connected LHCIIs.

4.1 Introduction

During photosynthesis solar energy is captured by pigments and stored by a series of events that convert the pure energy of light into biochemical energy. Primary reactions of this process take place in photosynthetic systems in the thylakoid membrane. These systems are highly organized: reaction centres (RCs) are surrounded by antennae that transfer absorbed light energy to the RCs. The antenna system consists of various pigment-binding proteins. In higher plants the main antenna complex is Light-Harvesting Complex II (LHCII), binding chlorophyll (Chl) a, Chl b, and xanthophylls.

Too much light can be damaging, and higher plants respond to conditions where the absorbed light exceeds the photosynthetic capacity via several photoprotective mechanisms. One of the most significant of them is the ΔpH-induced enhancement of non-radiative energy dissipation in the photosystem II antenna, registered as nonphotochemical chlorophyll fluorescence quenching (NPQ)[1]. This process causes a decrease of the singlet excited-state lifetime (quenching) of chlorophyll a (Chl a) by turning excess excitation energy into heat[2].

NPQ is mainly triggered by a ΔpH across the photosynthetic membrane and the dynamic control is achieved by the regulatory role of the xanthophyll-cycle carotenoids (violaxanthin, antheraxanthin and zeaxanthin) and the PsbS protein[3,4]. It is known that random aggregation of isolated LHCII leads to fluorescence quenching that resembles NPQ[5,6] and therefore aggregated LHCII seems to be a good model system for studying NPQ, although this does not necessarily mean that similar aggregates are also present in thylakoid membranes. A substantial amount of recent work has focused on NPQ-associated events in LHCII[7-12]. However, no consensus has been reached about the physical nature of

the energy dissipation. Moreover, it is still unknown whether LHCII aggregation leads to the formation of quenchers, as proposed in for instance[13,14] or that increased connectivity between trimers upon aggregation leads to efficient quenching by a small population of permanently quenched trimers[15,16]. In the latter case excitations would be transferred from unquenched trimers to quenched trimers, leading to accelerated depopulation of the excited state. These two scenarios have been visualized schematically in Figure 1. To discriminate between them we studied the excited-state lifetimes of LHCII of spinach in different states of aggregation: monomers, trimers and aggregates. We demonstrate that excitation traps are indeed being created upon aggregation of trimeric LHCII. These traps do not only quench excitations in the trimer in which they are located, due to excitation energy transfer between trimers, these traps also quench excitations originating in complexes that do not contain traps themselves. The fluorescence quenching in monomers was found to be even stronger than that in trimers, suggesting an intramonomeric origin of this process.

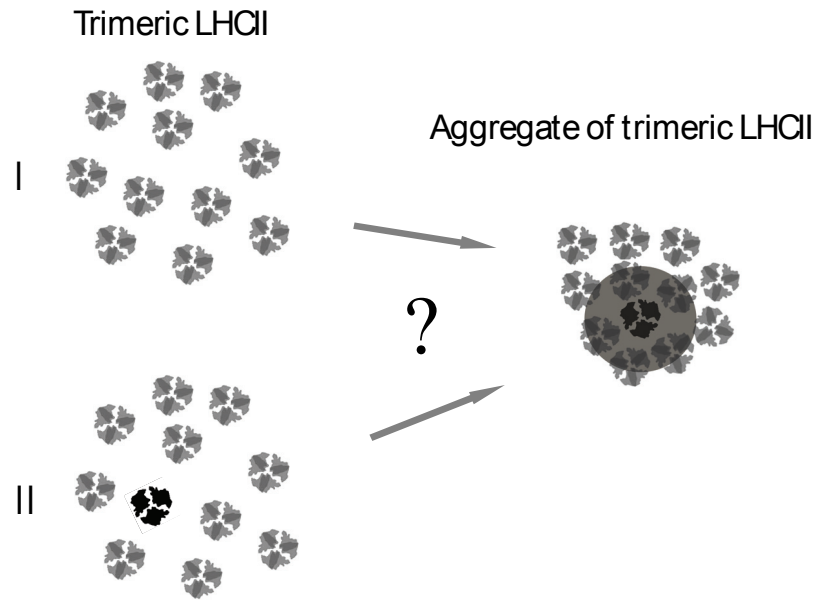

Figure 1. *Two scenarios of aggregation-induced fluorescence quenching of LHCII: (I) quencher formation upon aggregation, and (II) existing quenchers start quenching excitations originating in LHCII without quenchers, due to efficient transfer between trimers in aggregates. LHCII trimers with and without quenchers (black and light grey images, respectively) and LHCII trimers that are affected by the quencher (grey circular semitransparent area) are shown.*

4.2 Materials and Methods

Trimeric and monomeric LHCII were prepared from spinach as described before[17]. The proteins were suspended in a 20 mM HEPES buffer (pH 7.6) in 0.03% (0.6 mM) β-dodecylmaltoside (β-DM). Aggregates were obtained by lowering the β-DM concentration to 0.0003% (0.6 μM), i.e. far below the critical micelle concentration (~0.15 mM).

Steady-state absorption spectra were recorded on a Varian Cary 5E spectrophotometer. Steady-state fluorescence emission spectra (430 nm excitation) were recorded on a Spex-Fluorolog 3.2.2 spectrofluorimeter (Jobin-Yvon). Time-correlated single photon counting was performed with a home-built setup, as described elsewhere[18]. In brief, samples were excited with vertically polarized 430 nm pulses of 0.2 ps duration at a repetition rate of 3.8 MHz. The excitation density was reduced to obtain a count-rate below 30,000 per second (sub-pJ pulse energy) and care was taken to minimize data distortion[19]. The instrument response function (~30 ps FWHM) was obtained with pinacyanol iodide in methanol, with 10 ps fluorescence lifetime. Fluorescence was detected at right angle with respect to the excitation beam in 10 measuring sequences of 2 times 10 seconds through a vertical or horizontal polarizer and through a 665 nm long-pass filter (Schott). Detection through band-pass filters at 635 nm, 701 nm and 721 nm gave identical results. Individual photons were detected by a microchannel plate photomultiplier, and arrival times were stored in 4096 channels of a multichannel analyzer. The channel spacing was 5 ps or 1.25 ps (0.6 mM β-DM) and 3.0 ps (6 μM β-DM).

Fluorescence decay curves (parallel + 2 x perpendicular) were fitted to a sum of exponentials, convoluted with the instrument response function[20]. The quality of a fit was judged from the χ^2-value and by visual inspection of the residuals and the autocorrelation thereof. The number of exponentials was considered sufficient if the addition of one extra decay component did not significantly improve the fit. Confidence intervals were calculated by exhaustive search.

4.3 Results and Discussion

Absorption spectra of trimeric and monomeric LHCII are shown in Figure 2. These spectra resemble previous results (e.g. refs. 21-23). The broader absorption bands for monomeric LCHII indicate a more disordered/less rigid (and therefore less unique) environment of the pigments[24]. Upon aggregation the light scattering increases which causes an apparent increase of the absorption. This becomes more pronounced upon going to the blue. The

absorption decreases around 490 nm (absorption of lutein/neoxanthin[25]). The changes in absorption of LHCII upon aggregation have been discussed extensively by Naqvi et al[23].

Trimeric and monomeric LHCII both show multi-exponential fluorescence decay curves (Figure 3). The fitting results are given in Table 1. For trimeric LHCII the decay is nearly mono-exponential (3.81 ns, 86%). A small fraction of the trimers shows a shorter decay time (1.96 ns, 11%), and only a very small fraction decays much faster, i.e. is heavily quenched (0.21 ns, 2%). Similar results were obtained before (e.g. refs. 26,27) although the percentages differ somewhat. For monomeric LHCII similar decay times are observed but the fraction of fast components is higher (38% 1.89 ns and 14% 0.19 ns). Moreover, the fitting results depend slightly on the time interval used for fitting, indicating a broader distribution of decay times than for trimeric LHCII. This is probably related to the increased disorder/reduced rigidity of the monomeric unit, as also reflected by broadening of the absorption spectrum (Figure 2).

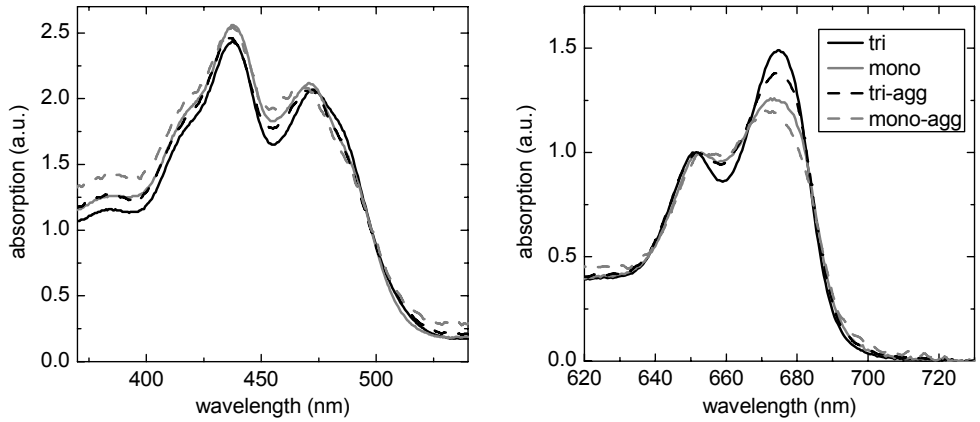

Figure 2. *Absorption spectra of trimeric (black) and monomeric (grey) LHCII, and aggregates (dashed) thereof, in the Soret (left) and Q-band region. Spectra are normalized on the peak around 650 nm.*

Upon aggregation the fluorescence decay becomes considerably faster as can be seen in Figure 4. The results of the fitting of these decay curves depend on the fitted time-range, starting values of the fitted parameters, and number of decay times. In all cases, at least five decay times are needed, as observed before[28]. Two of these are above 1 ns and the corresponding amplitudes are very small. They are possibly due to non-aggregated monomers or trimers. For the discussion below these components are not relevant and for the fitting of the decay curves we assumed these lifetimes to be equal for aggregated monomers and trimers. The fitting results are presented in Table 1. The large heterogeneity of lifetimes is probably due to the fact that the aggregates are random/disordered. More

ordered aggregates of plant light-harvesting complexes show less decay components[29]. This demonstrates clearly that the organization of the aggregates can modulate the lifetime.

The fitted values for the amplitudes and lifetimes can be used to calculate the relative fluorescence quantum yield of monomers, trimers and aggregates (Table 2). These yields are rather precise, do not depend significantly on the variation in the fitting values, and are very close to the relative quantum yields obtained from the steady-state measurements. The latter observation means that there is no indication for the presence of components that are even faster than the shortest fitted decay components.

The two >1 ns-lifetimes (1.6 ns and 4.0 ns) are very similar to those before aggregation, and they have very small amplitudes (<3%). The remaining lifetimes are much faster, reflecting severe quenching. The dominating lifetimes are of the order of 100-200 ps and several tens of ps. The 100-200 ps is similar to that of the small fraction observed for trimers and monomers in "unaggregated" LHCII, suggesting that in those preparations a small fraction of aggregates or quenched monomers/trimers is present.

In our analysis we initially focus on the results for aggregated trimers. The two main decay components are 25-40 ps (30-36%) and 150-200 ps (40-45%). How can these decay rates be related to quenching processes in the aggregate? Singlet excitations can

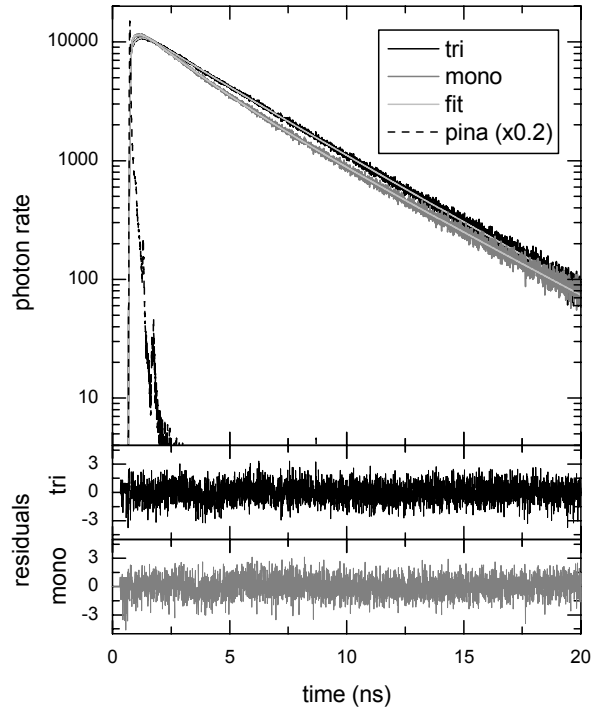

Figure 3. *Fluorescence decay curves of trimeric (black) and monomeric (grey) LHCII and of pinacyanol iodide in methanol (dashed). Excitation was at 430 nm, detection at >665 nm, 5.0 ps/time-channel.*

move from one Chl to another. This can be described as a diffusion process that leads to excitation equilibration[30]. Singlet-singlet annihilation studies showed that the excitation equilibration time in trimers is 30-50 ps and that for an aggregate of N trimers it is roughly equal to N * 30 ps[30]. From these numbers it can be predicted what the effect of quenchers will be on the fluorescence decay times.

For the sake of argument it is first assumed that the quenchers are extremely efficient (quenching rate >1 ps-1). In this case the fluorescence lifetime equals the time it takes for an excitation to reach the quencher, after which it is immediately quenched. Thus one would expect a lifetime of 30-50 ps (the excitation equilibration time) for quenched trimeric LHCII. A similar lifetime (25 ps) is for instance observed for a large fraction of LHCII trimers under high hydrostatic pressure[31]). In aggregates, the presence of one efficient quencher per 4 trimers would thus lead to a diffusion-limited lifetime of 120-200 ps. The largest part of the fluorescence decay for aggregates (of trimers) is described by lifetimes of 33 ps (34%) and 150 ps (43%). This demonstrates the presence of a high concentration of quenchers: 33 ps corresponds to 1 quencher per trimer, 150 ps corresponds to 1 quencher per ~4 trimers These results are in sharp contrast to the case of isolated trimers where only 2% of the complexes show a 210 ps decay component, i.e. 1 out of at least 50 trimers is significantly quenched. These results unequivocally demonstrate the fact that a large amount of quenchers is created upon aggregation. In the case of less efficient quenchers the number of quenchers needs to be even higher to explain the short lifetimes.

Table 1. *Fitted decay times (τ) and relative amplitudes (p) of trimeric and monomeric LHCII and aggregates thereof, with 95% confidence intervals in square brackets.*

	unaggregated		aggregated	
	τ (ns)	p	τ (ns)	p
trimer	**0.21** [0.088-0.406]	**0.02** [0.016-0.036]	**0.033** [0.025-0.039]	**0.34** [0.301-0.361]
	1.96 [1.856-2.074]	**0.11** [0.108-0.120]	**0.18** [0.156-0.195]	**0.43** [0.402-0.453]
	3.81 [3.805-3.820]	**0.86** [0.858-0.863]	**0.51** [0.459-0.558]	**0.20** [0.178-0.241]
			1.62 [1.409-1.803]	**0.028** [0.024-0.035]
			3.96 [3.413-4.895]	**0.002** [0.001-0.004]
monomer	**0.19** [0.139-0.238]	**0.14** [0.123-0.167]	**0.039** [0.036-0.042]	**0.62** [0.588-0.645]
	1.89 [1.775-1.970]	**0.38** [0.365-0.403]	**0.15** [0.135-0.161]	**0.31** [0.288-0.345]
	4.02 [3.962-4.068]	**0.47** [0.452-0.499]	**0.50** [0.451-0.533]	**0.06** [0.052-0.072]
			1.62 [1.409-1.803]	**0.007** [0.006-0.008]
			3.96 [3.413-4.895]	**0.001** [0.001-0.002]

The three <1 ns decay components probably reflect a broad distribution of lifetimes originating from heterogeneity of the quencher concentration in the aggregates. In such case it is better to consider the amplitude-weighted average fluorescence lifetime (<τ>). The >1 ns components probably originate from non-aggregated LHCII, so the relevant parameter is in fact not <τ>, but <τ>*: the average lifetime calculated from only the <1 ns components. For aggregates of trimeric LHCII <τ>* = 191 ps (Table 2), reflecting the presence of at least one quencher per 5 trimers.

Also upon aggregation of monomers substantial quenching is observed and the amplitude of the fastest components is even higher than for trimers. This is in agreement with other experiments that showed that monomeric LHCII is more easily quenched than trimeric LHCII (e.g. refs. 32,33). This can be relevant for NPQ, because excess light can lead to monomerization of LHCII in thylakoid membranes[34]. The fluorescence lifetimes of aggregated monomers strongly resemble those of aggregated trimers. This points at domains with the same concentration of quenchers in both types of aggregates, however in different amounts (Table 1). Again it should be concluded that quenchers are created upon (random) aggregation.

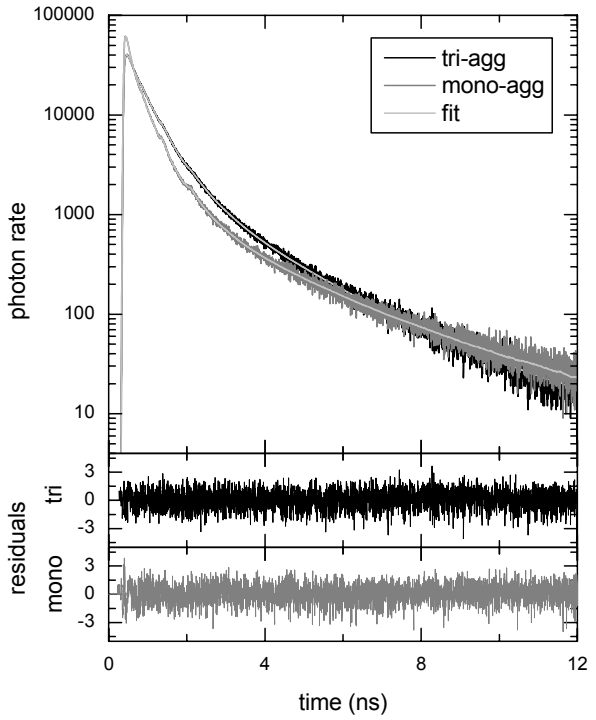

Figure 4. *Fluorescence decay curves of aggregates of trimeric (black) and monomeric (grey) LHCII. Excitation was at 430 nm, detection at >665 nm, 3.0 ps/time-channel.*

In conclusion, we find that only a very small fraction of trimeric LHCII is in a quenched state. This fraction increases substantially upon aggregation. These quenchers can then also trap excitations that arise in trimers that do not contain quenchers themselves. Aggregates of monomeric LHCII contain even a larger fraction of quenchers in comparison to the trimer. This fraction further increases upon aggregation, even more than for trimeric LHCII.

From the present data we cannot conclude what the nature is of the created quencher. It was argued before that structural changes of LHCII upon aggregation lead to quenching similar to NPQ *in vivo*[5]. It was for instance shown that aggregation leads to a change in interaction between Lutein 1 and Chl *a*[35] and it was speculated that this might lead to a change of the excited-state lifetime[36]. However, it remains uncertain whether such a mechanism is also present here.

Table 2. *Fluorescence quantum yields (φ_f^{rel}) and average lifetime ($<\tau>^*$) of trimeric and monomeric LHCII and aggregates thereof.*

	unaggregated		aggregated	
	trimer	monomer	trimer	monomer
φ_f^{rel} (st.st.) [1,2]	1	0.68	0.05	0.02
φ_f^{rel} (time-res.) [2,3]	1	0.75	0.07	0.03
$<\tau>^*$ (ns) [4]	-	-	0.191	0.101

[1] from steady state data; [2] relative to unaggregated trimeric LHCII; [3] from time-resolved fluorescence; [4] calculated without >1 ns lifetimes

Acknowledgements

This work is part of the research program of the "Stichting voor Fundamenteel onderzoek der Materie (FOM)", which is financially supported by the "Nederlandse Organisatie voor Wetenschappelijk Onderzoek (NWO)". B.v.O. was supported by FOM. A.V.R. was supported by the UK BBSRC.

References

1. Horton, P., Ruban, A. V. and Walters, R. G. (1996), *Ann. Rev. Pl. Physiol. Pl. Mol. Biol.* **47**, 655-684.
2. Horton, P. and Ruban, A. V. (2005), *J. Exp. Bot.* **56**, 365-373.
3. Demmig-Adams, B. (1990), *Biochim. Biophys. Acta* **1020**, 1-24.
4. Niyogi, K. K. (1999), *Ann. Rev. Pl. Physiol. Pl. Mol. Biol.* **50**, 333-359.
5. Ruban, A. V. and Horton, P. (1999), *Plant Physiol.* **119**, 531-542.
6. Ruban, A. V., Young, A. and Horton, P. (1994), *Biochim. Biophys. Acta* **1186**, 123-127.
7. Holt, N. E., Zigmantas, D., Valkunas, L., Li, X.-P., Niyogi, K. K. and Fleming, G. R. (2005), *Science* **307**, 433-436.
8. Horton, P., Ruban, A. V. and Wentworth, M. (2000), *Philos. Trans. R. Soc. London, B* **355**, 1361-1370.
9. Li, X.-P., Gilmore, A. M., Caffarri, S., Bassi, R., Golan, T., Kramer, D. and Niyogi, K. K. (2004), *J. Biol. Chem.* **279**, 22866-22874.
10. Aspinall-O'Dea, M., Wentworth, M., Pascal, A., Robert, B., Ruban, A. V. and Horton, P. (2002), *Proc. Natl. Acad. Sci. U. S. A.* **99**, 16331-16335.
11. Bassi, R. and Caffarri, S. (2000), *Photosynth. Res.* **64**, 243-256.
12. Pascal, A. A., Liu, Z. F., Broess, K., van Oort, B., van Amerongen, H., Wang, C., Horton, P., Robert, B., Chang, W. R. and Ruban, A. (2005), *Nature* **436**, 134-137.
13. Horton, P., Wentworth, M. and Ruban, A. V. (2005), *FEBS Lett.* **579**, 4201-4206.
14. Ruban, A. V., Young, A. and Horton, P. (1994), *Biochim. Biophys. Acta* **1186**, 123-127.
15. den Hollander, W. T. F., Bakker, J. G. C. and van Grondelle, R. (1983), *Biochim. Biophys. Acta* **725**, 492-507.
16. Gillbro, T., Sandström, Å., Spangfort, M., Sundström, V. and van Grondelle, R. (1988), *Biochim. Biophys. Acta* **934**, 369-374.
17. Ruban, A. V., Lee, P. J., Wentworth, M., Young, A. J. and Horton, P. (1999), *J. Biol. Chem.* **274**, 10458-10465.
18. Borst, J. W., Hink, M. A., van Hoek, A. and Visser, A. J. W. G. (2005), *Journal of Fluorescence* **15**, 153-160.
19. van Hoek, A. and Visser, A. J. W. G. (1985), *Anal. Instrum.* **14**, 359-378.
20. Digris, A. V., Skakoun, V. V., Novikov, E. G., van Hoek, A., Claiborne, A. and Visser, A. J. W. G. (1999), *Eur. Bioph. J.* **28**, 526-531.
21. Nussberger, S., Dekker, J. P., Kühlbrandt, W., van Bolhuis, B. M., van Grondelle, R. and van Amerongen, H. (1994), *Biochemistry* **33**, 14775-14783.
22. Peterman, E. J. G., Gradinaru, C. C., Calkoen, F., Borst, J. C., van Grondelle, R. and van Amerongen, H. (1997), *Biochemistry* **36**, 12208-12215.
23. Naqvi, K. R., Melo, T. B., Raju, B. B., Javorfi, T. and Garab, G. (1997), *Spectrochim. Acta, Part A* **53**, 1925-1936.
24. Palacios, M. A., Frese, R. N., Gradinaru, C. C., van Stokkum, I. H. M., Premvardhan, L. L., Horton, P., Ruban, A. V., van Grondelle, R. and van Amerongen, H. (2003), *Biochim. Biophys. Acta* **1605**, 83.
25. Croce, R., Cinque, G., Holzwarth, A. R. and Bassi, R. (2000), *Photosynth. Res.* **64**, 221-231.
26. Moya, I., Silvestri, M., Vallon, O., Cinque, G. and Bassi, R. (2001), *Biochemistry* **40**, 12552-12561.
27. Palacios, M. A., de Weerd, F. L., Ihalainen, J. A., van Grondelle, R. and van Amerongen, H. (2002), *J. Phys. Chem. B* **106**, 5782-5787.
28. Barzda, V., de Grauw, C. J., Vroom, J., Kleima, F. J., van Grondelle, R., van Amerongen, H. and Gerritsen, H. C. (2001), *Biophys. J.* **81**, 538-546.
29. Lambrev, P. H., Varkonyi, Z., Krumova, S., Kóvacs, L., Miloslavina, Y., Holzwarth, A. R. and Garab, G. (2007), *Biochim. Biophys. Acta* **1767**, 847-853.

30. Barzda, V., Gulbinas, V., Kananavicius, R., Cervinskas, V., van Amerongen, H., van Grondelle, R. and Valkunas, L. (2001), *Biophys. J.* **80**, 2409-2421.
31. van Oort, B., van Hoek, A., Ruban, A. V. and van Amerongen, H. (2007), *J. Phys. Chem. B* **111**, 7631-7637.
32. Wentworth, M., Ruban, A. V. and Horton, P. (2000), *FEBS Lett.* **471**, 71-74.
33. Wentworth, M., Ruban, A. V. and Horton, P. (2004), *Biochemistry* **43**, 501-509.
34. Garab, G., Cseh, Z., Kovacs, L., Rajagopal, S., Varkonyi, Z., Wentworth, M., Mustardy, L., Der, A., Ruban, A. V., Papp, E., Holzenburg, A. and Horton, P. (2002), *Biochemistry* **41**, 15121-15129.
35. Lampoura, S. S., Barzda, V., Owen, G. M., Hoff, A. J. and van Amerongen, H. (2002), *Biochemistry* **41**, 9139-9144.
36. van Amerongen, H. and van Grondelle, R. (2001), *J. Phys. Chem. B* **105**, 604-617.

Chapter 5

The equilibrium between quenched and non-quenched conformations of the major plant light-harvesting complex studied with high-pressure time-resolved fluorescence

based on:
B. van Oort, A. van Hoek, A.V. Ruban, and H. van Amerongen, 2007. The equilibrium between quenched and non-quenched conformations of the major plant light-harvesting complex studied with high-pressure time-resolved fluorescence. Journal of Physical Chemistry B, 111, p. 7631-7637

Abstract

Nonphotochemical quenching (NPQ) of chlorophyll fluorescence plays an important role in the protection of plants against excessive light. Fluorescence quenching of the major light-harvesting complex (LHCII) provides a model system to study the mechanism of NPQ. The existence of both quenched and non-quenched states of LHCII have been postulated. We used time-resolved fluorescence and hydrostatic pressure to study differences between these states. Pressure shifts the thermodynamic equilibrium between the two states. The estimated volume difference was 5 ml/mol, indicating a local conformational switch. The estimated free energy difference was 7.0 kJ/mol: high enough to keep the quenched state population low under normal conditions, but low enough to switch in a controlled way. These properties are physiologically relevant properties, because they guarantee efficient light harvesting, while at the same time maintaining the capacity to switch to a quenched state. These results indicate that conformational changes of LHCII can play an important role in NPQ.

5.1 Introduction

Photosynthesis provides a large input into the global food chain by converting solar energy into chemical energy. Primary reactions of this process take place in the thylakoid membrane, where a number of protein complexes are organised to conduct the photon energy conversion into the energy of ATP and NADPH. The photosynthetic systems are organised as supercomplexes: reaction centres are surrounded by antennae. The antennae consist of several pigment-protein complexes containing large amounts of photochemically inactive pigments, which greatly enhance the effective reaction center absorption cross-section. This enables plant growth at very low light intensity. However, the light intensity can fluctuate greatly during a day (up to hundreds of times). Too much light can be damaging, particularly for photosystem II, which carries one of the greatest oxidizers in nature, reaction center P680, capable of removing electrons from water, using it as fuel for driving the photosynthetic electron transport[1]. In order to avoid potentially lethal damage to the membrane by the "great oxidizer" a mechanism of NPQ is employed[2]. NPQ responds to frequent variations in light intensity, working as a safety valve to reduce the excitation pressure in the photosystem II.

NPQ is a well-controlled and heterogeneous process. It consists of qE and qI. qE is rapidly reversible in the dark, and is triggered by an increase in the ΔpH across the photosynthetic membrane. qI has slower recovery kinetics, and can appear as photoinhibition, which may actually be due to a photoprotective mechanism[3]. Three known major factors, ΔpH across the photosynthetic membrane, the xanthophyll cycle carotenoid,

zeaxanthin, and PSII protein, PsbS, determine the magnitude and kinetic properties of NPQ[3,4]. Despite a long history of NPQ research, neither the molecular mechanism nor its control is well understood. It is currently one of the major topics in the increasingly multidisciplinary field of photosynthesis research[5]. Two of the key mechanistic questions regarding qE are: *how is the transition into the photoprotective mode occuring* and *what is the physical nature of the energy dissipation process – the quencher's identity*? Protonation of LHCII proteins is currently considered as a major qE event, triggering a conformational transition in antenna into a dissipative, photoprotective state[6]. The NPQ-associated events in LHCII antenna have been in the focus of a number of important recent studies[7-12]. Most of them agree that a conformational change within the LHCII system is behind the *mechanics* of the process. It has been suggested that qE is the result of a protonation-induced conformational change in the LHCII antenna associated with the promotion of protein-protein association leading to aggregation (for a recent review see ref. 6). Isolated LHCII has been found to dissipate excitation energy very efficiently, reproducing closely the main qE features[13,14]. The extent of this aggregation was found to be controlled by the xanthophyll cycle carotenoids in such a manner, that whilst violaxanthin inhibits aggregation, zeaxanthin promotes it, causing amplification in energy quenching[13,14]. These observations led to the further development of an allosteric model for NPQ, where protonation-triggered LHCII aggregation caused changes in chlorophyll-chlorophyll or chlorophyll-carotenoid interactions in the antenna leading to the formation of energy dissipating pairs of pigments[6].

Recently we have obtained the first direct evidence that the conformational state of the LHCII trimer tunes its biological function, by altering the configuration of bound pigments[15]. The structural model of this complex, as determined by X-ray crystallography[16], was found to be that of the photoprotective or dissipative antenna state because of the 5 times reduced chlorophyll excited state/fluorescence lifetime. Because of a particular order of trimers in the crystal, the likelihood of formation of abnormal pigment interactions leading to the quenched state, as was frequently argued[17], was excluded. A group of long-wavelength low-temperature fluorescence bands and specific Raman features arising from the neoxanthin-Chl *b* domain were detected in crystals; these were similar to those reported earlier for quenched LHCII aggregates, but with greatly enhanced spectral resolution arising because of the high uniformity of protein conformation in the crystal.

The fluorescence decay of various LHCII preparations was often found to be bi-exponential, with the major part of the decay in ~4 ns, and a small fraction decaying with 0.3-2 ns[18-20]. These two lifetimes are likely to arise from LHCII in different conformations[18,19] supporting the idea of the existence of a conformational switch. In this work we use high hydrostatic pressure to shift the thermodynamic equilibrium in order to estimate volume and free energy differences between the two postulated states.

We show that a conformational switch of LHCII does exist and leads to the quenching. We provide the thermodynamic analysis of this transition. The quenched state is present to a small extent in isolated LHCII (few percent), and becomes more populated under high hydrostatic pressure. The switch is associated with a small volume difference, indicating a local switch. The associated energy difference is high enough to keep the population of the quenched state low under standard conditions, but the difference is low enough to easily populate it under favouring conditions.

5.2 Materials and Methods

5.2.1 Sample preparation

Trimeric LHCII was isolated from maize plants (*Zea mays* L. cv. LG11) of approximately two weeks old, using the method of Caffari et al.[21]. Samples were stored at -70 °C in 0.5 M sucrose, and measured within 6 months after isolation. For all experiments the samples were diluted at least 100-fold in sucrose-free medium (0.06% β-DM (Inalco S.p.A., Milan, Italy), 10 mM Hepes (Sigma, MO, USA), which is a pressure independent pH buffer[22], pH 7.5, to an OD of less than 0.05 at 435 nm. As a reference experiment the concentrated sample was diluted in 5% Triton X-100 (Pharmacia, Uppsala, Sweden). This leads to complete uncoupling of pigments (see results, and e.g. ref. 23). This sample is named "uncoupled LHCII". All buffers were prepared with ultrapure water (MilliQ gradient A10, Millipor, MA, USA). The Chl a/b ratio was 1.33, the Chl/Xan ratio was 4.1, as determined by deconvolution of the absorption spectra of the 80% acetone extract with the spectra of the individual pigments[24] (a refinement of the method of Porra et al.[25]).

5.2.2 High-pressure fluorescence measurements

Steady-state fluorescence spectra were recorded on a Spex-Fluorolog 3.2.2 spectrofluorimeter (Jobin-Yvon Horiba). For emission spectra, excitation was at 435 nm. For excitation spectra, detection was at 681 nm with trimeric LHCII and at 675 nm with uncoupled LHCII. Slit widths were 0.5 nm (excitation) and 5 nm (detection) in order to reduce photodegradation while maintaining sufficient detection sensitivity.

Fluorescence decay curves were recorded by time-correlated single photon counting (TCSPC) as described elsewhere[26]. In brief, the samples were excited with vertically polarized 435 nm wavelength light pulses of 0.2 ps duration at a repetition rate of 3.8 MHz, with typically 100 nW average power (annihilation free). Fluorescence was collected at a right angle with respect to the exciting light beam and at magic angle polarization, through a 665 nm long wave pass filter (Schott). Fluorescence decay data were

stored in 4096 channels of a multichannel analyzer (5.0 ps time spacing). The instrument response function (~30 ps FWHM) was obtained with pinacyanol iodide in methanol (10 ps fluorescence lifetime). Decay traces were fitted to a sum of exponentials, with home-built software[27].

The fluorescence setups were equipped with a high-pressure cell (ISS Inc./APP). Samples were in a 6*6 mm quartz cuvette sealed with plastic foil, and placed in the ethanol (spectroscopic grade, Merck) bath which was then pressurized. Pressure was increased in 12 evenly spaced steps from atmospheric pressure to 400 MPa. At each pressure the samples were equilibrated for at least 5 minutes prior to measurements. All experiments were performed at 287 K.

5.3 Results

5.3.1 Steady-state fluorescence

We measured fluorescence emission and excitation spectra of LHCII trimers in micelles at various hydrostatic pressures. As a reference we studied LHCII in which all pigments were uncoupled by 5% Triton X-100 (detection at 675 nm: mostly Chl *a*). The main results are summarized in Table 1 and Figures 1-3. The quenching and spectral shift of fluorescence upon pressure variation were reversible within the accuracy of the experiment.

At 435 nm mostly Chl *a*, and a small amount of Xan and Chl *b* is excited[28]. In the intact complex excitation energy on Xan and Chl *b* is rapidly transferred to Chl *a*[29], therefore almost all fluorescence originates from Chl *a*. In the uncoupled complexes no energy transfer occurs, so both Chl *a* and *b* fluorescence can be observed. Fluorescence detected from Chl *b* is roughly 95% weaker than that from Chl *a* because of (i) selective Chl *a* excitation, (ii) selective detection of Chl *a*, (iii) lower concentration of Chl *b*, and (iv) lower fluorescence quantum yield of Chl *b*[30].

A selection of emission spectra is given in Figure 1. All spectra are corrected for concentration changes due to compression of the solvent[31] and for changes in the absorption at the excitation wavelength by a shift of the absorption bands due to the applied pressure. Such a correction, with the use of excitation spectra, is straightforward because the shape of the 435 nm absorption band does not change significantly upon shifting (based on the excitation spectra, results not shown).

The fluorescence yield decreases with increasing pressure: 0.093 %/MPa for trimeric LHCII and 0.121 %/MPa for uncoupled LHCII (Figure 2, Table 1). The emission spectra shift to the red: 0.118 cm^{-1}/MPa for trimeric LHCII and 0.160 cm^{-1}/MPa for uncoupled LHCII (free pigments in ethanol showed similar results). The fluorescence

quenching and shift resemble those induced by aggregation, although high pressure does not lead to aggregation (see ref. 32 and discussion).

Fluorescence excitation spectra are sensitive to changes in absorption spectra and changes in energy transfer among different pigment molecules[33]. Therefore changes of excitation spectra provide information on conformational changes. Both in the Chl and in the Xan regions the spectra change. Difference spectra are also shown in Figure 3: spectra at 400 MPa minus 0.1 MPa. The spectra were first normalized on the area of the Soret region. A large fraction of the change appeared due to a shift of the Chl spectra. Therefore difference spectra were also calculated from a 400 MPa spectrum that was shifted such that the peak at 435 nm overlapped with the 0.1 MPa spectrum

The fluorescence excitation spectrum of uncoupled LHCII shows no sign of energy transfer from Chl *b* or Xan to Chl *a*, so all pigments are uncoupled. The difference spectrum constructed from the "aligned" 400 MPa spectrum resembles a Chl *b* minus Chl *a* spectrum. So (1) for free Chl the absorption bands shift, and (2) relatively less Chl *a* fluorescence is detected at high pressure. Observation (2) is not due to a relative decrease of the Chl *a* fluorescence quantum yield (see discussion), but due to a red-shift of the emission spectra, which leads to a relative decrease of Chl *a* fluorescence at the detection wavelength (675 nm).

The fluorescence excitation spectrum of trimeric LHCII also shifts. The difference spectrum contructed from the "aligned" 400 MPa spectrum (3.8 nm blue-shifted) shows a decrease in the Chl *a* (375-450 nm) and the Chl *b*/Neoxanthin (488 nm) regions, and an increase at 505 nm.

Table 1. *Main results of steady-state and time-resolved fluorescence experiments: shift of emission maximu (dv/dP), relative fluorescence quantum yield change with pressure ($d\varphi_f/dP$) and fluorescence quantum yield at 400 MPa relative to that at 0.1 MPa (φ_f^{400MPa}). Values result from linear fits of v and φ_f vs. pressure. Standard errors calculated from the fits are in brackets.*

	trimeric LHCII	uncoupled LHCII
dv/dP (cm^{-1}/MPa)[a]	-0.118 (0.011)	-0.160 (0.019)
$d\varphi_f$/dP (%/MPa) [a]	-0.093 (0.003)	-0.121 (0.004)
$d\varphi_f$/dP (%/MPa) [b]	-0.023 (0.001)	-0.0115 (0.0005)
$d\varphi_f$/dP (%/MPa)[c]	-0.091 (0.005)	-[d]
φ_f^{400MPa} (%)[a]	0.623 (0.007)	0.516 (0.009)
φ_f^{400MPa} (%)[b]	0.910 (0.004)	0.954 (0.002)
φ_f^{400MPa} (%)[c]	0.638 (0.017)	-[d]

[a] *from steady state fluorescence,* [b] *from a two-component fit of fluorescence decay,* [c] *from a three-component fit of fluorescence decay,* [d] *a third component was not detected*

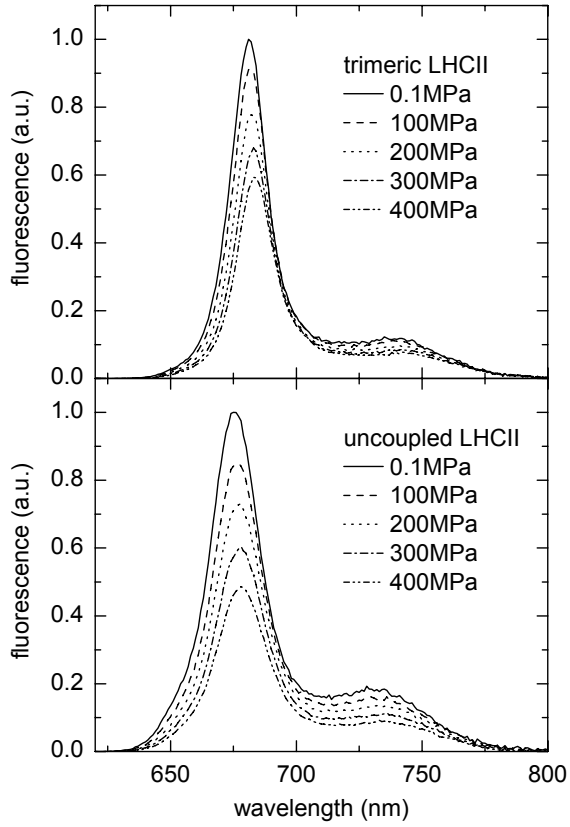

Figure 1. *Fluorescence emission spectra of trimeric (upper) and uncoupled LHCII (5% Triton X-100), at 283 K at different pressures. Spectra were recorded at 33 MPa intervals; for clarity not all spectra are shown.*

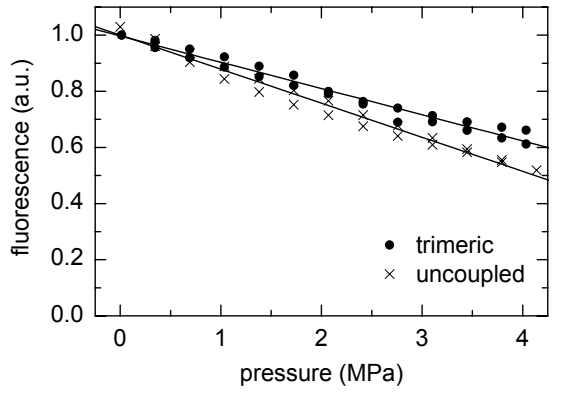

Figure 2. *Integrated fluorescence emission intensity of trimeric and uncoupled LHCII at different pressures, with linear fit (line and dashed line, see also Table 1). Data were obtained at increasing and decreasing pressure, with five minutes equilibration time at each pressure.*

5.3.2 Time-resolved fluorescence

The quenching process(es) were further studied by time-correlated single photon counting (TCSPC). Each fluorescence decay trace was fitted by a sum of exponentials. At each pressure the sum of pre-exponential factors (amplitudes) was normalized. For trimeric LHCII both the amplitudes and the lifetimes depend on pressure, whereas for uncoupled LHCII this is only the case for the lifetimes. The decay times change approximately linearly with pressure. The main TCSPC results are summarized in Table 1 and in Figure 4.

The fluorescence quantum yield at pressure *p* relative to the one at atmospheric pressure is given by equation (1), provided that the two fitted lifetimes are the only ones present in the sample.

$$\varphi_f^p = \frac{a_1^p \tau_1^p + a_2^p \tau_2^p}{a_1^0 \tau_1^0 + a_2^0 \tau_2^0} \qquad (1)$$

In (1) a_n^p and τ_n^p are the amplitude and lifetime of component *n* at pressure *p*, *p* = 0 indicates atmospheric pressure.

Firstly we present the TCSPC results on LHCII trimers. The fluorescence decay is described very well with two lifetimes: τ_1 = ~0.5 ns (very small amplitude) and τ_2 = ~3.5 ns. This agrees with previous experiments, e.g. Palacios et al.[20]. τ_1 slightly increases, τ_2 slightly decreases upon increasing the pressure. The relative fluorescence yield at 400 MPa is 0.91, according to equation (1); However, the steady-state experiments give a value of 0.62 (Figure 2). Thus a two component description of the system is incomplete: an additional fluorescence decay path must be present.

The additional decay path must be fast, or else the quality of the two-component fits would have been bad. To resolve the third lifetime (τ_3) we fitted decay traces at all pressures globally: τ_3 was forced to be equal at all pressures, while all other parameters ($a_{1,2,3}^p$, $\tau_{1,2}^p$) were not restricted.

An additional lifetime was now resolved: τ_3 = 25 ps. The other lifetimes and the ratio a_2/a_1 hardly change. The amplitude a_3 represents the relative concentration of a strongly quenched fraction of LHCII. The concentration increases from 0% at atmospheric pressure to 31% at 400 MPa. The relative fluorescence yield is 0.64, as calculated from equation (1) extended to three lifetimes. This yield is identical (within the errors, see Table 1) to that of the steady-state experiments.

Secondly we present the TCSPC results on uncoupled LHCII. The fluorescence decay curves contain two lifetimes: ~2 ns (Chl *b*) and ~5.7 ns (Chl *a*) (lifetime attribution with ref. 30). Both lifetimes decrease with increasing pressure (Figure 4). The corresponding amplitudes do not change. The total fluorescence at 400 MPa is 95% relative

to that at atmospheric pressure as calculated according to equation (1); However, the steady-state experiments give 52%.

The remaining 43% of fluorescence quenching must be caused by ultrafast quenching of a large fraction of the Chls. Global analysis did not resolve an additional decay path. Therefore the lifetime should be shorter than the time resolution (~5-10 ps).

If an addional fluorescence lifetime component exists, and this component is not present at atmospheric pressure, then the relative quantum yield is given by (2).

$$\varphi_f^p = \frac{a_1^p \tau_1^p + a_2^p \tau_2^p + a_3^p \tau_3^p}{a_1^0 \tau_1^0 + a_2^0 \tau_2^0} \qquad (2)$$

With φ_f^{400MPa} = 1-0.49 = 0.51 and using $\tau_3 \leq 10$ ps it follows that $a_3^{400MPa} \approx 0.47$. So in uncoupled LHCII 47% of all Chl is in a strongly quenched state at 400 MPa. The relative amplitudes of Chl *a* and *b* do not depend on pressure. So fluorescence quenching is equally strong for Chl *a* and *b*.

5.4 Discussion

5.4.1 Fluorescence excitation spectra

The fluorescence excitation difference spectrum of trimeric LHCII at 400 MPa minus 0.1 MPa shows a decrease in the Chl *a* region and the Chl *b*/Neoxanthin region (~488 nm), and an increase at 505 nm (Figure 3). It is remarkable that *in vivo* quenching is accompanied by an absorption increase at 505 nm, which is usually ascribed to de-epoxidation of Violaxanthin into Zeaxanthin[34]. In our sample such a de-epoxidation does not take place and the increase is most likely due to a red shift of one (or more) of the carotenoids. However, we cannot be sure that the spectral change is directly related to the fluorescence quenching.

5.4.2 The 25 ps fluorescence lifetime of trimeric LHCII

The fluorescence quenching of trimeric LHCII upon increasing pressure from atmospheric to 400 MPa is 37%. 26% of the quenching is due to the formation of a 25 ps decay path. The fraction of LHCII trimers with this fluorescence lifetime increases from 0 to 31% when the pressure increases from atmospheric pressure to 400 MPa. Our experiments do not give information on the nature of the quenching species. We used very low excitation power (<0.1 pJ per pulse, 3.8 MHz repetition rate), so the 25 ps decay is not due to singlet-singlet or singlet-triplet annihilation.

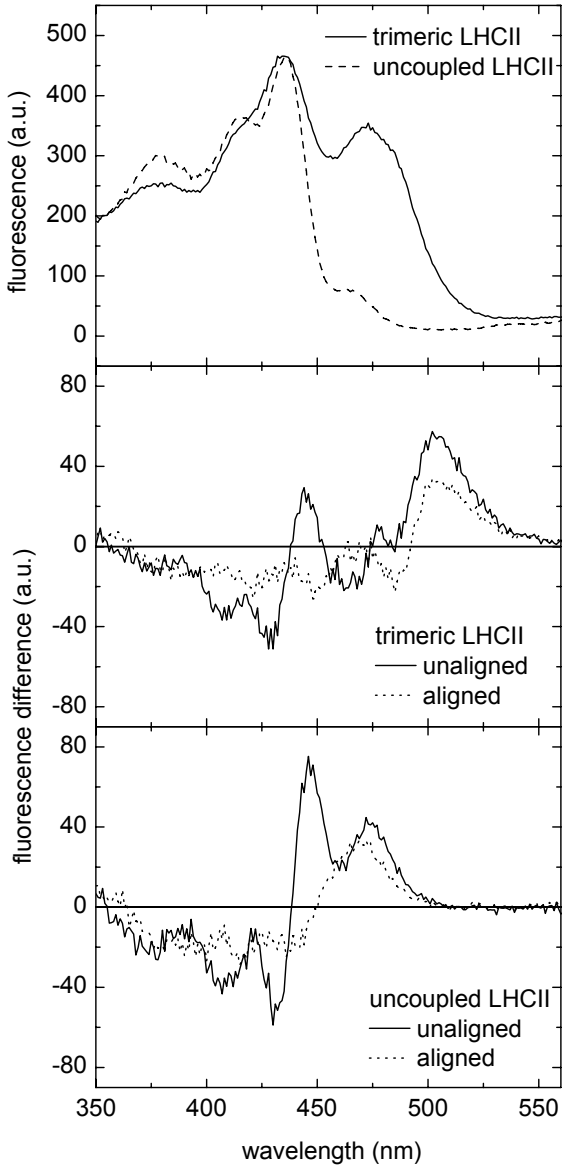

Figure 3. *Fluorescence excitation spectra of trimeric LHCII (detection at 681 nm) and uncoupled LHCII (detection at 675 nm) at 0.1 MPa (upper), and fluorescence excitation difference spectra (400 MPa - 0.1 MPa) of trimeric LHCII (middle) and uncoupled LHCII (lower). Difference spectra were calculated after normalizing the area of the Soret region of the spectra. Difference spectra calculated from spectra that were aligned on the 435 nm peak are shown in dotted lines.*

One strongly quenched Chl can quench all the fluorescence of an LHCII trimer. The time needed for an excitation on an arbitrary pigment within the trimer to reach a quencher is expected to be of the order of the spatial excitation equilibration time. This time was estimated to be 48 ps in trimeric LCHII and 32 ps in trimeric units within aggregated LHCII[35]. Thus it seems likely that the 25 ps lifetime reflects the time for an excitation to

reach a single quenching site in a trimer. This means that, with 42 Chls per trimer[16], less than 1% of all Chls is highly quenched, whereas in uncoupled LHCII 47% of all Chls is highly quenched. The possible role of this quenching *in vivo* will be discussed below.

5.4.3 The ~0.5 ns component is not caused by aggregation

Several arguments plead against the ~0.5 ns component originating from aggregates of LHCII: (1) The changes in the absorption spectra due to pressure are identical in LHCII in agarose gel (no aggregation), and under high detergent concentration[32]; (2) The fluorescence quenching is the same in LHCII in agarose gel and in micelles[32]; (3) The aggregation dependent scatter does not change (Figure 3 and ref. 32); (4) The fluorescence lifetime of the ~0.5 ns component increases with pressure, whereas the lifetimes of aggregates decrease (results not shown); (5) The change of relative ampludes of the various decay paths was completely reversible in trimeric LHCII, and not in aggregates (results not shown).

5.4.4 The longer fluorescence lifetimes of trimeric LHCII

What do the two major fluorescence lifetimes of trimeric LHCII mean? Moya et al.[19], and later Huyer et al.[18], correlated two lifetimes to two conformations of the LHCII, one of which might function as a sink for excess light energy, and the other as an efficient light harvester. Some studies found single-exponential fluorescence decay[20,35], and the number of lifetimes seems to depend on sample preparation[36]. The pressure dependence of the amplitudes of the lifetimes provides additional information.

Suppose the two lifetimes correspond to two distinct conformations of LHCII. The concentration (proportional to $a_{1,2}$) of each conformation depends on pressure (Figure 4). An increase in pressure favors reduction of the volume of a system. Neglecting higher order terms with respect to pressure, the Gibbs free energy difference between two states (ΔG_{12}) is a linear function of pressure (3).

$$\Delta G_{12} = -RT \ln K_{12} = \Delta G_{12}^{0} + p\Delta V_{12} \tag{3}$$

where ΔG^{0}_{12} is the standard Gibbs free energy difference (at 0.1 MPa (1 bar), 297 K); ΔV_{12} the partial molar volume difference between the two states; R the gas constant; T temperature; *p* pressure; and K_{12} the equilibrium constant governing the process. Thus in an equilibrium of two conformations the K_{12} depends on pressure as (4).

$$K_{12}(p) = \frac{a_2(p)}{a_1(p)} = e^{-\frac{\Delta G_{12}^{0} + p\Delta V_{12}}{RT}} = c_1 * e^{-c_2 p} \tag{4}$$

with constants $c_1 = e^{-\frac{\Delta G^0_{12}}{RT}}$ and $c_2 = \frac{\Delta V_{12}}{RT}$.

We obtained a good fit of the ratio of amplitudes to equation (4) (Figure 5), with ΔG^0_{12} = -7.0 (0.3) kJ/mol and ΔV_{12} = 5.3*10^{-6} (1.5*10^{-6}) m^3/mol, or 8.8*10^{-3} (2.5*10^{-3}) nm^3/trimer (values in parentheses indicate 95% confidential intervals). The volume of trimeric LHCII is approximately 150 nm^3, as calculated from the LHCII crystal structures of spinach[16] and pea[17], using SwissPdbViewer (version 3.7). The relative volume difference between the two conformations is thus 0.006%. This small structural difference relates well with the very small structural changes observed during quenching by detergent removal (without aggregation)[37].

How does this volume difference relate to the protein compression at 400 MPa? Typical values for the protein compressibility (κ) are in the range 0.05 – 0.15GPa^{-1} (ref. 38). The spectral shift of chromophores in solution depends on pressure according to equation (5), which emerges from the theory of Laird and Skinner[39].

$$\Delta\nu / \Delta p = n\kappa 3^{-1}\left(\nu_m - \nu_{vac}\right) \qquad (5)$$

Δν/Δp is pressure shift of the absorption maximum (in wavenumbers); κ compressibility, ν_m frequency of the absorption maximum at atmospheric pressure; ν_{vac} frequency of the optical transition in vacuum (= 15551 cm^{-1} for Chl *a*[40]); and the attractive chromophore-solvent interaction (E) depends on the intermolecular distance R as E = constant*R^n. Although this equation describes chromophores in solution, it was proven to apply for photosynthetic complexes, provided the Chls are well-separated, with weak electrostatic couplings and with small charge-transfer-state effects[41]. This is the case for LHCII[42-44].

The compressibilty of LHCII at 77 K is 0.045GPa^{-1}, as calculated from the shift of the absorption maximum at 676.1 nm[43], using equation (5).The shift at 287 K is probably several tens of procents higher than at 77 K[45]. Next we will estimate the LHCII compressibility from our data.

If we assume that the pressure shift of the Chl *a* absorption maximum is roughly equal to the shift of the emission maximum, the compressibility at 287 K is 0.08GPa^{-1} (with ν_m = 675 nm, Δν/Δp = -0.012 cm^{-1}/MPa). This assumption is not entirely correct: after absorption the excitation energy redistributes over the Chls *a*, with different absorption maxima. These maxima, between 664.9 and 683.3 nm[46], correspond to compressibilities between 0.12GPa^{-1} and 0.06GPa^{-1}. Most of the fluorescence originates from the red Chls, which indicate a compressibility of 0.06-0.08GPa^{-1}. This compares well with the value calculated from the 77 K absorption spectra. We conclude that LHCII compression is approximately 3% at 400 MPa.

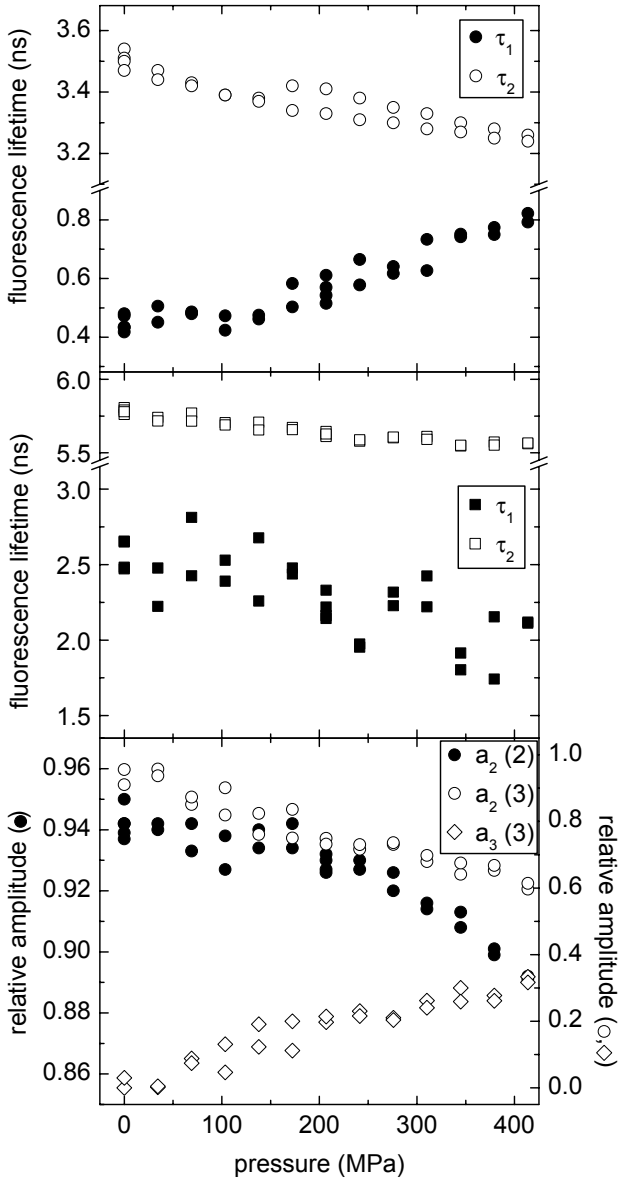

Figure 4. *Fit results of fluorescence decay: lifetimes of trimeric LHCII (upper) and uncoupled LHCII (middle). The relative amplitudes of two-component (a_2 (2)) and three-component fits (a_2 (3) and a_3 (3)) for trimeric LHCII are in the lower panel. At each pressure the sum of amplitudes equals unity (including unshown amplitude 1). The lifetimes are the results of two-component fits, and are identical to those of the fit with an additional (25±9 ps) component. The relative amplitudes of uncoupled LHCII were independent of pressure, a_1 = 0.101 (standard error: 0.008) and a_2 = 0.899 (standard error: 0.008).*

Thus the volume difference between the two conformations (ΔV_{12}) is much smaller (0.006%) than the LHCII volume difference between atmospheric pressure and 400 MPa (~3%). This suggests that ΔV_{12} may depend on pressure, which would explain the slight deviation between our data and the fit with equation (4) (Figure 5). Nevertheless, equation (4) still describes the data fairly well. This has some implications.

Firstly, the amplitudes behave according to the thermodynamical description of a two-state system. So the two fluorescence lifetimes represent two states, i.e. two different protein conformations, in agreement with results from low-temperature time-resolved fluorescence[18,19]. Moreover the results show that these states are in a dynamic equilibrium.

Secondly, the two conformations are quite resistant to pressure: the volume decrease due to pressure exceeds the volume difference between the conformations 500-fold, yet there remain two distinct conformations (the conformations maintain distinct fluorescence lifetimes). Apparently the pressure-induced volume changes affect mainly other conformational properties than those that form the difference between the two conformations identified by the two lifetimes. It points to a local conformational change with a volume change that is much smaller than the overall volume change upon compression.

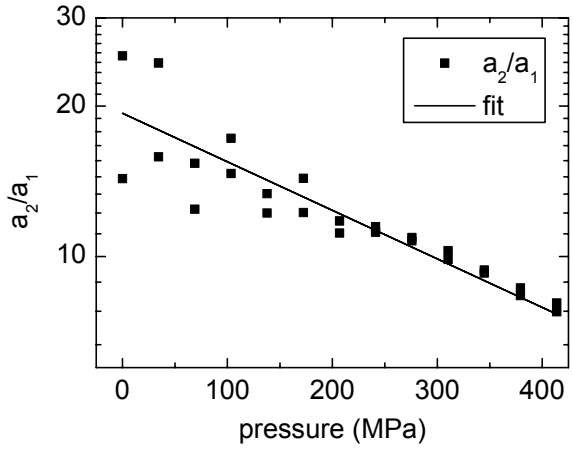

Figure 5. *Ratio a_2/a_1 from the three-lifetime analysis of time-resolved fluorescence of trimeric LHCII fitted with equation (4). See text for more details.*

Several processes can lead to a volume difference in the order of ΔV_{12} (5ml/mol) and an energy difference of ΔG^0_{12} (-7.0 kJ/mol), for example: hydrogen bond formation and solvation of singly charged ions[47]. Cis-trans isomerization of a carotenoid can also lead to a similar volume change, e.g. in bacteriorhodopsin[48], however the free energy change of this reaction is 59 kJ/mol[49], much higher than our ΔG_{12}. It should be noted that, in contrast with LHCII, in bacteriorhodopsin the chromophore is covalently bound to the protein. Bending of a carotenoid would probably lead to a smaller volume and energy change than isomerization. Raman spectroscopy showed two major difference between non-quenched LHCII trimers in micelles and quenched LHCII crystals: bending of the Neoxanthin and hydrogen bonding of at least one Chl *b*[15]. Lampoura et al demonstrated changes in the Chl-Car interaction upon aggregation[50], and Wentworth et al. correlated the transition of LHCII from an non-quenched to a quenched state with a perturbation in the Lut 1 region[37].

Although LHCII crystals are in a quenched state[15], most spectroscopic data on (non-quenched) trimeric LHCII can be explained by the crystal structure[51]. All these observations are in agreement with the small volume and energy differences we measure.

5.4.5 The nature of the quenchers/Quenching *in vivo?*

Aggregation of LHCII leads to fluorescence quenching (see e.g. ref. 52), and may play a role in NPQ[53]. Different mechanisms have been suggested to explain this quenching: It could either be caused by (i) a small population of strongly quenched LHCIIs, that also quench fluorescence of connected LHCII (e.g. ref. 52); or (ii) by conformational changes of a large fraction of LHCII, thereby less strongly quenching fluorescence of each LHCII (e.g. ref. 6). From our results we cannot conclude which mechanism is the most likely one: the fluorescence quenching is both due to the formation of quenched species (τ = 25 ps), and to conformational switching of LHCII between two conformations with different quenching rates. The energy difference between these two conformations is small, an therefore the quenched conformation may be stabilized by environmental changes (such as pH, membrane structure, aggregation) induced by high light intensities.

5.5 Conclusions

We have shown that: (i) Pressure creates a quenching species in trimeric LHCII. The lifetime of quenched trimers is 25 ps, which reflects the excitation equilibration time, or in other words, the time to reach an ultrafast quencher somewhere within the trimer. (ii) The fluorescence of uncoupled LHCII, and thus of individual chromophores, is far more susceptible to quenching than the chlorophylls in trimeric LHCII (approximately 50-fold). (iii) The two longer fluorescence lifetimes of trimeric LHCII originate from two protein conformations. These conformations are in a dynamic equilibrium which is shifted by pressure. The volume difference between the two conformations is 5 ml/mol, or 0.006%, pointing to a local conformational switch between a quenched and an non-quenched trimer. This volume difference is in agreement with the small structural differences between non-quenched LHCII in micelles and quenched LHCII crystals[15]. We cannot be sure that a similar way of quenching also occurs in vivo. It has recently been argued that the structure of the LHCII trimer in detergent is not identical to the structure in the thylakoid membrane[54]. However, our measurements show that such a change can readily occur in LHCII. The rapid quencher (25 ps), could also be physiologically relevant. It can only be present in few LHCII trimers, to prevent too strong quenching.

Thus it appears that within LHCII the Chls are organised such that they are not susceptible to random, uncontrolled quenching. It should be noted that reconstituted and

monomeric LHCII always show a higher degree of quenching and the organization appears to be less "perfect"[36,37]. At the same time different conformations exist with different fluorescence yields and the difference in free energy between them is high enough to keep the quenched state population low under normal conditions, but low enough (much lower than the energy of a photon) to switch in a controlled way. These properties guarantee efficient light harvesting, while at the same time maintaining the capacity to switch to a quenched state, possibly a physiologically relevant quenching one. These results indicate that conformational changes of LHCII can play a role in NPQ *in vivo*.

Acknowledgements

This work is part of the research program of the ''Stichting voor Fundamenteel Onderzoek der Materie (FOM)'', which is financially supported by the ''Nederlandse Organisatie voor Wetenschappelijk Onderzoek (NWO)''. B.v.O. was supported by FOM.

References

1. Barber, J. (1995), *Aust. J. Plant Physiol.* **22**, 201-208.
2. Horton, P., Ruban, A. V. and Walters, R. G. (1996), *Annu. Rev. Plant Physiol. Plant Mol. Biol.* **47**, 655-684.
3. Niyogi, K. K. (1999), *Annu. Rev. Plant Physiol. Plant Mol. Biol.* **50**, 333-359.
4. Demmig-Adams, B. (1990), *Biochim. Biophys. Acta* **1020**, 1-24.
5. van Oort, B. F., Ruban, A. V., van Hoek, A. and van Amerongen, H. Aggregation of LHCII leads to the creation of fluorescence quenchers. In: van der Est, A. and Bruce, D., editors; 2004 Montreal, Canada. Alliance Communications Group, Kansas, USA. p. 142-144.
6. Horton, P., Wentworth, M. and Ruban, A. V. (2005), *FEBS Lett.* **579**, 4201-4206.
7. Aspinall-O'Dea, M., Wentworth, M., Pascal, A., Robert, B., Ruban, A. V. and Horton, P. (2002), *Proc. Natl. Acad. Sci. U. S. A.* **99**, 16331-16335.
8. Bassi, R. and Caffarri, S. (2000), *Photosynth. Res.* **64**, 243-256.
9. Holt, N. E., Zigmantas, D., Valkunas, L., Li, X.-P., Niyogi, K. K. and Fleming, G. R. (2005), *Science* **307**, 433-436.
10. Horton, P., Ruban, A. V. and Wentworth, M. (2000), *Philos. Trans. R. Soc. Lond. B Biol. Sci.* **355**, 1361-1370.
11. Li, X.-P., Gilmore, A. M., Caffarri, S., Bassi, R., Golan, T., Kramer, D. and Niyogi, K. K. (2004), *J. Biol. Chem.* **279**, 22866-22874.
12. Ruban, A. V., Pascal, A. A., Robert, B. and Horton, P. (2002), *J. Biol. Chem.* **277**, 7785-7789.
13. Ruban, A. V. and Horton, P. (1999), *Plant Physiol.* **119**, 531-542.
14. Ruban, A. V., Young, A. and Horton, P. (1994), *Biochim. Biophys. Acta* **1186**, 123-127.
15. Pascal, A. A., Liu, Z. F., Broess, K., van Oort, B., van Amerongen, H., Wang, C., Horton, P., Robert, B., Chang, W. R. and Ruban, A. (2005), *Nature* **436**, 134-137.
16. Liu, Z. F., Yan, H., Wang, K., Kuang, T., Zhang, J., Gui, L. and Chang, W. (2004), *Nature* **428**, 287-292.
17. Standfuss, J., Terwisscha van Scheltinga, A. C., Lamborghini, M. and Kühlbrandt, W. (2005), *EMBO J.* **24**, 919-928.

18. Huyer, J., Eckert, H.-J., Irrgang, K.-D., Miao, J., Eichler, H.-J. and Renger, G. (2004), *J. Phys. Chem. B* **108**, 3326-3334.
19. Moya, I., Silvestri, M., Vallon, O., Cinque, G. and Bassi, R. (2001), *Biochemistry* **40**, 12552-12561.
20. Palacios, M. A., de Weerd, F. L., Ihalainen, J. A., van Grondelle, R. and van Amerongen, H. (2002), *J. Phys. Chem. B* **106**, 5782-5787.
21. Caffarri, S., Croce, R., Breton, J. and Bassi, R. (2001), *J. Biol. Chem.* **276**, 35924-35933.
22. Kitamura, Y. and Itoh, T. (1987), *J. Solution Chem.* **16**, 715-725.
23. Dall'Osto, L., Caffarri, S. and Bassi, R. (2005), *Plant Cell* **17**, 1217-1232.
24. Croce, R., Canino, G., Ros, F. and Bassi, R. (2002), *Biochemistry* **41**, 7334-7343.
25. Porra, R. J., Thompson, W. A. and Kriedemann, P. E. (1989), *Biochim. Biophys. Acta* **975**, 384-394.
26. Borst, J. W., Hink, M. A., van Hoek, A. and Visser, A. J. W. G. (2005), *J. Fluoresc.* **15**, 153-160.
27. Digris, A. V., Skakoun, V. V., Novikov, E. G., van Hoek, A., Claiborne, A. and Visser, A. J. W. G. (1999), *Eur. Biophys. J.* **28**, 526-531.
28. Croce, R., Cinque, G., Holzwarth, A. R. and Bassi, R. (2000), *Photosynth. Res.* **64**, 221-231.
29. Connelly, J. P., Müller, M. G., Hucke, M., Gatzen, G., Mullineaux, C. W., Ruban, A. V., Horton, P. and Holzwarth, A. R. (1997), *J. Phys. Chem. B* **101**, 1902-1909.
30. Seely, G. R. and Connolly, J. S. 1986. Fluorescence of photosynthetic pigments in vitro. In Light emission by plants and bacteria, editors: Govindjee, Amesz, J. and Fork, D. C., Academic Press, Inc., Orlando. p. 99-133.
31. Fine, R. A. and Millero, F. J. (1973), *J. Chem. Phys.* **59**, 5529-5536.
32. Connelly, J. P., Ruban, A. V. and Horton, P. Pressure induced fluorescence quenching in plant light harvesting complex II. In: Isaacs, N. S., editor; 1998 p. 417-422.
33. van Amerongen, H., Valkunas, L. and van Grondelle, R. 2000. Photosynthetic excitons. World Scientific Publishing, Singapore. 590 p.
34. Yamamoto, H. Y., Kamite, L. and Wang, Y.-Y. (1972), *Plant Physiol.* **49**, 224-228.
35. Barzda, V., Gulbinas, V., Kananavicius, R., Cervinskas, V., van Amerongen, H., van Grondelle, R. and Valkunas, L. (2001), *Biophys. J.* **80**, 2409-2421.
36. Palacios, M. A., Standfuss, J., Vengris, M., van Oort, B. F., van Stokkum, I. H. M., Kühlbrandt, W., van Amerongen, H. and van Grondelle, R. (2006), *Photosynth. Res.* **88**, 269-285.
37. Wentworth, M., Ruban, A. V. and Horton, P. (2003), *J. Biol. Chem.* **278**, 21845-21850.
38. Reddy, N. R. S., Wu, H.-M., Jankowiak, R., Picorel, R., Cogdell, R. J. and Small, G. J. (1996), *Photosynth. Res.* **48**, 277-289.
39. Laird, B. B. and Skinner, J. L. (1989), *J. Chem. Phys.* **90**, 3274-3281.
40. Renge, I. (1992), *Chem. Phys.* **167**, 173-184.
41. Wu, H.-M., Rätsep, M., Jankowiak, R., Cogdell, R. J. and Small, G. J. (1998), *J. Phys. Chem. B* **102**, 4023-4034.
42. Palacios, M. A., Caffarri, S., Bassi, R., van Grondelle, R. and van Amerongen, H. (2004), *Biochim. Biophys. Acta* **1656**, 177-188.
43. Pieper, J., Rätsep, M., Jankowiak, R., Irrgang, K.-D., Voigt, J., Renger, G. and Small, G. J. (1999), *J. Phys. Chem. A* **103**, 2412-2421.
44. van Amerongen, H. and van Grondelle, R. (2001), *J. Phys. Chem. B* **105**, 604-617.
45. Reddy, N. R. S., Wu, H.-M., Jankowiak, R., Picorel, R., Cogdell, R. J. and Small, G. J. (1996), *Photosynth. Res.* **48**, 277-289.
46. Trinkunas, G., Connelly, J. P., Müller, M. G., Valkunas, L. and Holzwarth, A. R. (1997), *J. Phys. Chem. B* **101**, 7313-7320.
47. Mozhaev, V. V., Heremans, K., Frank, J., Masson, P. and Balny, C. (1996), *Proteins: Struct., Funct., Genet.* **24**, 81-91.
48. Bryl, K. and Yoshihara, K. (2002), *Eur. Biophys. J.* **31**, 539-548.

49. Bondar, A.-N., Fischer, S., Suhai, S. and Smith, J. C. (2005), *J. Phys. Chem. B* **109**, 14786-14788.
50. Lampoura, S. S., Barzda, V., Owen, G. M., Hoff, A. J. and van Amerongen, H. (2002), *Biochemistry* **41**, 9139-9144.
51. Novoderezhkin, V. I., Palacios, M. A., van Amerongen, H. and van Grondelle, R. (2005), *J. Phys. Chem. B* **109**, 10493-10504.
52. Mullineaux, C. W., Pascal, A. A., Horton, P. and Holzwarth, A. R. (1993), *Biochim. Biophys. Acta* **1141**, 23-28.
53. Horton, P., Ruban, A. V., Rees, D., Pascal, A. A., Noctor, G. and Young, A. J. (1991), *FEBS Lett.* **292**, 1-4.
54. Lambrev, P. H., Varkonyi, Z., Krumova, S., Kóvacs, L., Miloslavina, Y., Holzwarth, A. R. and Garab, G. (2007), *Biochim. Biophys. Acta* **1767**, 847-853.

Chapter 6

Picosecond fluorescence of intact and dissolved PSI-LHCI crystals

based on:

B. van Oort, A. Amunts, J.W. Borst, A. van Hoek, N. Nelson, H. van Amerongen, R. Croce, 2008. Picosecond fluorescence of intact and dissolved PSI-LHCI crystals. Biophysical Journal, in press.

Abstract

Over the last years many crystal structures of photosynthetic pigment-protein complexes have been determined, and used extensively to model spectroscopic results obtained on the same proteins in solution. However, the crystal structure is not necessarily identical to the structure of the protein in solution. Here we studied picosecond fluorescence of Photosystem I-Light Harvesting Complex I (PSI-LHCI), a multisubunit pigment-protein complex that catalyzes the first steps of photosynthesis. The ultrafast fluorescence of PSI-LHCI crystals is identical to that of dissolved crystals, but differs considerably from most kinetics presented in literature. In contrast to most studies, the present data can be modeled quantitatively with only 2 compartments: PSI core and LHCI. This yields the rate of charge separation from an equilibrated core (22.5+/-2.5 ps) and rates of excitation energy transfer from LHCI to core (k_{LC}) and *vice versa* (k_{CL}). The ratio $R=k_{CL}/k_{LC}$ between these rates appears to be wavelength-dependent and scales with the ratio of the absorption spectra of LHCI and core, indicating the validity of a detailed balance relation between both compartments. k_{LC} depends slightly but non-systematically on detection wavelength, averaging $(9.4+/-4.9\ ps)^{-1}$. R ranges from 0.5 (below 690 nm) to around 1.3 above 720 nm.

6.1 Introduction

The primary steps of photosynthetic conversion of solar energy into chemical energy occur in membrane-bound photosystems (PSs). These photosytems are highly organized pigment-protein complexes. In oxygen-evolving photosynthesis, two photosystems (PSII and PSI) work in series to drive electrons from water to $NADP^+$. In higher plants PSI forms a supercomplex named PSI-LHCI, consisting of a core complex and four light-harvesting complexes (LHCIs). The core complex consists of 15 proteins, which bind ~103 chlorophylls (Chls) *a*, ~20 carotenoids (Cars), three [4Fe4S] clusters, and two phylloquinones[1-4]. It contains the reaction centre (RC), with six Chls, that is responsible for charge separation upon excitation. In higher plants, four LHCIs, which bind together 56 Chls *a* and *b*[1] and ~10 Cars[5,6] are attached to one side of the core[7]. In addition, 9 Chls fill the gap between LHCI and core[1,2], and have been proposed to mediate energy transfer from LHCI to the core[8,9]. The pigments bound to PSI-LHCI fulfil various functions: light-harvesting, charge-separation and electron transport (in the RC), and photoprotection[4]. The pigment density in PSI is higher than in PSII and in contrast to PSII, PSI contains Chls which are substantially lower in excited-state energy ('red' Chls) than the RC Chls[10]. Moreover, the energy transfer from light-harvesting pigments to RC is faster and more efficient in PSI (for an overview, see refs. 11,12).

The core complex of higher plants and cyanobacteria is highly conserved concerning protein composition and protein and pigment organization[1,3]. However, the spectroscopic properties of individual cyanobacteria species, higher plants and red algae differ substantially due to the presence of the red Chls, which have diverse energies and abundance in the different systems[13,14]. In higher plants the red Chls are mainly associated with the outer antenna and in particular with Lhca3 and Lhca4[15-17]. The transfer of excitation energy from these low-energy forms to the RC is a thermally activated process[18] and it has a large influence on the excitation trapping time of the system[13,19,20]. The most advanced compartmental modeling studies on PSI all include at least one compartment that contains red pigments.

The excited-state dynamics of PSI has been studied extensively by time-resolved fluorescence and rather large variations have been observed[8,20-25]. In general bi- and tri-exponential decays are observed for PSI from higher plants[8,20-25]. The fastest component (5-20 ps) is partially attributed to energy transfer from bulk to low-energy chlorophylls and partially to trapping. The second component (20-60 ps) is generally attributed to the trapping from the core complex, and the origin of a slower decay (80-130 ps) is under debate[26]. The shape and the relative intensities of the second and third decay components differ considerably for the various studies, especially in the red part of the spectrum. This suggests differences in the content of the red forms and/or LHCI-core connectivity for the various preparations. Also the interpretation of the results varies: from a trap-limited model in which the excitation-energy migration time is largely neglected[24] to a model in which both migration and charge separation contribute to the trapping kinetics[8,22], even for cyanobacteria, in which LHCI is absent[27].

Several theoretical studies have used the X-ray structures of pea PSI-LHCI[1,2] and cyanobacterial PSI core[3] to model the excited-stated dynamics[9,26,28-30]. However, it is not trivial that the structure and dynamics of a pigment-protein complex are the same in solution and in crystal form. For example, light-harvesting complex II (LHCII), which is part of the PSII supercomplex, shows clear differences in fluorescence and Raman properties for solubilized and crystallized forms[31].

Therefore, it is not *a priori* known whether excited-state properties obtained from theoretical studies based on the PSI-LHCI crystal structure reflect those of PSI-LHCI in solution. This complicates the comparison of results from the theoretical studies with experimental data (which moreover have large variations, see above). For these reasons we have measured the excited-state dynamics of PSI-LHCI crystals, and compared the results with those obtained for solubilized PSI-LHCI crystals. The excited-state dynamics in these two samples were indistinguishable, thus indicating very similar structure and dynamics. Comparison with previously reported fluorescence kinetics shows that many differ from those of the crystals. A novel approach is applied to unveil the fluorescence kinetics upon

selective excitation of either core or LHCI, the trapping time from the equilibrated core in the presence of the antenna, the rates of excitation-energy transfer from core to LHCI and *vice versa* and to explain the wavelength-dependence of the overall trapping time.

6.2 Materials and methods

6.2.1 PSI-LHCI crystal preparation

PSI-LHCI was isolated from *Pisum sativum* (pea), and crystallized as described in ref. 32.

6.2.2 Pigment composition

PSI-LHCI crystals were dissolved in 80 % acetone and the precipitate was removed by centrifugation. Absorption spectra were recorded on a Cary 5E UV-Vis-NIR (Varian Palo Alto, CA). The pigment composition was analyzed by HPLC and fitting of the absorption spectra of the acetone extracts as in ref. 33. Values of 8.5±0.1 for the Chl a/b ratio and of 5.2±0.1 for the Chl/Car ratio were obtained. Out of the 168 Chls, 150 are Chls *a* and 18 Chls *b* and there are 19 β-carotenes, 8 luteins and 5 violaxanthins.

6.2.3 Time-Correlated Single Photon Counting (TCSPC)

PSI-LHCI crystals were solubilized in measuring buffer (10 mM Tricine pH 7.8). Steady-state fluorescence emission spectra, which are necessary to calculate Decay Associated Spectra (DAS), were measured upon excitation at 410 nm or 475 nm on a Spex Fluorolog 3.2.2 (Jobin-Yvon). Fluorescence decay curves were measured by TCSPC using a home-built setup[34]. In brief, vertically polarized excitation pulses were used (410 nm or 475 nm wavelength, 200 fs pulse duration, 3.8 MHz repetition rate). Fluorescence was collected at right angle to the excitation beam, at a rate of ~30000 counts per second, and care was taken to minimize data distortion[35]. The fluorescence light was detected at magic angle polarization, through the following interference filters: 679, 693, 707 and 713 nm (Schott), 724.1, 734.1, 744.1 and 759.4 nm (Balzer). The interference filters were tilted by 5º to prevent reflections. Under the same angle, the filters' transmission spectra were measured on a Cary 5E UV-Vis-NIR spectrophotometer. The spectral widths were 10-15 nm, and transmission maxima are as indicated in Figure 3. Detection times were stored in a multichannel analyzer (4096 channels at 2.0 ps time spacing). All measurements were performed at 287 K, and the number of counts in the peak channel was 30.000 to 50.000.

Curves measured at different excitation and detection wavelengths were globally fitted to a sum of exponential decays that was convoluted with the instrument response

function (irf, ~60 ps fwhm), using home-built software[36]. The irf was determined from the fast decay of pinacyanol iodide in methanol (6 ps, measured with the streak camera detection system, see below). The fitting resulted in Decay Associated Spectra (DAS). The fit quality was evaluated from χ^2, and from plots of the weighted residuals and the autocorrelation thereof. To obtain a good fit for all combinations of excitation and detection wavelength, at least six decay times are needed. The accuracy of $\Delta\bar{\tau}^{L-C}$ and of $\Delta\bar{\tau}^{475nm-412nm}$ (see below) was tested by fixing the fastest lifetime at different values between 15 and 30 ps and re-optimizing the fit of the fluorescence decay traces. The effect appeared to be negligible.

To compare the fit results of PSI-LHCI in solution with PSI-LHCI crystals, decay curves were constructed from the DAS (taking into account the spectral sensitivity of the Fluorescence Lifetime Imaging Microscope), and convoluted with the irf of the FLIM, using a reference convolution routine[37] .

6.2.4 Fluorescence Lifetime Imaging Microscopy (FLIM)

Time-resolved fluorescence of PSI-LHCI crystals was measured by FLIM, with the setup as previously described[38]. In short, two-photon excitation pulses (860 nm wavelength, 150 fs pulse duration, 76 MHz repetition rate) were focused into the sample with a 60x water immersion objective lens (CFI Plan Apochromat, numerical aperture 1.2, Nikon, Tokyo, Japan). Fluorescence was detected via non-descanned single photon counting detection, through two band-pass filters of 700 nm (75 nm width) (HQ700/75 Chroma, Vermont, USA), or one band-pass filter of 730 nm (45 nm width) (XF1097 730AF45, Omega Optical, Vermont, USA). Images of 32x32 pixels were obtained, with 4096 time channels of 3.1 ps. Typically one crystal occupied 300 to 600 pixels of the image.

Care was taken to prevent sample degradation by drying and photobleaching at very high light intensities. Drying led to an increase of the fluorescence lifetime, and was prevented by addition of mother liquid (for composition see ref. 1). Increasing the power 1000-fold by focusing all light on a single pixel, led to bleaching: The fluorescence lifetime increased, the the total fluorescence decreased, and spots of decreased fluorescence were visible by eye. At lower light intensity the signal intensity scaled linearly with the square of the excitation power, confirming excitation via two-photon absorption. Fluorescence kinetics did not depend on excitation light intensity in the power range used for these experiments (0.03-0.30 mW, Figure 11 of Supplementary Material). Each crystal was measured several times, and the results were indistinguishable. In total tens of crystals were measured.

Fitting of the fluorescence kinetics per pixel showed little variation within and between crystals (Figure 1). Therefore, the fluorescence decay curves of all pixels of a

crystal were summed and analyzed with home-built software[36]. The curves were fitted to a sum of exponential decays, convoluted with the irf (25 ps), which was determined from the decay of pinacyanol iodide in methanol. Because of the relatively large background intensity, decay curves were not fitted beyond 1 ns.

The fluorescence decay traces obtained with FLIM are of less quality than those with TCSPC. Several factors are responsible for this: (i) In FLIM the number of photons detected per pixel is low as compared to TCSPC. This results in larger (Poissonian) noise. Summing up the decay curves of all pixels containing crystal-fluorescence partially overcomes this problem. (ii) The time channels are wider in FLIM (3.1 ps) than in TCSPC (2 ps). (iii) FLIM has a larger background signal, due to slightly worse shielding of background light. (iv) The irf of FLIM contains more artefacts due to reflections, caused by the larger amount of optics between sample and detector. (v) The irf can be determined less accurately with FLIM, because the reference compound is in solution, whereas the sample is semi-solid (crystals). However, the irf is narrower than for TCSPC. Therefore, in spite of all these limitations, we were able to obtain high time resolution with the FLIM data, and we could compare the fluorescence kinetics with those obtained by TCSPC of PSI-LHCI in solution

6.2.5 Streak camera

Time-resolved fluorescence of pinacyanol iodide (Exciton Inc, Dayton, Ohio) in methanol was measured on a picosecond time scale, with the set of lasers and the synchroscan streak-camera detection system described in detail elsewhere[39]. In short, vertically polarized excitation pulses (400, 475, or 530 nm, 200 fs duration, 253 kHz repetition rate, 1mW) were focused to a 150 μm spot in a static cuvette containing the sample. Fluorescence was focused into the spectrograph, at right angle to the excitation beam, and at magic angle polarization. The spectrograph horizontally dispersed the fluorescence spectrum into the streak camera, where it was vertically dispersed as a function of time. Streak images obtained by the CCD camera were corrected for non-linearity of the time- and wavelength axes, and the sensitivity of the detection system. The corrected streak images represent two-dimensional datasets of fluorescence intensity as a function of time and wavelength, with spectral resolution 2 nm, and temporal resolution ~1 ps. The images were sliced up into traces of 2 nm width, and fitted by global analysis to a sum of exponentials, using software described in ref. 40. The resulting wavelength-dependent amplitudes provide the DAS. The fluorescence of pinacyanol decays mainly mono-exponentially, with lifetime 6 ps (DAS shown in Figure 10 of Supplementary Material), at all excitation wavelengths, with a small contribution from solvent relaxation upon 530 nm excitation. The kinetics were independent of concentration, and not affected by reabsorption. The 6 ps is of higher precision than the previously reported values, that ranged from 4 to 10 ps[41-46], and therefore

increases the accuracy of TCSPC experiments when pinacyanol is used as a reference to determine the instrument response function.

6.3 Results

6.3.1 PSI-LHCI crystals

The fluorescence kinetics of a single crystal at different excitation intensities are shown in Figure 11 of Supplementary Material. The fluorescence kinetics were indistinguishable for excitation intensities varying ten-fold (0.03-0.30 mW), i.e. a 100-fold variation of the number of excited states. During all experiments the power was within this range. Thus in these experiments the effects of closing reaction centres and/or bleaching and annihilation are negligible.

FLIM experiments comprise TCSPC experiments in each pixel of a microscope image. These individual traces were fitted to a biexponential decay. Figure 1 shows a false-color image of the result of such a fit for a single PSI-LHCI crystal, detected at 670-730 nm (left) or 710-750 nm (middle). The color encodes for the average fluorescence lifetime, calculated from the bi-exponential fit. A frequency histogram of the average lifetime distribution is also shown (right). It is clear that the fluorescence lifetime is nearly the same in all pixels. Therefore, the signals of all pixels were summed in order to increase the signal intensity.

Time-resolved fluorescence of tens of PSI-LHCI crystals was measured. The fluorescence kinetics were identical for all crystals with only few exceptions. The fluorescence decay curves of the crystals with the highest signal to noise ratio were analyzed further. Three of these decay curves are presented in Figure 2. As in Figure 1, the fluorescence decay is faster in the 670-730 nm interval than in the 710-750 nm interval. The decay curves of the five crystals with highest signal intensity were analyzed together, using global analysis, fitting simultaneously the decays at both detection wavelengths. At least three exponentials were needed for a good description of the data, yielding the parameters given in Table 1 (four exponentials gave a negligibly better fit). The main decay lifetimes are ~26 ps (71+/-2 % at 670-730 nm and 57+/-1 % at 710-750 nm), and ~67 ps (26+/-2 % and 37+/-1 %). The third lifetime (~244 ps) contributes ≈<5%. No components with negative amplitude (indicative of energy transfer) were found. These are probably faster than the time resolution of our FLIM setup.

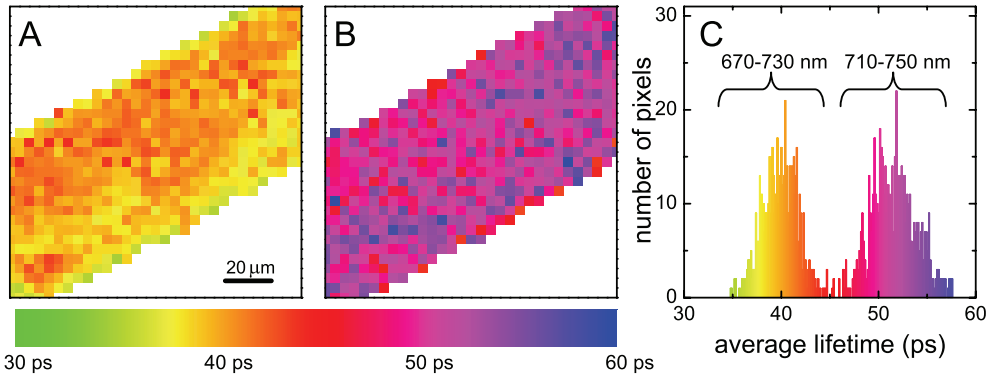

Figure 1. *Fluorescence Lifetime Image of PSI-LHCI crystal, measured at room temperature. False colors represent the average lifetimes at each pixel. The histogram represents the frequency of occurrence of the average lifetime calculated from a two-component fit. Excitation was at 860 nm, detection at 670-730 nm (left, average lifetime: 40 ps) or at 710-750 nm (average lifetime: 51 ps). Colour scale: 30 ps (green) to 60 ps (blue).*

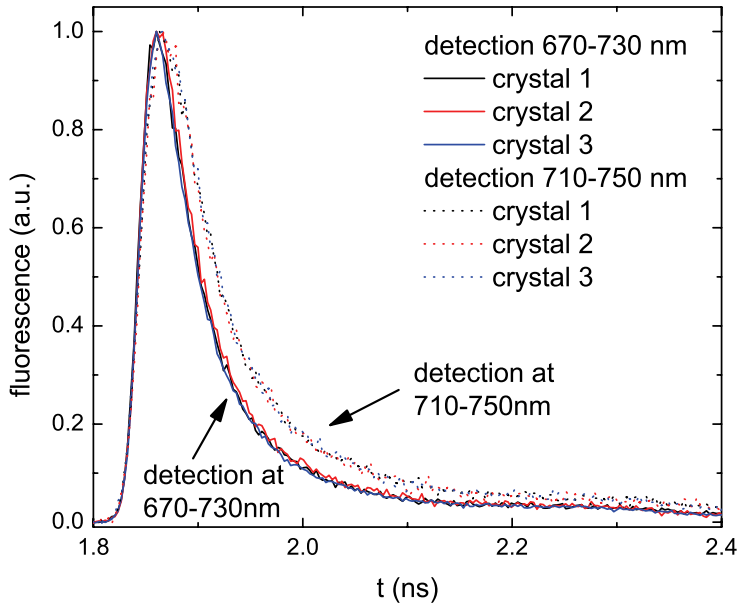

Figure 2. *Normalized sums of fluorescence decay curves of three different PSI-LHCI crystals measured at room temperature with FLIM. Excitation was at 860 nm, detection at 670-730 nm and 710-750 nm (dotted).*

6.3.2 PSI-LHCI in solution

An important question is whether the fluorescence kinetics of PSI-LHCI crystals are the same as those of PSI-LHCI in solution. In order to sort this out, the crystals were solubilized and the steady-state and time-resolved fluorescence were measured. The excitation wavelength was 410 nm or 475 nm, and the detection ranged from 670 to 760 nm. To obtain a good fit of the fluorescence decay traces at all combinations of excitation and detection wavelengths, at least six decay times are needed. Scaling the results of the fitting with the steady-state emission spectra yields the Decay Associated Spectra (DAS, see Figure 3). The main lifetimes are 24 ps (23.7-24.4 ps), 61 ps (60.4-61.5 ps) and 143 ps (141-146 ps). The 95% confidence intervals calculated by exhaustive search are given between brackets. The 24 ps DAS peaks around 690 nm, whereas the other DAS show a red-shift, typical for PSI-LHCI. The red-shift becomes larger with increasing DAS lifetime as was observed before[21]. The nanosecond slow components with small amplitudes may arise from very small amounts of disconnected LHCI and free chlorophyll. The contribution of this slow component is much smaller than in most other studies. The shapes and intensities of the DAS are independent of excitation

Table 1. *Fluorescence decay parameters of PSI-LHCI crystals and PSI-LHCI in solution. Amplitudes p_{cryst} are the average of a global fit of the five crystals with highest signal intensities (with standard deviation, more details in text). Three of these decay traces are shown in Figure 2. Amplitudes p_{sol} are calculated from the DAS in Figure 3 (without the >ns components, more details in text), such that they represent the same spectral window as used for the crystals.*

	PSI-LHCI crystal			PSI-LHCI in solution			
excitation:	860 nm			410 nm		475 nm	
detection:	670-730 nm	710-750 nm		670-730 nm	710-750 nm	670-730 nm	710-750 nm
τ (ns)	p_{cryst}*	p_{cryst}*	τ (ns)	p_{sol}	p_{sol}	p_{sol}	p_{sol}
0.026	0.710 (0.020)	0.570 (0.012)	0.024	0.722	0.551	0.665	0.509
0.067	0.256 (0.021)	0.369 (0.013)	0.061	0.208	0.334	0.257	0.362
0.244	0.035 (0.000)	0.060 (0.002)	0.143	0.063	0.104	0.079	0.117
			0.37	0.006	0.011	0.008	0.012

* *standard deviation between brackets*

wavelength, except for the 24 ps DAS: upon 410 nm excitation the integrated intensity is ~20 % larger than upon 475 nm excitation (Figure 3). It should be noted that the DAS mainly serve as a relatively simply description of the decay curves. As is argued in Appendix A, the decay times are expected to differ at different wavelengths.

At first sight, the lifetimes and amplitudes of PSI-LHCI crystals (Table 1) and PSI-LHCI in solution (Figure 3) are rather similar. In order to perform a quantitative comparison, we calculated the weighted average of the DAS for the FLIM detection regions (670-730 nm or 710-750 nm), taking into account the spectral sensitivity of the FLIM detection system (determined by the optics and detector). The resulting relative amplitudes are presented in Table 1. This shows that the fluorescence kinetics of PSI-LHCI crystals are very similar to those of PSI-LHCI in solution when excited at 410 nm, both upon "blue" (670-730 nm), and "red" (710-750 nm) detection.

To determine to which extent the small differences between PSI-LHCI crystals and PSI-LHCI in solution are due to uncertainty in the fitting, we used a more direct way of comparing the two datasets: the multi-exponential decay of PSI-LHCI in solution (constructed from Table 1) was convoluted with the instrumental response function of the FLIM setup, and subsequently compared with the experimental decay curves of PSI-LHCI crystals. It is clear that the fluorescence kinetics of PSI-LHCI in crystal and in solution are the same upon 410 nm, and only slightly different upon 475 nm excitation (Figure 4A).

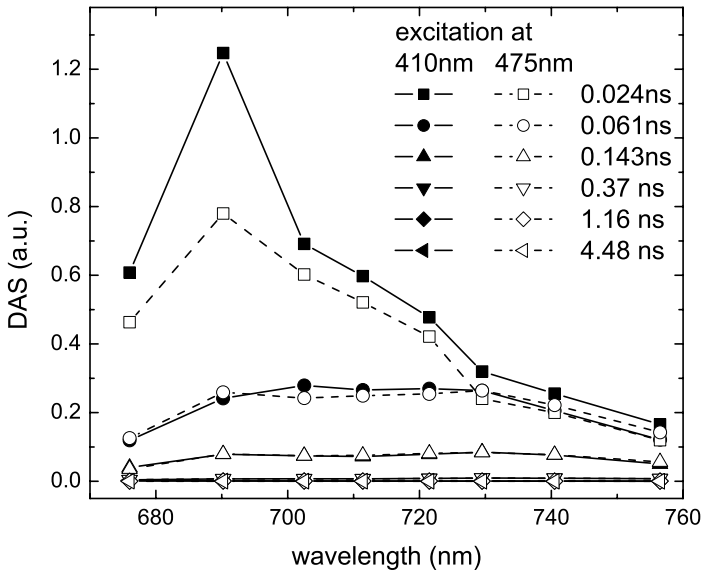

Figure 3. *Decay Associated Spectra (DAS) of PSI-LHCI in solution at 287 K, excited at 410 nm and at 475 nm (dashed). DAS are scaled on the total area of the 61 ps and 143 ps DAS. The slowest three components are presented in more detail in Figure 12 of Supplementary Material.*

6.4 Discussion

6.4.1 PSI-LHCI crystals versus PSI-LHCI in solution

The fluorescence kinetics of PSI-LHCI depend on excitation wavelength (Figure 3), as was shown previously[20,23]. This is due to excitation of different pigments at different wavelengths, which leads to a wavelength-dependent initial excitation distribution over PSI core and LHCI. The fluorescence kinetics of PSI-LHCI crystals, after excitation at 860 nm, are identical to those of PSI-LHCI in solution upon excitation at 410 nm, but not upon excitation at 475 nm (Figure 4A). This implies excitation of the same pigment-protein complexes at 860 nm and 410 nm. The pigments in PSI-LHCI can roughly be divided into three groups: core pigments, LHCI pigments and low-energy chlorophylls ('red Chls'). Below 500 nm the red chlorophylls cannot be excited selectively, so the focus is on the ratio of excited core/LHCI pigments. Upon 410 nm about 65 % of the excitations is created on core Chls, at 475 nm this is about 30 % (based on the absorption spectra in Appendix B and taking into account 70 % Car to Chl transfer efficiency in the core[47] and around 85% in LHCI (E. Wientjes, unpublished results)). Unfortunately two-photon absorption spectra of PSI and LHCI are not available. If only Cars show two-photon absorption of 860 nm light and transfer energy to Chl, then ~60 % of the excitations will "start" on core Chls and ~40 % on LHCI Chls (based on Car contents reported in refs. 1,5,6 and on Car to Chl energy transfer efficiency of 70 % in the core, and 80-90% in LHCI). If only Chl *a* absorbs at 860 nm, then 65 % of the excitations are created in the core and 35 % in LHCI. The two-photon absorption of Chl *b* is 25 times weaker than that of Chl *a*[48] and is not taken into account. So the initial excitation distribution is 60-65 % on the core, and 35-40 % on LHCI, using 860 nm light, very similar to what is calculated for 410 nm excitation. This explains why the fluorescence decay kinetics of PSI-LHCI crystals closely resemble those of PSI-LHCI in solution upon 410 nm excitation, but not upon 475 nm. We conclude that in this preparation of PSI-LHCI from *Pivum sativum* (pea), the fluorescence kinetics are the same in crystals and in solution.

Previous studies on PSI-LHCI showed quite a large variation of fluorescence kinetics (see Introduction). In general three major decay times are found: 5-20 ps, 20-60 ps, 80-130 ps[8,20-25]. The decay times and spectra depend on the type of detergent and its concentration[25], the presence of glycerol[22], and on excitation wavelength[20,23]. The kinetics may further depend on preparation method and plant species. It is of interest to use the atomic structure obtained by X-ray crystallography[1] to explain the observed kinetics[9,26,28]. However, the structure of the different preparations of PSI-LHCI in solution is not necessarily the same as that of pea PSI-LHCI in its crystal lattice. Therefore, the question

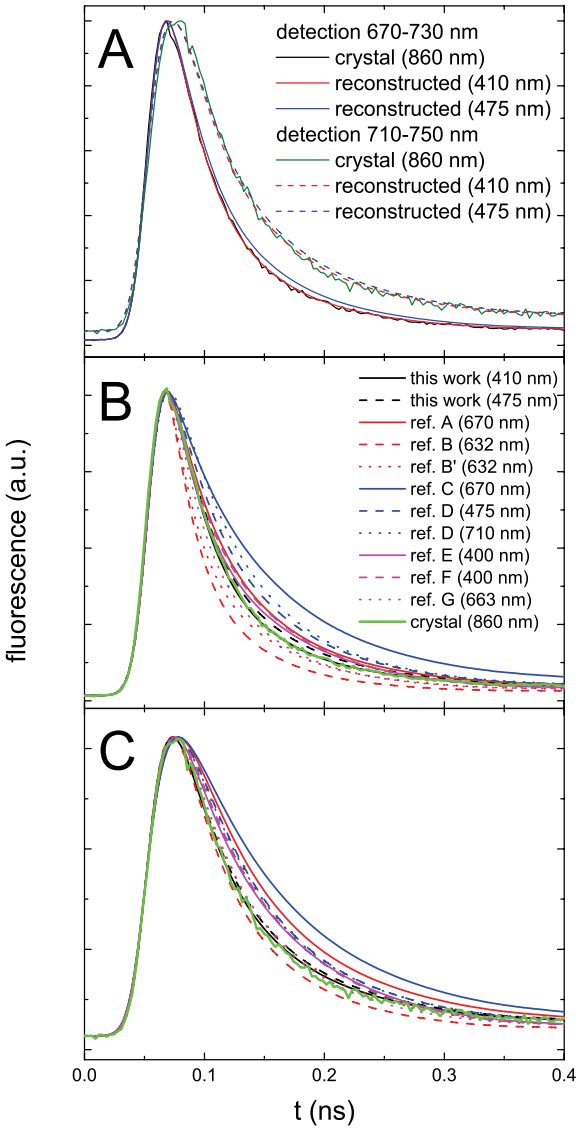

Figure 4. *Sums of fluorescence decay curves of a PSI-LHCI crystal, and reconstructed from the fits of PSI-LHCI in solution (A, see Table 1), or from fluoresecence kinetics from literature (B,C), after correcting for FLIM sensitivity, convoluting with the irf and adding some background signal. Excitation was as indicated in the legend. Detection was as indicated in the legend (A), at 670-730 nm (B) or 710-750 nm (C). Fluorescence kinetics in panels B and C are from: ref. A, [25]; ref. B, [22]; ref. B', [22] with 65 % glycerol; ref. C, [21]; ref. D, [23]; ref. E, [20]; ref. F, [8]; ref. G, [24].*

arose which of the available experimental kinetics correspond to those of the crystal structure.

For that, the fluorescence decay curves were constructed for the kinetics reported in refs. 8,20-25 and solubilized crystals (Table 1). Next, these curves were corrected for spectral sensitivity of the FLIM detection system, and convoluted with the irf. The resulting curves are compared with the experimental FLIM data: In Figure 4A for PSI in solution as measured in the present study, and in Figure 4B and C for several literature values[8,20-25].The

experiments from literature were all performed at excitation wavelengths that lead to ~65 % core excitation, except for ref. 23 (475 nm, ~30 % and 710 nm, ~48 % core excitation), as can be concluded from the absorption spectra in Appendix B, while assuming 70 % Car to Chl transfer efficiency in the core and 80-90 % in LHCI. The curves in Figure 4 clearly show the large variety in reported fluorescence kinetics. At 670-730 nm the kinetics from references 8,20,24,25, and at 710-750 nm from references 22,24 resemble those of the crystals. Only the kinetics reported by Slavov et al.[24] resemble (but are not identical to) those of the crystals at both wavelengths. Particularly at 670-730 nm their kinetics are faster than observed for the crystals. This is in contrast with the kinetics of solubilized PSI-LHCI crystals, which strongly resemble those of the crystals, in both wavelengths ranges. Therefore curves in Figure 4 serve as a warning, setting limits to the possibilities of structure-based modeling of the fluorescence kinetics presented in literature. It is important to realize that the crystallization step requires extremely homogeneous PSI-LHCI, and thereby guarantees very small heterogeneity of the preparation (hetereogeneity can be due to partial dissociation of LHCI, of other subunits, or of pigments), as illustrated by the very small intensity of the nanosecond DAS (Figure 3).

6.4.2 PSI-LHCI in solution

The data on PSI-LHCI in solution are in very good agreement with those on PSI-LHCI crystals. It is therefore worthwhile to evaluate the implications of the observed kinetics in solution on the excited-state dynamics. The main difference between the fluorescence kinetics after 410 nm and 475 nm excitation concerns the amplitude of the fastest decay component, which is approximately 20 % larger upon 410 nm excitation (Figure 3). This leads to the difference $\Delta\bar{\tau}^{475nm-412nm}$ between the average fluorescence lifetimes (calculated as the cross product of relative amplitudes and fluorescence lifetimes) upon 410 nm ($\bar{\tau}^{412nm}$) and 475 nm excitation ($\bar{\tau}^{475nm}$). $\Delta\bar{\tau}^{475nm-412nm}$ was determined at different detection wavelengths but there appeared to be no systematic variation of its value as a function of wavelength, in contrast to what was observed for the values of $\bar{\tau}^{412nm}$ and $\bar{\tau}^{475nm}$ themselves (Figure 5). Therefore, the $\Delta\bar{\tau}^{475nm-412nm}$ values at different detection wavelengths were averaged, leading to $\Delta\bar{\tau}^{475nm-412nm}$ = 3.3+/-1.7 ps, where 1.7 ps is the standard deviation calculated from $\Delta\bar{\tau}^{475nm-412nm}$ at all detection wavelengths. This difference indicates that the overall trapping time depends on the initial excitation distribution over the pigments and it is investigated in more details below.

Upon 410 nm excitation about p = 65 % of the Chl excitations is created in the core, at 475 nm this is about q = 30 % (see above). From these numbers the average lifetimes upon (hypothetical) excitation of only core ($\bar{\tau}^C$) or only LHCI ($\bar{\tau}^L$) can be calculated (Appendix A):

$$\bar{\tau}^c = \frac{q-1}{q-p} * \bar{\tau}^{412nm} - \frac{p-1}{q-p} * \bar{\tau}^{475nm} \quad (1)$$

$$\bar{\tau}^L = \frac{q}{q-p} * \bar{\tau}^{412nm} - \frac{p}{q-p} * \bar{\tau}^{475nm} \quad (2)$$

From these equations it follows that the difference between the average lifetime upon excitation of core and of LHCI ($\Delta\bar{\tau}^{L-C}$) is 9.4+/-4.9 ps, where 4.9 ps originates form the non-systematic variation with wavelength (Figure 5).

Next, the origin of the difference in average lifetime is addressed. In fluorescent systems containing a photosynthetic trap, the average fluorescence lifetime is the sum of two terms: $\bar{\tau} = \tau_{trap} + \tau_{mig}$, where τ_{trap} is the average charge separation time of a photosynthetic system in which the excitations are equilibrated over all the pigments according to the Boltzmann distribution and τ_{mig} is the average time it takes for an excitation to reach the primary electron donor in the RC from an arbitrary pigment of the system, also called the first passage time[49,50]. τ_{trap} is independent of which pigment is

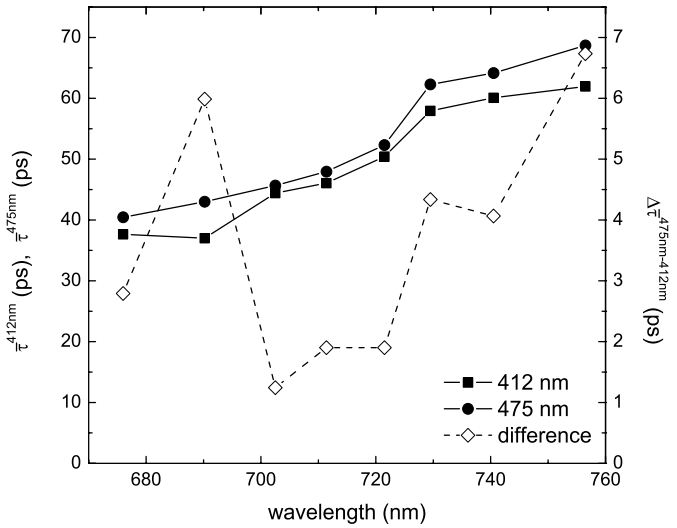

Figure 5. *Average fluorescence lifetimes ($\bar{\tau}$) calculated from the picosecond DAS in Figure 3, upon excitation at 475 nm or 412 nm, and the difference thereof (open symbols, right y-axis). The difference between excitation of core or LHCI equals 2.86 x the difference between excitation at 475 and 412 nm.*

initially excited. Therefore, τ_{mig} must be different upon core (τ_{mig}^{C}) or LHCI (τ_{mig}^{L}) excitation. For further interpretation we introduce a simple model of two interacting clusters/compartments of pigments (core and LHCI, see Figure 6). The equilibration within a cluster or compartment is assumed to be much faster than the transfer between the clusters. Within the context of this model the rate of excitation transfer from LHCI to core (k_{LC}) is given by (derivation in Appendix A):

$$k_{LC} = \frac{1}{\bar{\tau}^{L} - \bar{\tau}^{c}} = \frac{1}{\tau_{mig}^{L} - \tau_{mig}^{C}} = \frac{q-p}{\bar{\tau}^{412nm} - \bar{\tau}^{475nm}} \tag{3}$$

So the difference between the migration times upon core or LHCI excitation ($\Delta\tau_{mig}^{L-C}$) equals the difference between average fluorescence lifetimes upon core or LHCI excitation ($\Delta\bar{\tau}^{L-C}$), which in turn is equal to the inverse (average) rate of energy transfer from LHCI to core $(k_{LC})^{-1}$: 9.4+/-4.9 ps.

The model in Figure 6 permits the calculation of Decay Associated Spectra upon selective excitation of core or LHCI, analogous to the calculation of $\bar{\tau}^{C}$ and $\bar{\tau}^{L}$:

$$DAS_i^{C} = \frac{q-1}{q-p} * DAS_i^{412nm} - \frac{p-1}{q-p} * DAS_i^{475nm} \tag{4}$$

$$DAS_i^{L} = \frac{q}{q-p} * DAS_i^{412nm} - \frac{p}{q-p} * DAS_i^{475nm} \tag{5}$$

for i=1..4

The total area of $DAS_{i=1..4}^{412nm}$ and the total area of $DAS_{i=1..4}^{475nm}$ are normalized. The resulting DAS are given in Figure 7. Again, the main difference is observed for the fastest DAS (24 ps). Upon core excitation, this resembles the fluorescence emission spectrum of PSI core particles, whereas upon LHCI excitation it seems to be a mixture of the spectra of

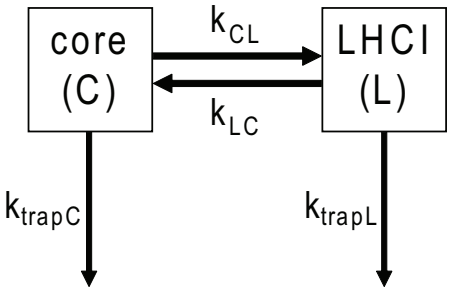

Figure 6. *Model used for interpretation of fluorescence kinetics upon (hypothetical) excitation of only core or only LHCI pigments. Excited-state energy can be transferred from core to LHCI and vice versa, and can be "trapped" by core (via charge separation) and LHCI (via fluorescence, intersystem crossing and internal conversion, with rates k_{trapC} and $k_{trapL,}$ respectively. Equilibration within the core and within LHCI is assumed to occur much faster than transfer between the two compartments. The value of k_{trapL} is neglected because it is two orders of magnitude smaller than k_{trapC}.*

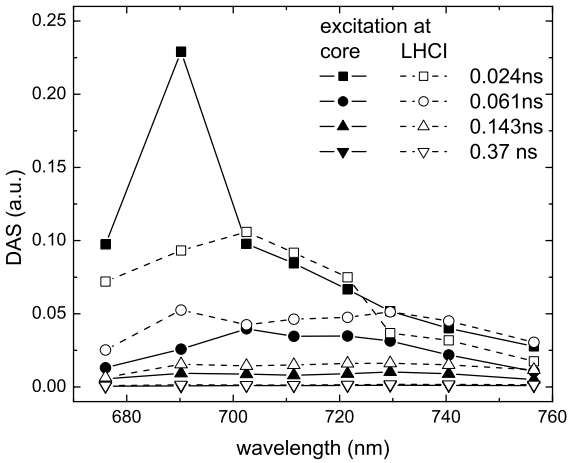

Figure 7. *Decay Associated Spectra (DAS) of PSI-LHCI in solution at 287K, upon (hypothetical) excitation of only core or only LHCI pigments (dashed). DAS were calculated from linear combinations of the DAS in Figure 3, with 65 % core excitation at 410 nm, and 30 % at 475 nm. See text for more details. In Supplementary Material Figure 13 the three slow DAS are presented after scaling to equal area.*

PSI core and LHCI particles. The spectral shapes and relative intensities of the other DAS are very similar for core and LHCI excitation, indicating that after the initial decay of 24 ps, the fluorescence decay kinetics no longer depend on the location of the initial excitation.

For the model in Figure 6 it can be derived (Appendix A) that:

$$k_{trapC} = \frac{1+\frac{k_{CL}}{k_{LC}}}{\bar{\tau}^C} = \frac{1+\frac{\tau_{LC}}{\tau_{CL}}}{\bar{\tau}^C} \equiv \frac{1+R}{\bar{\tau}^C} \tag{6}$$

$$R \equiv \frac{\tau_{LC}}{\tau_{CL}} = k_{trapC} \cdot \bar{\tau}^C - 1 \tag{7}$$

The trapping rate k_{trapC} for excitations in the core can now be estimated from $\bar{\tau}^C$ and R. The ratio R is defined as $R(\lambda) = k_{CL}(\lambda)/k_{LC}(\lambda)$ and it can be approximated as the ratio of the absorption spectra of core and LHCI (see Appendix A). Next, R(λ) is calculated using the value of $\bar{\tau}^C(\lambda)$ (calculated from the DAS in Figure 7) and varying the value of k_{trapC} until optimal agreement was obtained with the value of R(λ) calculated from the spectra (see Figure 8). This leads to an estimated value of $k_{trapC} = (22.5+/-2.5\ ps)^{-1}$ in good agreement with values obtained previously on isolated PSI core particles (e.g. refs. 22,24,25). Note that R(λ) as determined from the ratio of the absorption spectra should be somewhat red-shifted (see Appendix A) for a direct comparison with R(λ) determined from the

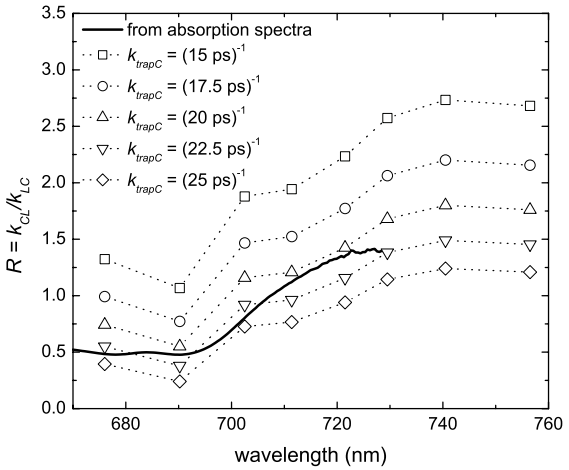

Figure 8. *Ratio $R = k_{CL} / k_{LC}$ calculated from the ratio between the absorption spectra of LHCI and core, and calculated from the average lifetime upon selective excitation of core pigments ($\overline{\tau}^C$) and various rates of trapping from the core (k_{trapC}), using $R = k_{trap} \cdot \overline{\tau}^C - 1$ (see Discussion and Appendix A). R calculated by these two methods coincides rather well for k_{trapC} = (22.5+/-2.5 ps)$^{-1}$. This number was not affected by fixing the fastest lifetime to values ranging from 15 to 30 ps and reoptimizing the fit of the fluorescence decay traces.*

fluorescence kinetics, because of the Stokes' shift. However, as can be seen from Figure 8, shifting the curve somewhat to the red does not alter the conclusion that k_{trapC} = (22.5+/-2.5 ps)$^{-1}$. It is worthwhile noting that no explicit red compartments are needed to describe the data. The red pigments are implicitly included in the compartments of core and LHCI and they contribute to the wavelength dependence of the parameter R.

In conclusion, the fluorescence decay kinetics of PSI-LHCI crystals are identical to those of PSI-LHCI in solution, obtained by solubilization of the crystals. Therefore, our results indicate that the PSI-LHCI conformation and dynamics in the crystal strongly resemble those in solution. Many previous fluorescence experiments on PSI-LHCI in solution differ from the PSI-LHCI crystal data, possibly because of sample heterogeneity, which is much smaller for solubilized crystals. Care should therefore be taken when relating those experiments to the crystal structure.

The fluorescence decay of PSI-LHCI in solution is faster upon excitation at 410 nm than at 475 nm. This is caused by the time for energy transfer from LHCI to PSI core (~9 ps). The initial Decay Associated Spectrum calculated for (hypothetical) excitation of only core pigments is blue-shifted relative to excitation of LHCI pigments. This illustrates the fact that excitations are not instantaneously distributed over the PSI-LHCI according to a Boltzmann distribution. The slower Decay Associated Spectra are very

similar for both excitation wavelengths, showing that after the initial 24 ps process the fluorescence kinetics has become independent of the location of the initial excitation. The fluorescence kinetics of PSI-LHCI can be described with the simple model presented in Figure 6 and the trapping rate for the equilibrated core is $k_{trap} = (22.5+/-2.5\ ps)^{-1}$. The presence of LHCI leads to a slowing down of the overall trapping rate. The wavelength dependence of this overall trapping rate can be explained entirely by rapid equilibration within both core and LHCI followed by wavelength dependent energy transfer between them. The wavelength dependence then stems from the wavelength dependence of the ratio $R = k_{LC}/k_{CL}$ of the energy transfer rates from core to LHCI (k_{LC}) and *vice versa* (k_{CL}), and R is simply equal to the ratio of the number of pigments with energy hc/λ in core and LHCI, respectively, which is in good approximation equal to the ratio of the respective absorption spectra (see Appendix A). This model, which is much simpler than currently available models, which comprise more compartments with spectral forms which cannot be attributed to specific pigments or complexes within the supercomplex, can therefore serve as a starting point for detailed modeling at the molecular level, making use of the PSI-LHCI crystal structure.

6.5 Acknowledgements

This work is part of the research program of the “Stichting voor Fundamenteel onderzoek der Materie (FOM)”, which is financially supported by the “Nederlandse Organisatie voor Wetenschappelijk Onderzoek (NWO)”. B.v.O. was supported by FOM. N.N. acknowledges support from the "Israel Science Foundation" (grant no. 356/06), and R.C. from the "Nederlandse Organisatie voor Wetenschappelijk Onderzoek (NWO)- Earth and Life Science (ALW)" through a VIDI grant.

Appendix A. Derivation of equations describing energy transfer and trapping for the model in Figure 6.

The time dependence of the probabilities C and L that the core or LHCI are excited, respectively, is described by two differential equations, and two boundary conditions:

$$\frac{dC}{dt} = -(k_{trap} + k_{CL}) * C + k_{LC} * L \tag{A1}$$

$$\frac{dL}{dt} = k_{CL} * C - (k_{trapL} + k_{LC}) * L \tag{A2}$$

$$C(t=0) = C_{t=0} \tag{A3}$$

$$L(t=0) = L_{t=0} \tag{A4}$$

These equations lead to expressions for C(t) and L(t):

$$C(t) = \frac{1}{2Z}\left[e^{-\frac{1}{2}Xt}\{C_{t=0}(Z+M) - 2L_{t=0}k_{LC}\} + e^{-\frac{1}{2}Yt}\{C_{t=0}(Z-M) + 2L_{t=0}k_{LC}\}\right] \tag{A5}$$
$$\equiv p_1^C e^{-t/\tau_1} + p_2^C e^{-t/\tau_2}$$

$$L(t) = \frac{1}{2Z}\left[e^{-\frac{1}{2}Xt}\{L_{t=0}(Z-M) - 2C_{t=0}k_1\} + e^{-\frac{1}{2}Yt}\{L_{t=0}(Z+M) + 2C_{t=0}k_1\}\right] \tag{A6}$$
$$\equiv p_1^L e^{-t/\tau_1} + p_2^L e^{-t/\tau_2}$$

with

$$X = k_{CL} + k_{LC} + k_{trapC} + k_{trapL} + \sqrt{(k_{CL} + k_{LC} + k_{trapC} + k_{trapL})^2 - 4(k_{LC}k_{trapC} + (k_{CL} + k_{trapC})k_{trapL})} \tag{A7}$$

$$Y = k_{CL} + k_{LC} + k_{trapC} + k_{trapL} - \sqrt{(k_{CL} + k_{LC} + k_{trapC} + k_{trapL})^2 - 4(k_{LC}k_{trapC} + (k_{CL} + k_{trapC})k_{trapL})} \tag{A8}$$

$$Z = \sqrt{(k_{CL} + k_{LC} + k_{trapC} + k_{trapL})^2 - 4(k_{LC}k_{trapC} + (k_{CL} + k_{trapC})k_{trapL})} \tag{A9}$$

$$M = k_{CL} - k_{LC} + k_{trapC} - k_{trapL} \tag{A10}$$

So *C* and *L* decay (and possibly rise) biexponentially with lifetimes τ_1 and τ_2 and amplitudes p_1^C, p_2^C, p_1^L, and p_2^L. The average fluorescence lifetimes upon excitation of only core ($\bar{\tau}^c$) or only LHCI ($\bar{\tau}^L$) correspond to:

$$\bar{\tau}^C = \frac{p_1^C\tau_1 + p_2^C\tau_2}{p_1^C + p_2^C} \qquad with \;\; C_{t=0} = 1 \;\; and \;\; L_{t=0} = 0 \tag{A11}$$

$$\bar{\tau}^L = \frac{p_1^L\tau_1 + p_2^L\tau_2}{p_1^L + p_2^L} \qquad with \;\; C_{t=0} = 0 \;\; and \;\; L_{t=0} = 1 \tag{A12}$$

Assuming that $k_{trapL} = 0$ (no direct decay from LHCI), and combining the equations above, using $\tau_1 = 2/X$ and $\tau_2 = 2/Y$ and $p_1^C + p_2^C = p_1^L + p_2^L = 1$ (when $C_{t=0} + L_{t=0} = 1$) leads to

$$\bar{\tau}^C = \frac{1}{2Z}\left[\frac{2}{X}(Z + M - 2k_{CL}) + \frac{2}{Y}(Z - M + 2k_{CL})\right] \tag{A13}$$

$$\bar{\tau}^L = \frac{1}{2Z}\left[\frac{2}{X}(Z - M - 2k_{LC}) + \frac{2}{Y}(Z + M + 2k_{LC})\right] \tag{A14}$$

so

$$\begin{aligned}\bar{\tau}^L - \bar{\tau}^C &= \frac{1}{Z}\left[\frac{1}{X}(-2M - 2(k_{LC} - k_{CL})) + \frac{1}{Y}(2M + 2(k_{LC} - k_{CL}))\right] \\ &= -\frac{2}{Z}\left[\frac{1}{X}(M + k_{LC} - k_{CL}) - \frac{1}{Y}(M + (k_{LC} - k_{CL}))\right] \\ &= -\frac{2}{Z}(M + k_{LC} - k_{CL})\left[\frac{1}{X} - \frac{1}{Y}\right]\end{aligned} \tag{A15}$$

Which simplifies further using $M + k_{LC} - k_{CL} = k_{trapC}$ (see above), into

$$\begin{aligned}\bar{\tau}^L - \bar{\tau}^C &= -\frac{2}{Z}k_{trapC} * \left[\frac{1}{X} - \frac{1}{Y}\right] \\ &= -\frac{2}{Z}k_{trapC} * \left[\frac{Y - X}{XY}\right]\end{aligned} \tag{A16}$$

Using $Y - X = 2Z$ and $XY = (k_{CL} + k_{LC} + k_{trapC})^2 - Z^2$, it then follows that

$$\begin{aligned}\bar{\tau}^L - \bar{\tau}^C &= -\frac{2}{Z} k_{trapC} * \left[\frac{-2Z}{(k_{CL} + k_{LC} + k_{trapC})^2 - Z^2} \right] \\ &= \frac{4k_{trapC}}{(k_{CL} + k_{LC} + k_{trapC})^2 - Z^2} \\ &= \frac{4k_{trapC}}{(k_{CL} + k_{LC} + k_{trapC})^2 - \left[(k_{CL} + k_{LC} + k_{trapC})^2 - 4k_{LC}k_{trapC} \right]} \\ &= \frac{1}{k_{LC}} = \tau_{LC}\end{aligned} \tag{A17}$$

i.e.

$$k_{LC} = \frac{1}{\bar{\tau}^L - \bar{\tau}^C} \tag{A18}$$

When at excitation wavelength P a fraction p of the excitations is created in the core, and at wavelength Q fraction q, then (see Discussion)

$$\bar{\tau}^c = \frac{q-1}{q-p} * \bar{\tau}^{412nm} - \frac{p-1}{q-p} * \bar{\tau}^{475nm} \tag{A19}$$

$$\bar{\tau}^L = \frac{q}{q-p} * \bar{\tau}^{412nm} - \frac{p}{q-p} * \bar{\tau}^{475nm} \tag{A20}$$

Introducing theses equations into (A18), gives a new expression for k_{LC}:

$$k_{LC} = \frac{q-p}{\bar{\tau}^{412nm} - \bar{\tau}^{475nm}} \tag{A21}$$

Using $Z + M = X - k_{LC}$ and $Z - M = -Y + k_{LC}$, equation A14 can be rewritten as

$$\bar{\tau}^L = \frac{1}{Z}\left[\frac{1}{X}(-Y + 2k_{LC} - 2k_{LC}) + \frac{1}{Y}(X - 2k_{LC} + 2k_{LC}) \right] \tag{A22}$$

which simplifies into

$$\bar{\tau}^L = \frac{1}{Z}\left[\frac{-Y}{X} + \frac{X}{Y} \right] = \frac{1}{Z}\left[\frac{X^2 - Y^2}{XY} \right] \tag{A23}$$

Substitution of equations A7-9 into A23 then gives

$$\begin{aligned}\bar{\tau}^L &= \frac{1}{Z}\left[\frac{4Z(k_{CL}+k_{LC}+k_{trapC})}{(k_{CL}+k_{LC}+k_{trapC})^2-Z^2}\right] \\ &= \frac{4(k_{CL}+k_{LC}+k_{trapC})}{(k_{CL}+k_{LC}+k_{trapC})^2-Z^2} \\ &= \frac{4(k_{CL}+k_{LC}+k_{trapC})}{4k_{LC}k_{trapC}} \\ &= \frac{k_{CL}+k_{LC}+k_{trapC}}{k_{LC}k_{trapC}}\end{aligned} \tag{A24}$$

This can be rewritten, by defining the ratio $R = k_{CL}/k_{LC}$, so $k_{CL} = k_{LC}R$,

$$\begin{aligned}\bar{\tau}^L &= \frac{(1+R)k_{LC}+k_{trapC}}{k_{LC}k_{trapC}} \\ &= \frac{\frac{(1+R)}{\bar{\tau}^L-\bar{\tau}^C}+k_{trapC}}{\frac{k_{trapC}}{\bar{\tau}^L-\bar{\tau}^C}} \\ &= \frac{1+R+k_{trapC}(\bar{\tau}^L-\bar{\tau}^C)}{k_{trapC}}\end{aligned} \tag{A25}$$

So

$$k_{trapC}\bar{\tau}^L = 1+R+k_{trapC}(\bar{\tau}^L-\bar{\tau}^C) \tag{A26}$$

and

$$k_{trapC} = \frac{1+R}{\bar{\tau}^C} \tag{A27}$$

Or in other words

$$R = k_{trapC}\cdot\bar{\tau}^C - 1 \tag{A28}$$

Note that the trapping time of the core is on the order of tens of ps and the lifetime of LHCI is on the order of ns so the assumption that $k_{trapL} = 0$ is justified. Moreover, in this compartmental model it is assumed that equilibration in a compartment is much faster than the transfer between the compartments. Note that R, k_{CL} and k_{LC} can be wavelength dependent (see below).

In addition, the overall decay can be described as $\bar{\tau} = \tau_{trap} + \tau_{mig}$ (see Discussion) and τ_{trap} is independent of which pigment is initially excited. Therefore, the different average lifetimes upon excitation of either core or LHCI must be caused by variation of τ_{mig}, so

$$k_{LC} = \frac{1}{\bar{\tau}^L - \bar{\tau}^C} = \frac{1}{\tau_{mig}^L - \tau_{mig}^C} \tag{A29}$$

$R(\lambda)$ can be calculated from independent experiments because it should obey the detailed balance equation for the above model:

$$R(\lambda) = \frac{k_{CL}(\lambda)}{k_{LC}(\lambda)} = \frac{n_L(\lambda)}{n_C(\lambda)} * e^{-\Delta E(\lambda)/kT} \tag{A30}$$

where $n_{L,C}$ are degeneracy factors for LHCI and core respectively. In this specific case, n_L and n_C depend on wavelength: $n_{L,C}$ are the number of pigments of excited-state energy $E_{L,C}$, which are responsible for the fluorescence at wavelength λ. ΔE is the energy difference between the relevant pigments of core and LHCI at this wavelength ($\Delta E = E_L - E_C$), which equals zero when measuring at one particular wavelength. This leads to

$$R(\lambda) = \frac{k_{CL}(\lambda)}{k_{LC}(\lambda)} = \frac{n_L(\lambda)}{n_C(\lambda)} \tag{A31}$$

The ratio $n_L(\lambda)/n_C(\lambda)$ can be approximated by the ratio of the absorption spectra[51] of LHCI and core, normalized to the number of Chls ($Abs_{L,C}$), see Appendix B, when the Stokes' shift is neglected. So the ratio of the absorption spectra of LHCI and PSI core (normalized to their pigment contents) provide the ratio of forward and backward energy transfer between core and LCHI. Above ~730 nm, the absorption of the core becomes very small and the accuracy of R decreases. It should be noted that it might seem better to take the steady-state fluorescence spectra to obtain R because the fluorescence and not the absorption is being probed but in that case proper normalization of the spectra is difficult because of the trapping process and possible additional fluorescence quenching mechanisms that can influence the ratio of the fluorescence spectra. Taking the absorption spectra instead leads to a small blue shift of $R(\lambda)$. However, as can be seen in Figure 8, this does not seriously affect the modeling results and the conclusion. It should be noted that the rates are wavelength dependent and therefore it is expected that different lifetimes are observed at different wavelengths. Therefore, strictly speaking, the use of Decay Associated Spectra is not allowed because this assumes the presence of the same decay times at different wavelengths. However, the spectra and the corresponding lifetimes describe the data well and here they are only used to obtain the various average lifetimes at different wavelengths which are used for the modeling.

Appendix B. Absorption spectra of PSI-LHCI, PSI core and LHCI

Absorption spectra of PSI core and LHCI are necessary to determine the selective excitation of core and LHCI pigments at various wavelengths, and to determine the ratio *R* for forward and backward energy transfer between core and LHCI pigments. We recorded absorption spectra of PSI core, LHCI and PSI-LHCI supercomplex. Samples were purified as described previously[52], and absorption spectra were recorded at 290 K using a SLM-Aminco DK2000 spectrophotometer. The results are shown in Figure 9.

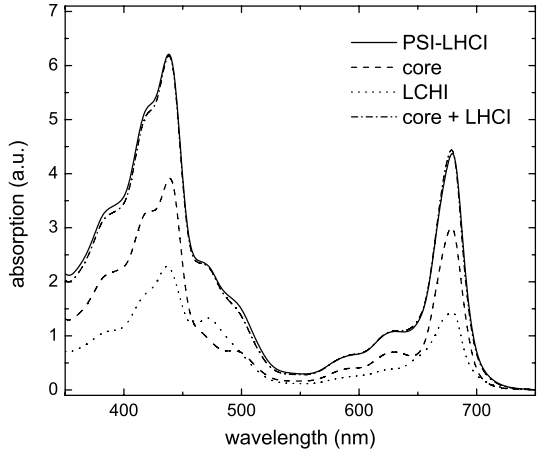

Figure 9. *Absorption spectra of PSI-LHCI, PSI core, LHCI, scaled to the number of pigments. The sum of core and LHCI spectra is also shown.*

Supplementary Material

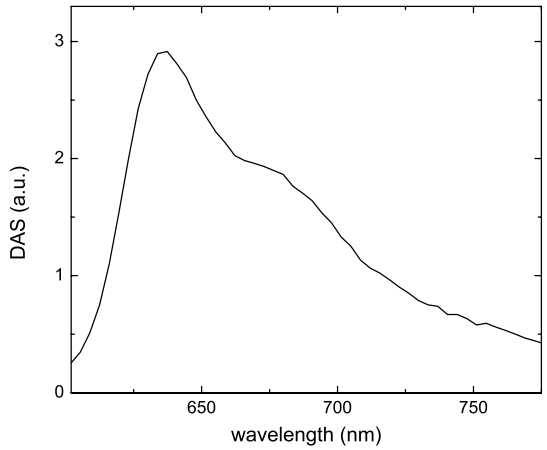

Figure 10. *Decay Associated Fluorescence Spectrum (τ = 6 ps) of pinacyanol iodide in methanol at 294 K. Excitation was at 475 nm, fluorescence was detected with the streak-camera setup.*

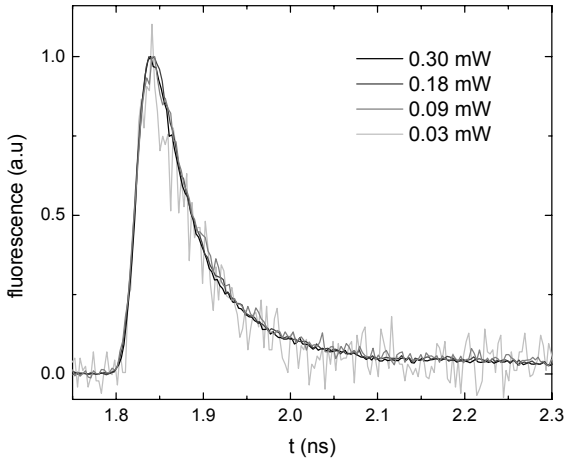

Figure 11. *Sums of fluorescence decay curves of a PSI-LHCI crystal measured at room temperature with FLIM. Data were corrected for background signal, and normalized in the peak. Excitation was at 860 nm, at energies as indicated, detection was at 670-730 nm.*

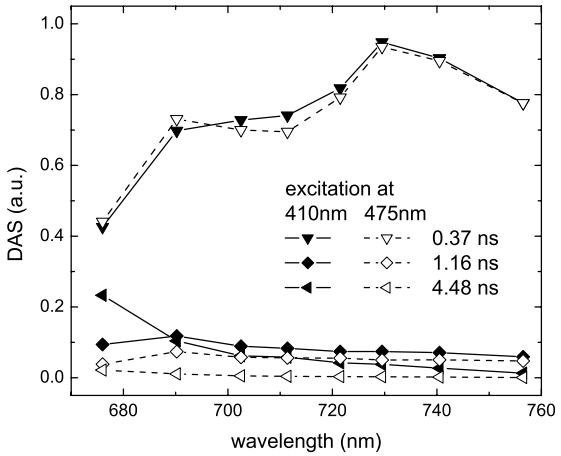

Figure 12. *Decay Associated Spectra (DAS) of the slowest components of PSI-LHCI in solution at 287 K, excited at 410 nm and at 475 nm (dashed), scaled on the total area of the 61 ps and 143 ps DAS (same data as in Figure 3 of the main text, but multiplied by 100).*

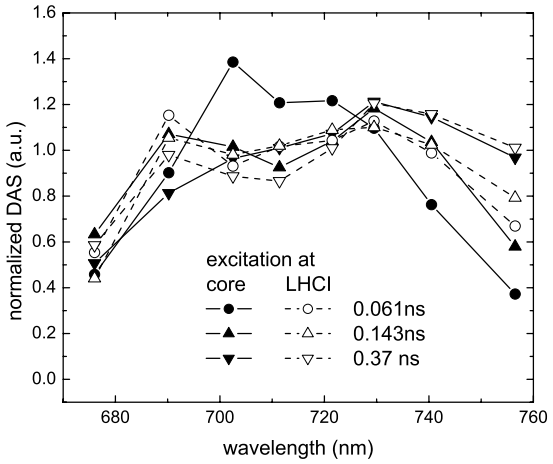

Figure 13. *Decay Associated Spectra (DAS) of PSI-LHCI in solution at 287 K, upon excitation of only core or only LHCI pigments (dashed). DAS were calculated from linear combinations of the DAS in Figure 3 of the main text, with 65 % core excitation at 410 nm, and 30 % at 475 nm. See text for more details. DAS are scaled to equal area (by multiplaction of DAS of 61 ps, 143 ps and 0.37 ns, respectively, by 34.9, 11.5 and 1049 for core excitation, and by 21.9, 67.9 and 670 for LHCI excitation).*

References

1. Amunts, A., Drory, O. and Nelson, N. (2007), *Nature* **447**, 58-63.
2. Ben-Shem, A., Frolow, F. and Nelson, N. (2003), *Nature* **426**, 630-635.
3. Jordan, P., Fromme, P., Witt, H. T., Klukas, O., Saenger, W. and Krauss, N. (2001), *Nature* **411**, 909-917.
4. Jensen, P. E., Bassi, R., Boekema, E. J., Dekker, J. P., Jansson, S., Leister, D., Robinson, C. and Scheller, H. V. (2007), *Biochim. Biophys. Acta* **1767**, 335-352.
5. Castelletti, S., Morosinotto, T., Robert, B., Caffarri, S., Bassi, R. and Croce, R. (2003), *Biochemistry* **42**, 4226-4234.
6. Croce, R., Morosinotto, T., Castelletti, S., Breton, J. and Bassi, R. (2002), *Biochim. Biophys. Acta* **1556**, 29-40.
7. Boekema, E. J., Jensen, P. E., Schlodder, E., van Breemen, J. F. L., van Roon, H., Scheller, H. V. and Dekker, J. P. (2001), *Biochemistry* **40**, 1029-1036.
8. Ihalainen, J. A., Klimmek, F., Ganeteg, U., van Stokkum, I. H. M., van Grondelle, R., Jansson, S. and Dekker, J. P. (2005), *FEBS Lett.* **579**, 4787-4791.
9. Şener, M. K., Jolley, C., Ben-Shem, A., Fromme, P., Nelson, N., Croce, R. and Schulten, K. (2005), *Biophys. J.* **89**, 1630-1642.
10. Nelson, N. and Yocum, C. F. (2006), *Annu. Rev. Plant Biol.* **57**, 521-565.
11. Fromme, P., Schlodder, E. and Jansson, S. 2003. Structure and Function of the Antenna System in Photosystem I. In Light-Harvesting Antennas in Photosynthesis, editors: Green, B. R. and Parson, W. W., Kluwer Academic Publishers, Dordrecht. p. 253-279.
12. van Amerongen, H. and Dekker, J. P. 2003. Light-Harvesting in Photosystem II. In Light-Harvesting Antennas in Photosynthesis, editors: Green, B. R. and Parson, W. W., Kluwer Academic Publishers, Dordrecht. p. 219-251.
13. Gobets, B. and van Grondelle, R. (2001), *Biochim. Biophys. Acta* **1507**, 80-99.
14. Gobets, B., van Amerongen, H., Monshouwer, R., Kruip, J., Rögner, M., van Grondelle, R. and Dekker, J. P. (1994), *Biochim. Biophys. Acta* **1188**, 75-85.
15. Croce, R., Chojnicka, A., Morosinotto, T., Ihalainen, J. A., van Mourik, F., Dekker, J. P., Bassi, R. and van Grondelle, R. (2007), *Biophys. J.* **93**, 2418-2428.
16. Morosinotto, T., Breton, J., Bassi, R. and Croce, R. (2003), *J. Biol. Chem.* **278**, 49223-49229.
17. Schmid, V. H. R., Cammarata, K. V., Bruns, B. U. and Schmidt, G. W. (1997), *Proc. Natl. Acad. Sci. USA* **94**, 7667-7672.
18. Jennings, R. C., Zucchelli, G., Croce, R. and Garlaschi, F. M. (2003), *Biochim. Biophys. Acta* **1557**, 91-98.
19. Gobets, B., van Stokkum, I. H. M., van Mourik, F., Dekker, J. P. and van Grondelle, R. (2003), *Biophys. J.* **85**, 3883-3898.
20. Ihalainen, J. A., van Stokkum, I. H. M., Gibasiewicz, K., Germano, M., van Grondelle, R. and Dekker, J. P. (2005), *Biochim. Biophys. Acta* **1706**, 267-275.
21. Croce, R., Dorra, D., Holzwarth, A. R. and Jennings, R. C. (2000), *Biochemistry* **39**, 6341-6348.
22. Engelmann, E., Zucchelli, G., Casazza, A. P., Brogioli, D., Garlaschi, F. M. and Jennings, R. C. (2006), *Biochemistry* **45**, 6947-6955.
23. Ihalainen, J. A., Jensen, P. E., Haldrup, A., van Stokkum, I. H. M., van Grondelle, R., Scheller, H. V. and Dekker, J. P. (2002), *Biophys. J.* **83**, 2190-2201.
24. Slavov, C., Ballottari, M., Morosinotto, T., Bassi, R. and Holzwarth, A. R. (2008), *Biophys. J.* **94**, 3601-3612.
25. Turconi, S., Weber, N., Schweitzer, G., Strotmann, H. and Holzwarth, A. R. (1994), *Biochim. Biophys. Acta* **1187**, 324-334.
26. Melkozernov, A. N., Barber, J. and Blankenship, R. E. (2006), *Biochemistry* **45**, 331-345.

27. Gobets, B., van Stokkum, I. H. M., Rogner, M., Kruip, J., Schlodder, E., Karapetyan, N. V., Dekker, J. P. and van Grondelle, R. (2001), *Biophys. J.* **81**, 407-424.
28. Yang, M., Damjanovic, A., Vaswani, H. M. and Fleming, G. R. (2003), *Biophys. J.* **85**, 140-158.
29. Brüggemann, B., Sznee, K., Novoderezhkin, V., van Grondelle, R. and May, V. (2004), *J. Phys. Chem. B* **108**, 13536-13546.
30. Damjanovic, A., Vaswani, H. M., Fromme, P. and Fleming, G. R. (2002), *J. Phys. Chem. B* **106**, 10251-10262.
31. Pascal, A. A., Liu, Z. F., Broess, K., van Oort, B., van Amerongen, H., Wang, C., Horton, P., Robert, B., Chang, W. R. and Ruban, A. (2005), *Nature* **436**, 134-137.
32. Amunts, A., Ben-Shem, A. and Nelson, N. (2005), *Photochem. Photobiol. Sci.* **4**, 1011-1015.
33. Croce, R., Canino, G., Ros, F. and Bassi, R. (2002), *Biochemistry* **41**, 7334-7343.
34. Borst, J. W., Hink, M. A., van Hoek, A. and Visser, A. J. W. G. (2005), *J. Fluoresc.* **15**, 153-160.
35. van Hoek, A. and Visser, A. J. W. G. (1985), *Anal. Instrum.* **14**, 359-378.
36. Digris, A. V., Skakoun, V. V., Novikov, E. G., van Hoek, A., Claiborne, A. and Visser, A. J. W. G. (1999), *Eur. Biophys. J.* **28**, 526-531.
37. Boens, N., Ameloot, M., Yamazaki, I. and De Schryver, F. C. (1988), *Chem. Phys.* **121**, 73-86.
38. Russinova, E., Borst, J.-W., Kwaaitaal, M., Cano-Delgado, A., Yin, Y., Chory, J. and de Vries, S. C. (2004), *Plant Cell* **16**, 3216-3229.
39. van Oort, B., Murali, S., Wientjes, E., Koehorst, R. B. M., Spruijt, R., van Hoek, A., Croce, R. and van Amerongen, H. (2008), *submitted*.
40. van Stokkum, I. H. M., Larsen, D. S. and van Grondelle, R. (2004), *Biochim. Biophys. Acta* **1657**, 82-104.
41. Eske, A. T. and Naqvi, R. K. (1979), *Chem. Phys. Lett.* **63**, 128-132.
42. Mialocq, J. C. (1982), *Chem. Phys.* **73**, 107-115.
43. Mialocq, J. C., Jaraudias, J. and Goujon, P. (1977), *Chem. Phys. Lett.* **47**, 123-126.
44. Sundstrom, V. and Gillbro, T. (1981), *Chem. Phys.* **61**, 257-269.
45. Voigt, G., Nowak, F., Ehlert, J., Beenken, W. J. D., Leupold, D. and Sandner, W. (1997), *Chem. Phys. Lett.* **278**, 380.
46. Thistlethwaite, P. J. and Griesser, H. J. (1982), *Chem. Phys. Lett.* **91**, 58-62.
47. de Weerd, F. L., Kennis, J. T. M., Dekker, J. P. and van Grondelle, R. (2003), *J. Phys. Chem. B* **107**, 5995-6002.
48. Leupold, D., Teuchner, K., Ehlert, J., Irrgang, K.-D., Renger, G. and Lokstein, H. (2002), *Biophys. J.* **82**, 1580-1585.
49. van Amerongen, H., Valkunas, L. and van Grondelle, R. 2000. Photosynthetic excitons. World Scientific Publishing, Singapore. 590 p.
50. Broess, K., Trinkunas, G., van der Weij-de Wit, C. D., Dekker, J. P., van Hoek, A. and van Amerongen, H. (2006), *Biophys. J.* **91**, 3776-3786.
51. Laible, P. D., Knox, R. S. and Owens, T. G. (1998), *J. Phys. Chem. B* **102**, 1641-1648.
52. Croce, R., Zucchelli, G., Garlaschi, F. M. and Jennings, R. C. (1998), *Biochemistry* **37**, 17355-17360.

Chapter 7

Summarizing discussion

7.1 Introduction

This thesis focuses on the study of photosynthetic pigment-protein complexes using time-resolved fluorescence techniques. Fluorescence spectroscopy often requires attaching fluorescent labels to the proteins under investigation. With photosynthetic proteins this is not necessary, because these proteins contain fluorescent pigments. Each pigment's fluorescence is influenced by its environment, and thereby may provide information on structure and dynamics of pigment-protein complexes *in vitro* and *in vivo*. Another way to probe protein structure is X-ray diffraction of crystals of the pigment-protein complexes. In this work fluorescence was measured of crystals of Light Harvesting Complex II (LHCII), of which the structure is known from X-ray diffraction on similar crystals. Analysis of spectral properties and structure of the crystals yielded important insights in the process of nonphotochemical quenching (NPQ). The insights were supplemented by studies of aggregated LHCII, and LHCII under high hydrostatic pressure. The largest photosynthetic pigment-protein complex to be crystallized to date (PSI-LHCI) was also studied. A minor light-harvesting complex (CP29), which may be important for NPQ, and which has eluded crystallization, was studied by site-directed fluorescent labeling combined with FRET to obtain structural information. This summarizing discussion first treats CP29 (section 7.2), then LHCII and NPQ (section 7.3), and finally PSI (section 7.4). The general conclusions are in section 7.5, followed by the recommendations for future study.

7.2 Streak camera setup: Structure of CP29

A valuable detection method of time-resolved fluorescence is the synchroscan streak camera system. Such a setup was built, using a set of lasers and amplifiers of Coherent (U.S.A.), a spectrograph of Chromex (U.S.A.) and a streak camera of Hamamatsu (Japan). Chapter 2 describes the details of the setup, and analysis of the data obtained with it. In Chapter 3 the value of the setup is illustrated for CP29. CP29 is one of the minor light-harvesting complexes of PSII. Its exceptionally long N-terminal domain[1] is phosphorylated[2] under cold stress-induced photoinhibition[3]. Phosphorylation leads to spectral changes, that were assigned to conformational changes of the transmembranal part of CP29[4]. Later CP29 was suggested to be a site for quenching during NPQ[5], and in *Arabidopsis thaliana* plants that lack CP29 (and CP24) NPQ is decreased compared to wild type plants[6]. The structure of CP29 has not been resolved, however the high sequence homology with LHCII, especially in the transmembrane domain, suggests an organization similar to that of LHCII, the structure of which has been obtained at 2.5-2.72 Å[7,8]. However, no information is available about the organization of the N-terminal domain,

which differs completely from that of LHCII. In Chapter 3 specific amino acids in the tail were replaced by a cysteine, which was then labeled with a rhodamine type dye (TAMRA), which can be selectively excited around 530-550 nm. Förster resonance energy transfer was measured from TAMRA to the Chl molecules, providing information about distances between specific sites of the N-terminal domain and the chlorophyll molecules. The N-terminal domain seems to fold back to the transmembranal part of CP29. Although these results require further substantiation, the experiments demonstrate the feasibility of this approach to study protein structure.

7.3 Nonphotochemical quenching and LHCII

Nonphotochemical quenching is an important mechanism that plants and algae use to prevent photodamage under conditions of high light intensity[9]. It has been proposed to take place in LHCII[10-13] (or CP29[5], see above). An unresolved issue is the mechanism of quenching. Currently there are two views: (i) quenching occurs via energy transfer from Chl *a* to Lut and subsequent rapid relaxation to the ground state[13]; (ii) quenching occurs via cation radical formation by charge separation in a Chl-Zea dimer, and subsequent rapid relaxation to the ground state[14]. Both candidates have in common that a light-harvesting complex (LHC) can switch between a state with a long excited-state lifetime, and a state in which this lifetime is reduced. Chapters 1, 4 and 5 describe experiments on this switching in LHCII.

Aggregation of LHCII *in vitro* leads to fluorescence quenching that is very similar to that observed *in vivo* under conditions of NPQ[15,16]. Therefore aggregated LHCII has been used extensively as a model system for studying the role of LHCs in NPQ[10,17-20]. However, it is still unknown whether LHCII aggregation leads to the formation of quenchers (excitation traps), as proposed for instance by Horton et al.[11,19], or that increased connectivity between trimers upon aggregation leads to efficient quenching by a small population of permanently quenched LHCII[21,22]. If quenchers are formed, the question remains whether strong quenchers form in a small fraction of LHCII[18], or whether weaker quenchers form in a large fraction of LHCII[11]. In Chapter 4 excited-state lifetimes of monomers, trimers and aggregates of LHCII are compared. The quenching in aggregates was so strong, that it could not be explained quantitatively by enhanced trapping by quenchers that were present before aggregation. So quenchers are created upon aggregation. These quenching traps do not only trap excitations in the trimer in which they are located, but also excitations originating in complexes that do not contain traps themselves. The

fluorescence quenching in monomers was found to be even stronger than that in trimers, suggesting an intramonomeric origin of this process.

In Chapter 5 hydrostatic pressure was used to study the switching between quenched/unquenched states of LHCII. At atmospheric pressure a small fraction of isolated LHCII is quenched, and this fraction is in thermodynamic equilibrium with the bulk unquenched fraction[23]. Applying high hydrostatic pressure shifts the equilibrium more to the quenched conformation and this allows determination of the energy difference between both states and the change in volume. The volume difference between the two states is very small: 5 ml/mol; less than 0.006% of the volume of one trimeric LHCII complex, which indicates a local conformational switch between the two states. The switch is accompanied by a small change in energy: 7.0 kJ/mol; high enough to keep the quenched state population low under normal conditions, but low enough to switch in a controlled way by environmental changes (such as pH, membrane structure, aggregation) induced by high light intensities.

In addition, at high pressure a state forms that is approximately 100-fold more quenched than the other two states. This state has a fluorescence lifetime of ~25 ps, reflecting the average time to reach an extremely efficient quencher somewhere within the trimer (the excitation equilibration time)[24]. At 400 MPa (4 kbar) less than 1% of all Chls are highly quenched, whereas in LHCII in which the pigments were uncoupled by detergent treatment this was 47%. These pressure experiments demonstrate that at least two types of quenchers can be formed in LHCII *in vitro*, very strong and relatively weak ones. *In vivo* a small number of strong quenchers could quench fluorescence of many connected LHCs. Alternatively a large number of weak quenchers could lead to the same amount of quenching.

A third approach to gain insight in the switching of LHCII between quenched and unquenched states involves the study of crystals of LHCII, as described in Chapter 1 and by Pascal et al.[12]. The crystal structure of LHCII from spinach at 0.272 nm[7] aided in the understanding of its spectroscopic features; extensive modeling based on this structure explained many steady-stated and time-resolved spectral properties of LHCII in solution[25]. It is not known *a priori*, however, whether the structure of LHCII is the same when LHCII is dissolved in buffer, and when it is crystallized. This is particularly relevant, because LHCII has the ability to switch between conformations with different fluorescence lifetimes[10,17,18]. Fluorescence lifetime imaging microscopy showed that the fluorescence lifetime of LHCII crystals was ~850 ps. When the crystals were dissolved the fluorescence lifetime switched to ~4 ns. Subsequent aggregation switched LHCII back to a quenched state, with a lifetime of ~650 ps (Chapter 1 and ref. [12]). Thus, it is clear that the crystal structure does not correspond to the unquenched state of LHCII, but more resembles the

quenched state of aggregated LHCII, and/or that of LHCII under hydrostatic pressure. Also the Raman and low-temperature fluorescence emission spectra of the crystals differed from those of LHCII in solution[12]. Those differences indicated a higher degree of homogeneity and stronger twisting of the Neo in the crystals as compared to LHCII in solution. Also the interactions of Chls *b* and their environment are different. The crystal packing was not dense enough to induce these changes directly by trimer-trimer interactions, nor can the quenching be caused by intertrimeric pigment interactions. Therefore the quencher must be sought for inside the trimeric units. Based on the crystal structure[7], two sites were proposed: a Chl *a* dimer in close proximity of a Lut, and a Chl *b* close to Neo. It was later confirmed that in aggregated LHCII excited-state energy is transferred from Chl to Lut, supporting the role of Lut in fluorescence quenching in the crystals[13].

7.4 Photosystem I

The structural and spectral differences between LHCII in crystal form and in solution triggered the study of PSI-LHCI crystals in Chapter 6. PSI-LHCI is a pigment-protein complex that is more complicated than LHCII: PSI-LHCI binds more pigments (~160 vs. 42), it performs photochemical quenching, and it contains "red Chls", with an excited-state energy lower than that of the reaction centre[26]. The fluorescence decay is rather complex due to the presence of energetically coupled Chls with very different excited-state energies. The excited-state energy of the Chls and their coupling may depend on plant species, preparation method and measuring conditions[27-33]. Consequently, a wide range of fluorescence decay kinetics have been reported over the years[27-33]. In Chapter 6 it is shown that the picosecond fluorescence of intact crystals is identical to that of dissolved crystals, but differs considerably from most kinetics presented in literature[27-33]. Caution should therefore be taken in using the crystal structure to model those kinetics.

The data of dissolved crystals were described quantitatively by a simple model that required only two pigment clusters: PSI core and LHCI. This model yielded rates of photosynthetic trapping from the core, and wavelength-dependent excitation energy transfer from LCHI to PSI core and *vice versa*. The model differs from previous models with respect to the reduced number of pigment clusters, and the introduction of the wavelength-dependence of the transfer rates. The modeling yields spectra and rate constants that originate specifically from excitation of pigments in PSI core or LHCI, and can therefore serve as a starting point for detailed modeling at the molecular level, using the PSI-LHCI crystal structure.

7.5 General conclusions

This thesis presents important information on the mechanisms by which LHCII (or LHCs of PSII in general) can contribute to NPQ. Better understanding of this photoprotective process may in time lead to strategies to increase crop yields and/or plant fitness. It may further aid systems that mimic photosynthesis *in vitro*, aiming at energy production. The experiments with LCHII crystals showed that its crystal structure was that of a quenched conformation, as compared to LHCII in buffer. Next it was shown that upon aggregation of LHCII quenchers are formed, which consequently also quench fluorescence of LHCII trimers without quenchers. Under high hydrostatic pressure, two quenching mechanisms were observed: (i) Strong quenching, limited by the excitation equilibration time of a trimeric unit; and (ii) weaker quenching, caused by a conformational change that is associated with very small energy and volume changes. These results mark the broad dynamic range of quenching that LHCII can undergo. With CP29, a start has been made to study the structure of its N-terminal domain, which is phosphorylated under stress.

This thesis further deals with the aptness of using X-ray crystal structures to model spectral properties of pigment-protein complexes. Often it is tacitly assumed that the structure of these complexes is the same in solution and in crystal form. For LHCII this assumption is not completely valid, because the fluorescence of LHCII crystals is quenched as compared to that of LHCII in solution. For PSI-LHCI the fluorescence decay was identical for crystals and dissolved crystals. The decay was however different from most of those reported before, and the crystal structure may not be suited to model those data. A new type of model provides a simple description of the fluorescence kinetics, based on only two compartments and wavelength-dependent excited-state energy transfer among them. The experiments on these crystals illustrate the need of caution when using crystal structures to model specific spectral parameters of pigment-protein complexes.

7.6 Recommendations

7.6.1 CP29 structure

With regard to the study of the structure of the N-terminal tail of CP29 I recommend the following:

1. More detailed structural information can be obtained by using more labeling positions.
2. The effect of the fluorescent label on the structure should be checked, by comparing, for example, (low temperature) linear and circular dichroism, with and without label attached.

3. Another label can be used, for example a smaller fluorescent label, or a paramagnetic label for electron paramagnetic resonance (EPR) experiments.
4. The N-terminal domain of CP29 is phosphorylated under stress[3]. Therefore it would be interesting to study the effect of phosphorylation on the structure of this domain. If *in vitro* phosphorylation is impossible, its effect may be mimicked by introduction of a negatively charged amino acid.

7.6.2 Nonphotochemical quenching and LHCII

With regard to the study of LHCII as a model system of nonphotochemical quenching *in vivo*, I recommend the following:

1. Chapter 5 shows that hydrostatic pressure can be used to controllably and reversibly switch LHCII between quenched and unquenched states. This switching can now be studied by many other spectroscopic methods to gain insight in the quenching mechanism.
2. Most experiments on isolated LHCII have been done with micellar systems, where individual monomers or trimers are solubilized by detergent molecules. *In vivo* LHCII is in a crowded membrane, which is a quite different environment. The *in vivo* state can be mimicked by reconstitution of LHCII in lipid vesicles (as done by Moya et al.[23]). The effect of crowding can be studied by changing the protein/lipid ratio of the vesicles. Optical and structural properties of LHCII should be studied in such vesicles. Also the experiments on CP29 could be repeated in lipid vesicles. The structure of the N-terminal domain may be affected by the membrane via steric hindrance or electrostatic interactions.
3. *In vivo* the pH gradient across the photosynthetic membrane is required for full NPQ. Indeed, lowering pH induces fluorescence quenching of isolated LHCII[19]. However, *in vivo* the formation and relaxation of qE and ΔpH occur with different kinetics[34]. With LHCII in lipid vesicles a pH gradient can be applied across the membrane (ideally all LHCII units in a vesicle should be oriented with the same side to the interior). Then the quenching effect of the gradient can be studied in detail in a system that is more *in vivo*-like than LHCII in micelles.
4. Study how connectivity of photosynthetic units in the native membrane influences the effect of quenchers. Native photosynthetic membranes are densely packed[35], enabling energy transfer among photosynthetic complexes, which results in migration of excitation energy through multiple complexes. A quencher is more effective in a highly connected network of pigments than in a weakly connected network[21]. The connectivity is related to the speed of excited-state energy migration, but this speed is still under debate[36-38], and may change in response to a plant's environment[39,40]. Knowledge about

the connectivity will therefore help to understand to which extent fluorescence quenching of individual LHCs can contribute to the overall quenching *in vivo*. Connectivity should be measured (using rapid fluorescence induction[41]) in unquenched samples and during NPQ formation.

7.6.3 Photosynthetic pigment-protein crystals

With regard to the study of crystals of photosynthetic pigment-protein complexes, I recommend the following:

1. The use of total internal reflection microscopy instead of confocal microscopy, to avoid reabsorption effects.
2. Study other (optical and electronic) properties than fluorescence lifetimes. A start has been made with measuring Raman and fluorescence spectra of LHCII[12], variable fluorescence and electron transfer rates in cyanobacterial PSII cores[42], EPR spectroscopy of cyanobacterial PSI[43] and PSII[44] cores. Such experiments can give more insight in which properties of pigment-protein complexes are conserved in crystals and which differ from those of the same complexes in solution. Further experiments are then required to compare those properties with those of the complexes *in vivo*.
3. "Manipulate" crystals, and measure the effect on optical and electronic properties. For example, it is possible to infiltrate photosynthetic crystals with chemicals such as DCMU[42] (which inhibits Q_A to Q_B electron transfer). Crystals can be "manipulated" in many other ways, such as by magnetic or electric fields or by light. Also temperature can be varied (note that X-ray diffraction experiments are generally performed at cryogenic temperatures). Measurements of pigment-protein complex properties under these different conditions can aid the comparison with the complexes in solution and *in vivo*.

7.6.4 Crystals of biomolecules

The question whether a structure obtained by X-ray crystallography is the same as that in solution, is appropriate for many biomolecules, not just photosynthetic proteins. Often it is tacitly assumed that the structure is the same in crystal and solution. This is not always true for pigment-protein complexes (see LHCII). Also the fluorescence of several fluorescent proteins of the GFP family is quenched compared to that of the same proteins in solution[45]. Also the fluorescence of ethidium bromide bound to DNA is quenched more in crystals than in solution[45]. Therefore a systematic comparison of spectroscopic and structural

properties of many types of biomolecules in crystal and in solution can provide valuable missing information.

7.6.5 Photosynthesis research in broader perspective

The production of enough food to feed and energy to power the world's growing population are key issues of our society. At this moment all food, and most energy, originates from biomass (either directly from "fresh" biomass (~14%) or indirectly from fossil biomass, e.g. oil, coal, gas (~74%)[46]). The growth of the world's population and its increasing prosperity, boost the demand for food and energy. Meanwhile the amount of easily-accessible natural reserves of fossil fuels is decreasing, and CO_2 released by burning fossil fuels is proposed to contribute to climate changes[47]. Therefore alternative energy sources are required.

A wide range of energy sources is available, for example energy from biomass, wind energy, tidal energy and energy from nuclear fission. Each of these has its own advantages and disadvantages. The main advantages of energy from biomass is that biomass production uses an abundant energy source (the sun) and existing production facilities (i.e. photosynthetic organisms). Disadvantages of biomass production are (i) competition with food production; (ii) requirement of fresh water, which becomes increasingly scarce; and (iii) requirement of large areas of arable land. (Note that the use of algae can overcome some of these disadvantages, but that requires a more complex capital intensive production than the use of plants.)

Most biomass is produced by photosynthesis[46]. Improving the efficiency of photosynthesis may overcome some of the disadvantages of biomass production. Three paths may lead to such an increase of efficiency: (i) reduction of losses in light-to-fuel conversion; (ii) conversion of solar energy directly into fuel; (iii) realization of artificial devices that perform better than the natural system. Future photosynthesis research should aim at the knowledge required to follow these paths.

References

1. Bassi, R., Sandona, D. and Croce, R. (1997), *Physiol. Plant.* **100**, 769-779.
2. Testi, M. G., Croce, R., Polverino-De Laureto, P. and Bassi, R. (1996), *FEBS Lett.* **399**, 245-250.
3. Bergantino, E., Dainese, P., Cerovic, Z., Sechi, S. and Bassi, R. (1995), *J. Biol. Chem.* **270**, 8474-8481.
4. Croce, R., Breton, J. and Bassi, R. (1996), *Biochemistry* **35**, 11142-11148.
5. Ahn, T. K., Avenson, T. J., Ballottari, M., Cheng, Y.-C., Niyogi, K. K., Bassi, R. and Fleming, G. R. (2008), *Science* **320**, 794-797.
6. Andersson, J., Walters, R. G., Horton, P. and Jansson, S. (2001), *Plant Cell* **13**, 1193-1204.

7. Liu, Z. F., Yan, H., Wang, K., Kuang, T., Zhang, J., Gui, L. and Chang, W. (2004), *Nature* **428**, 287-292.
8. Standfuss, J., Terwisscha van Scheltinga, A. C., Lamborghini, M. and Kühlbrandt, W. (2005), *EMBO J.* **24**, 919-928.
9. Niyogi, K. K. (1999), *Annu. Rev. Plant. Physiol. Plant Mol. Biol.* **50**, 333-359.
10. Horton, P., Ruban, A. V., Rees, D., Pascal, A. A., Noctor, G. and Young, A. J. (1991), *FEBS Lett.* **292**, 1.
11. Horton, P., Wentworth, M. and Ruban, A. V. (2005), *FEBS Lett.* **579**, 4201-4206.
12. Pascal, A. A., Liu, Z. F., Broess, K., van Oort, B., van Amerongen, H., Wang, C., Horton, P., Robert, B., Chang, W. R. and Ruban, A. (2005), *Nature* **436**, 134-137.
13. Ruban, A. V., Berera, R., Ilioaia, C., van Stokkum, I. H. M., Kennis, J. T. M., Pascal, A. A., van Amerongen, H., Robert, B., Horton, P. and van Grondelle, R. (2007), *Nature* **450**, 575-578.
14. Holt, N. E., Zigmantas, D., Valkunas, L., Li, X.-P., Niyogi, K. K. and Fleming, G. R. (2005), *Science* **307**, 433-436.
15. Ruban, A. V. and Horton, P. (1999), *Plant Physiol.* **119**, 531-542.
16. Ruban, A. V., Young, A. and Horton, P. (1994), *Biochim. Biophys. Acta* **1186**, 123-127.
17. Ruban, A. V. and Horton, P. (1992), *Biochim. Biophys. Acta* **1102**, 30.
18. Mullineaux, C. W., Pascal, A. A., Horton, P. and Holzwarth, A. R. (1993), *Biochim. Biophys. Acta* **1141**, 23-28.
19. Ruban, A. V., Young, A. and Horton, P. (1994), *Biochim. Biophys. Acta* **1186**, 123-127.
20. Bassi, R. and Caffarri, S. (2000), *Photosynth. Res.* **64**, 243-256.
21. den Hollander, W. T. F., Bakker, J. G. C. and van Grondelle, R. (1983), *Biochim. Biophys. Acta* **725**, 492-507.
22. Gillbro, T., Sandström, Å., Spangfort, M., Sundström, V. and van Grondelle, R. (1988), *Biochim. Biophys. Acta* **934**, 369-374.
23. Moya, I., Silvestri, M., Vallon, O., Cinque, G. and Bassi, R. (2001), *Biochemistry* **40**, 12552-12561.
24. Barzda, V., Gulbinas, V., Kananavicius, R., Cervinskas, V., van Amerongen, H., van Grondelle, R. and Valkunas, L. (2001), *Bioph. J.* **80**, 2409-2421.
25. Novoderezhkin, V. I., Palacios, M. A., van Amerongen, H. and van Grondelle, R. (2005), *J. Phys. Chem. B* **109**, 10493-10504.
26. Nelson, N. and Yocum, C. F. (2006), *Annu. Rev. Plant Biol.* **57**, 521-565.
27. Croce, R., Dorra, D., Holzwarth, A. R. and Jennings, R. C. (2000), *Biochemistry* **39**, 6341-6348.
28. Engelmann, E., Zucchelli, G., Casazza, A. P., Brogioli, D., Garlaschi, F. M. and Jennings, R. C. (2006), *Biochemistry* **45**, 6947-6955.
29. Ihalainen, J. A., Jensen, P. E., Haldrup, A., van Stokkum, I. H. M., van Grondelle, R., Scheller, H. V. and Dekker, J. P. (2002), *Bioph. J.* **83**, 2190-2201.
30. Ihalainen, J. A., Klimmek, F., Ganeteg, U., van Stokkum, I. H. M., van Grondelle, R., Jansson, S. and Dekker, J. P. (2005), *FEBS Lett.* **579**, 4787-4791.
31. Ihalainen, J. A., van Stokkum, I. H. M., Gibasiewicz, K., Germano, M., van Grondelle, R. and Dekker, J. P. (2005), *Biochim. Biophys. Acta* **1706**, 267-275.
32. Slavov, C., Ballottari, M., Morosinotto, T., Bassi, R. and Holzwarth, A. R. (2008), *Bioph. J.* **94**, 3601-3612.
33. Turconi, S., Weber, N., Schweitzer, G., Strotmann, H. and Holzwarth, A. R. (1994), *Biochim. Biophys. Acta* **1187**, 324-334.
34. Horton, P., Ruban, A. V. and Walters, R. G. (1996), *Annu. Rev. Plant. Physiol. Plant Mol. Biol.* **47**, 655-684.
35. Kirchhoff, H., Tremmel, I., Haase, W. and Kubitscheck, U. (2004), *Biochemistry* **43**, 9204-9213.
36. Kirchhoff, H., Borinski, M., Lenhert, S., Chi, L. and Büchel, C. (2004), *Biochemistry* **43**, 14508-14516.

37. Broess, K., Trinkunas, G., van Hoek, A., Croce, R. and van Amerongen, H. (2008), *Biochim. Biophys. Acta* **1777**, 404-409.
38. van Amerongen, H., Valkunas, L. and van Grondelle, R. 2000. Photosynthetic excitons. World Scientific Publishing, Singapore. 590 p.
39. Anderson, J. M. (1986), *Annu. Rev. Plant Physiol.* **37**, 93-136.
40. Kirchhoff, H., Haase, W., Wegner, S., Danielsson, R., Ackermann, R. and Albertsson, P. A. (2007), *Biochemistry* **46**, 11169-11176.
41. Trissl, H. W. and Lavergne, J. (1995), *Austr. J. Plant. Physiol.* **22**, 183-193.
42. Kargul, J., Maghlaoui, K., Murray, J. W., Deak, Z., Boussac, A., Rutherford, W. A., Vass, I. and Barber, J. (2007), *Biochim. Biophys. Acta*.
43. Kamlowski, A., van der Est, A., Fromme, P. and Stehlik, D. (1997), *Biochim. Biophys. Acta* **1319**, 185-198.
44. Kammel, M., Kern, J., Lubitz, W. and Bittl, R. (2003), *Biochim. Biophys. Acta* **1605**, 47-54.
45. Royant, A., Carpentier, P., Ohana, J., McGeehan, J., Paetzold, B., Noirclerc-Savoye, M., Vernede, X., Adam, V. and Bourgeois, D. (2007), *J. Appl. Cryst.* **40**, 1105-1112.
46. Archer, M. D. and Barber, J. 2004. Photosynthesis and photoconversion. In Molecular to global photosynthesis, editors: Archer, M. D. and Barber, J., Imperial College Press, London. p. 1-41.
47. IPCC, 2007: Climate Change 2007: The Physical Science Basis. Contribution of Working Group I to the Fourth Assessment Report of the Intergovernmental Panel on Climate Change. editors: Solomon, S., Qin, D., Manning, M., Chen, Z., Marquis, M., Averyt, K. B., Tignor, M. and H.L., M. Cambridge University Press, Cambridge, United Kingdom and New York, NY, USA. 996 p.

Chapter 8

Nederlandse samenvatting

8.1 Inleiding

Dit proefschrift beschrijft tijdsopgeloste fluorescentie van fotosynthetische pigment-eiwit complexen. Fluorescentie is een proces waarbij licht wordt uitgezonden na lichtabsorptie. Het fluorescentiesignaal bevat informatie over structuur en dynamica van pigment-eiwit complexen, zowel *in vitro* als *in vivo*.

Eiwitstructuur kan gemeten worden met röntgendiffractie aan eiwitkristallen. Een probleem hierbij is dat het onduidelijk is of de structuur van deze eiwitten in oplossing gelijk is aan die in een kristalrooster. Daarom is fluorescentie gemeten van Light-Harvesting Complex II (LHCII) kristallen, en van LHCII oplossing (Hoofdstuk 1). Deze experimenten zijn aangevuld met metingen aan aggregaten van LHCII en aan LHCII onder hydrostatische druk. De structuur van CP29, een eiwit dat sterk op LHCII lijkt, is bestudeerd met behulp van fluorescente labels. Tenslotte is fluorescentie van Photosystem I-Light-Harvesting Complex I (PSI-LHCI) kristallen bestudeerd. In deze samenvatting worden achtereenvolgens CP29 (paragraaf 8.2), LHCII en NPQ (paragraaf 8.3), en PSI (paragraaf 8.4) besproken. In paragraaf 8.5 staan de belangrijkste conclusies.

8.2 Streak camera opstelling: Structuur van CP29

De synchroscan streak camera is een meetopstelling om tijdsopgeloste fluorescentie te meten. In het kader van deze promotie is een streak camera gebouwd. In hoofdstuk 2 staan de experimentele aspecten en de analyse van meetdata beschreven. In hoofdstuk 3 wordt de waarde van de streak camera geïllustreerd met metingen aan CP29. Dit pigment-eiwit complex lijkt betrokken bij nonphotochemical quenching (NPQ)[1,2], en fosforylering van het N-terminale domein leidt tot spectrale veranderingen[3-5]. De structuur van dit N-terminale domein, dat veel langer is dan in aanverwante eiwitten[6], is bestudeerd door op specifieke plaatsten een rhodamine-type label (TAMRA) te binden, dat selectief kan worden geëxciteerd rond 530-550nm. De gemeten (afstandsafhankelijke) energieoverdracht van TAMRA naar Chl wijst er op dat het N-terminale domein terugvouwt op het transmembraan deel van CP29.

8.3 Nonphotochemical quenching en LHCII

Nonphotochemical quenching (NPQ) is een belangrijk mechanisme dat planten en algen gebruiken om schade door een teveel aan geabsorbeerd licht te voorkomen[7]. NPQ vindt waarschijnlijk plaats in LHCII[8-11] (en/of in CP29[1,2]), en leidt tot een fluorescentie doving

(quenching). Er zijn verschillende ideeën over het mechanisme van de quenching: (i) energieoverdracht van chlorophyl (Chl) naar luteine (Lut), gevolgd door snel verval naar de grondtoestand[11]; en (ii) vorming van een cation radicaal door ladingsscheiding in een Chl-Zea dimeer, gevolgd door snel verval naar de grondtoestand[12]. Bij beide mechanismen kan een LHC "schakelen" tussen toestanden met een langlevende en met een kortlevende Chl aangeslagen toestand. Hoofdstukken 1, 4 en 5 beschrijven experimenten aan dit "schakelen" in LHCII.

Aggregatie van LHCII *in vitro* leidt tot fluorescentie quenching die erg lijkt op de quenching *in vivo* onder NPQ omstandigheden[13,14]. Daarom wordt LHCII veel gebruikt als een *in vitro* modelsysteem om de rol van LHC's in NPQ te bestuderen[8,15-18]. Het is echter onbekend of LHCII aggregatie leidt tot de vorming van quenchers ("traps" voor excitatie-energie), zoals voorgesteld door Horton et al.[9,17], of dat de toegenomen koppeling tussen LHCII trimeren tijdens aggregatie leidt tot efficiënte quenching door een kleine fractie van permanent gequencht LHCII[19,20]. Als er quenchers gevormd worden, dan kan een klein aantal sterke quenchers[16] leiden tot een zelfde mate van quenching als een groter aantal zwakkere quenchers[9].

In hoofdstuk 4 wordt de tijdsopgeloste fluorescentie van LHCII monomeren, trimeren en aggregaten vergeleken. De fluorescentie quenching door aggregatie is zo groot dat deze niet kwantitatief verklaard kan worden door een vergrootte effectiviteit van quenchers die al aanwezig waren voor aggregatie. Dus aggregatie leidt tot de vorming van sterke quenchers, die vervolgens ook de fluorescentie van gekoppelde LHCII eenheden quenchen. In monomeren is de quenching groter dan in trimeren, wat suggereert dat de quencher te vinden is in een monomere eenheid van LHCII, en niet op het grensvlak tussen de drie monomeren in een trimeer.

In hoofdstuk 5 is hydrostatische druk gebruikt om het schakelen van LHCII tussen conformaties met gequenchte en ongequenchte fluorescentie te bestuderen. Bij atmosferische druk is een kleine fractie LHCII gequencht. Deze fractie is in thermodynamisch evenwicht met het ongequenchte LHCII[21]. Onder verhoogde druk verschuift dit evenwicht. Hierdoor is het mogelijk om het energieverschil (7.0 kJ/mol) en het volumeverschil (0.006%) tussen gequencht en ongequencht LHCII te bepalen. Dit kleine conformatieverschil is groot genoeg om er voor te zorgen dat er weinig gequencht LHCII is onder normale omstandigheden, maar klein genoeg er voor om te zorgen dat lichtgeïnduceerde omgevingsveranderingen (zoals pH, eiwitstructuur en aggregatie) kunnen zorgen voor een gecontroleerde schakeling tussen de twee toestanden.

Daarnaast veroorzaakt hoge druk de vorming van LHCII waarvan de fluorescentie ongeveer 100 keer meer gequencht is dan de twee andere vormen. Dit LHCII heeft een fluorescentielevensduur van ~25 ps, wat ongeveer gelijk is aan de vereiste tijd om een extreem efficiënte quencher te bereiken binnen een trimeer[22]. Het aantal quenchers is echter

vrij klein (aangenomen dat er één quencher per trimeer wordt gevormd). Dit aantal is veel groter in LCHII waarin de pigmenten ontkoppeld zijn. De hoge-drukmetingen laten dus zien dat er tenminste twee manieren zijn waarop fluorescentie van LCHII gequencht kan worden: (i) vorming van sterke quenchers, die *in vivo* de fluorescentie van veel gekoppelde LHC's zouden kunnen quenchen; en (ii) schakeling tussen twee conformaties met verschillende fluorescentielevensduren. In geval (ii) is de quenching per trimeer gering, zou zodoende *in vivo* een groter aantal gequenchte trimeren nodig zou zijn.

Een derde benadering om inzicht te krijgen in het schakelen van LCHII betreft het bestuderen van LHCII kristallen, zoals beschreven in hoofdstuk 1, en door Pascal et al.[10]. De kristalstructuur van LHCII van spinazie, met een ruimtelijke resolutie van 0.272 nm[23], leidt tot een beter inzicht in de spectroscopische eigenschappen van LHCII; modellen gebaseerd op de structuur kunnen veel steady-state en tijdsopgeloste spectrale eigenschappen van LHCII in oplossing verklaren[24]. Het is echter niet *a priori* bekend of de structuur van LHCII in kristalvorm identiek is aan die van LHCII in oplossing. Dit is in het bijzonder relevant gezien het vermogen van LHCII om te schakelen tussen conformaties met verschillende fluorescentielevensduren[8,15,16,25].

Metingen met fluorescentie levensduur imaging microscopie toonden aan dat de fluorescentie levensduur van LHCII in kristallen ~850 ps is. Wanneer de kristallen werden opgelost veranderde dit in ~4 ns, om vervolgens door aggregatie te schakelen naar ~650 ps (hoofdstuk 1 en ref. 10). De tijdsopgeloste fluorescentie van LCHII kristallen lijkt dus niet op die van ongequencht LHCII, maar meer op die van LHCII aggregaten, of van LCHII onder hydrostatische druk. Ook de Raman en lage temperatuur fluorescentie emissie spectra van de kristallen verschilden van die van (ongequencht) LHCII in oplossing[10].

De verschillen wijzen op een hogere homogeniteit en een sterkere verbuiging van neoxanthine in de kristallen dan in oplossing. Ook de interacties van Chl *b* met zijn omgeving verschilt. De kristalpakking was niet dicht genoeg om deze structuurverschillen direct te veroorzaken door trimeer-trimeer interacties, noch kan de quenching worden veroorzaakt door intertrimere pigment interacties. Zodoende moet de quencher gezocht worden binnenin de trimere eenheden. Op basis van de kristalstructuur[23] zijn twee posities voorgesteld: een Chl *a* dimeer dicht bij een Lut, en een Chl *b* dicht bij Neo. Latere experimenten wijzen er op dat in geaggregeerd LHCII energie wordt overgedragen van Chl naar Lut, wat de rol van Lut in de fluorescentie quenching bevestigt[11].

8.4 Fotosysteem I

De verschillen van structuur en spectrale eigenschappen van LHCII in kristalvorm en in oplossing, inspireerden het bestuderen van Photosystem I-Light-Harvesting Complex I

(PSI-LHCI) kristallen. PSI-LHCI is een veel complexer pigment-eiwit complex dan LHCII: PSI-LHCI bindt meer pigmenten (160 vs. 42), het is actief in ladingsscheiding en electrontransport, en het bevat "rood Chl" met een lagere aangeslagen toestand energie dan het Chl in het reactie centrum[26]. Door deze complexiteit is ook is de tijdsopgeloste fluorescentie van PSI-LHCI vrij complex. Bovendien kunnen de aangeslagen toestand energieën en de Chl-Chl koppelingen afhangen van plantensoort, isolatiewijze en meetomstandigheden. Zodoende is in de loop der jaren een grote variatie aan fluorescentie kinetieken gepubliceerd[27-33]. In hoofdstuk 6 wordt aangetoond dat de tijdsopgeloste fluorescentie van PSI-LHCI kristallen (van dit preparaat) identiek is aan die van opgeloste kristallen, maar verschilt van de meeste kinetieken uit de literatuur[27-33]. Het is dus belangrijk voorzichtig te zijn bij het gebruiken van de kristalstructuur voor het modelleren van die kinetieken.

De data van de opgeloste kristallen worden kwantitatief beschreven met een eenvoudig model met slechts twee clusters van pigmenten: PSI core en LHCI. Dit model levert de snelheidsconstantes van fotosynthetische trapping in de core en de golflengteafhankelijke energieoverdrachtssnelheid van PSI naar LHCI en *vice versa*. Het model verschilt van eerdere modellen[27-33] wat betreft het aantal clusters van pigmenten, en de golflengteafhankelijkheid van de overdrachtssnelheden. Uit het model kunnen emissiespectra en de fluorescentievervalsnelheden na selectieve excitatie van pigmenten in PSI core of in LCHI worden berekend. Dit kan dienen als uitgangspunt voor het gedetailleerd modelleren van PSI-LHCI spectroscopische eigenschappen, gebruik makend van de kristalstructuur.

8.5 Algemene conclusies

Dit proefschrift levert belangrijke informatie over de mechanismen waarmee LHCII (en andere LHC's van PSII) kunnen bijdragen aan NPQ. Een beter begrip van dit beschermingsmechanisme tegen lichtgeïnduceerde schade kan op termijn leiden tot strategieën om de gewasopbrengsten en/of plant conditie te verbeteren. Het zou eveneens de ontwikkeling kunnen ondersteunen van de systemen die fotosynthese nabootsen *in vitro*, met als doel energieproductie.

De experimenten met LHCII kristallen toonden aan dat de fluorescentie van LHCII in een kristalrooster is gequencht ten opzichte van die van LHCII in oplossing. Dus de kristalstructuur van LHCII is die van een gequenchte conformatie. Vervolgens is aangetoond dat aggregatie van LHCII leidt tot de vorming van quenchers van fluorescentie. Deze quenchers kunnen ook de fluorescentie quenchen van gekoppelde LHCII trimeren die geen quenchers bevatten. Onder hoge hydrostatische druk zijn er twee quenching

mechanismen: (i) sterke quenching, beperkt door de tijd om een extreem efficiënte quencher te bereiken binnen een trimeer; en (ii) zwakkere quenching, veroorzaakt door een conformatieverandering die gepaard gaat met kleine veranderingen van volume en energie. Deze resultaten tonen het brede dynamische bereik aan van de fluorescentie quenching die LHCII kan ondergaan. Met CP29 is een begin gemaakt van het bestuderen van de structuur van het N-terminale deel, dat gefosforyleerd kan worden onder stress.

Dit proefschrift behandelt verder de toepasbaarheid van eiwitstructuren, verkregen met röntgendiffractie aan eiwitkristallen, voor het modelleren van spectrale eigenschappen van pigment-eiwit complexen. Vaak wordt zwijgend aangenomen dat de structuur van deze complexen hetzelfde is in oplossing en in kristalvorm. Voor LHCII is deze aanname niet helemaal geldig (zie boven). Voor PSI-LHCI is het fluorescentieverval identiek voor kristallen en opgeloste kristallen. Het fluorescentieverval verschilt echter van de meeste gerapporteerde data, en daarom is de kristalstructuur wellicht niet geschikt voor het modelleren van die data. Een nieuw type model geeft een eenvoudige omschrijving van de fluorescentie kinetiek, gebaseerd op slechts twee pigment-clusters, met daartussen golflengteafhankelijke energieoverdracht. De experimenten aan deze kristallen geven aan dat een zekere voorzichtigheid moet worden betracht bij het gebruik van kristalstructuren voor het modelleren van spectrale eigenschappen van pigment-eiwit complexen.

8.6 References

1. Ahn, T. K., Avenson, T. J., Ballottari, M., Cheng, Y.-C., Niyogi, K. K., Bassi, R. and Fleming, G. R. (2008), Science 320, 794-797.
2. Andersson, J., Walters, R. G., Horton, P. and Jansson, S. (2001), Plant Cell 13, 1193-1204.
3. Testi, M. G., Croce, R., Polverino-De Laureto, P. and Bassi, R. (1996), FEBS Lett. 399, 245-250.
4. Bergantino, E., Dainese, P., Cerovic, Z., Sechi, S. and Bassi, R. (1995), J. Biol. Chem. 270, 8474-8481.
5. Croce, R., Breton, J. and Bassi, R. (1996), Biochemistry 35, 11142-11148.
6. Bassi, R., Sandona, D. and Croce, R. (1997), Physiol. Plant. 100, 769-779.
7. Niyogi, K. K. (1999), Annu. Rev. Plant. Physiol. Plant Mol. Biol. 50, 333-359.
8. Horton, P., Ruban, A. V., Rees, D., Pascal, A. A., Noctor, G. and Young, A. J. (1991), FEBS Lett. 292, 1.
9. Horton, P., Wentworth, M. and Ruban, A. V. (2005), FEBS Lett. 579, 4201-4206.
10. Pascal, A. A., Liu, Z. F., Broess, K., van Oort, B., van Amerongen, H., Wang, C., Horton, P., Robert, B., Chang, W. R. and Ruban, A. (2005), Nature 436, 134-137.
11. Ruban, A. V., Berera, R., Ilioaia, C., van Stokkum, I. H. M., Kennis, J. T. M., Pascal, A. A., van Amerongen, H., Robert, B., Horton, P. and van Grondelle, R. (2007), Nature 450, 575-578.
12. Holt, N. E., Zigmantas, D., Valkunas, L., Li, X.-P., Niyogi, K. K. and Fleming, G. R. (2005), Science 307, 433-436.
13. Ruban, A. V. and Horton, P. (1999), Plant Physiol. 119, 531-542.
14. Ruban, A. V., Young, A. and Horton, P. (1994), Biochim. Biophys. Acta 1186, 123-127.
15. Ruban, A. V. and Horton, P. (1992), Biochim. Biophys. Acta 1102, 30.

16. Mullineaux, C. W., Pascal, A. A., Horton, P. and Holzwarth, A. R. (1993), Biochim. Biophys. Acta 1141, 23-28.
17. Ruban, A. V., Young, A. and Horton, P. (1994), Biochim. Biophys. Acta 1186, 123-127.
18. Bassi, R. and Caffarri, S. (2000), Photosynth. Res. 64, 243-256.
19. den Hollander, W. T. F., Bakker, J. G. C. and van Grondelle, R. (1983), Biochim. Biophys. Acta 725, 492-507.
20. Gillbro, T., Sandström, Å., Spangfort, M., Sundström, V. and van Grondelle, R. (1988), Biochim. Biophys. Acta 934, 369-374.
21. Moya, I., Silvestri, M., Vallon, O., Cinque, G. and Bassi, R. (2001), Biochemistry 40, 12552-12561.
22. Barzda, V., Gulbinas, V., Kananavicius, R., Cervinskas, V., van Amerongen, H., van Grondelle, R. and Valkunas, L. (2001), Bioph. J. 80, 2409-2421.
23. Liu, Z. F., Yan, H., Wang, K., Kuang, T., Zhang, J., Gui, L. and Chang, W. (2004), Nature 428, 287-292.
24. Novoderezhkin, V. I., Palacios, M. A., van Amerongen, H. and van Grondelle, R. (2005), J. Phys. Chem. B 109, 10493-10504.
25. van Oort, B., Amunts, A., Borst, J. W., van Hoek, A., Nelson, N., van Amerongen, H. and Croce, R. (2008), Bioph. J. in press.
26. Nelson, N. and Yocum, C. F. (2006), Annu. Rev. Plant Biol. 57, 521-565.
27. Croce, R., Dorra, D., Holzwarth, A. R. and Jennings, R. C. (2000), Biochemistry 39, 6341-6348.
28. Engelmann, E., Zucchelli, G., Casazza, A. P., Brogioli, D., Garlaschi, F. M. and Jennings, R. C. (2006), Biochemistry 45, 6947-6955.
29. Ihalainen, J. A., Jensen, P. E., Haldrup, A., van Stokkum, I. H. M., van Grondelle, R., Scheller, H. V. and Dekker, J. P. (2002), Bioph. J. 83, 2190-2201.
30. Ihalainen, J. A., Klimmek, F., Ganeteg, U., van Stokkum, I. H. M., van Grondelle, R., Jansson, S. and Dekker, J. P. (2005), FEBS Lett. 579, 4787-4791.
31. Ihalainen, J. A., van Stokkum, I. H. M., Gibasiewicz, K., Germano, M., van Grondelle, R. and Dekker, J. P. (2005), Biochim. Biophys. Acta 1706, 267-275.
32. Slavov, C., Ballottari, M., Morosinotto, T., Bassi, R. and Holzwarth, A. R. (2008), Bioph. J. 94, 3601-3612.
33. Turconi, S., Weber, N., Schweitzer, G., Strotmann, H. and Holzwarth, A. R. (1994), Biochim. Biophys. Acta 1187, 324-334.

Acknowledgements

Nu dit proefschrift zijn ontknoping nadert, wil ik graag iedereen bedanken die direct of indirect aan zijn voltooiing heeft bijgedragen.

First of all I thank the organizations that made the work possible: Intro2 for letting me take part in their useful and pleasant meetings, courses and workshops. FLIM to FLIN for financing my participation in several courses and meetings. MSCWU for supporting all the microspectroscopy equipment. FOM for paying my salary.

Herbert, bedankt voor je begeleiding, voor de vrijheid die je me liet, voor de mooie monsters die je telkens voor me in handen wist te krijgen, en voor de prettige denksessies waarbij we steeds nieuwe manieren vonden om tegen de data aan te kijken. Sasha, thank you for being my "tele-"supervisor, a living encyclopedia of all NPQ related information, and a source of interesting ideas. Roberta, in the course of my project you became more and more involved, to my great pleasure. I greatly enjoyed our brainstorming data analysis. Er gaat niets boven Groningen!

In the course of my PhD project I had the pleasure of working with many people from all over the world. I would like to thank you all for pleasant collaboration: Roberto Bassi and Tomas Morosinotto (Marseille), Bruno Robert and Andy Pascal (Saclay), Peter Horton (Sheffield), Wenrui Chang (Beijing), Klaus Kemnitz and Marco Vitali (Berlin), Eckhard Hofmann and Silke Johanning (Bochum), James Barber and Joanna Kargul (London), Nathan Nelson and Alexey Amunts (Tel Aviv).

Op technisch vlak heb ik veel geleerd van Arie van Hoek, Jan Willem Borst en Frank de Weerd, bedankt! Sergey, Ivo, Kate, you taught me a lot on data analysis, and made the programs to do it, thank you very much. Rob, met jouw eeuwige enthousiasme en spectroscopische kennis was je altijd een bron van energie en van hoop dat er wat interessants uit experimenten en data analyse zou komen. Ik hoop dat je nog lang blijft genieten van de spectroscopie, het onderzoek en de studenten. Emilie en Marieke, het was een groot plezier jullie te begeleiden. Ruud bedankt voor het vele biochemische werk aan CP29. To all the other people at biophysics: thank you for good times inside and outside university.

Als je gelukkig bent werk je beter, dus wat gelukkig maakt levert een positieve bijdrage aan het boekje. In dat kader wil ik graag de (oud-)Haarweg 193 bewoners bedanken, en de unihockeyers, de acrobaten en het selecte roeiersclubje. Marloes, bedankt voor de mooie tijd, en de hoofdbrekens die je me gaf om EPR te begrijpen. Marjon, als bron van opgewektheid, met een grote bijdrage aan het geluk, en daarmee aan dit boekje: bedankt. Dingen kunnen raar lopen als je even naar de VS gaat....

Ten slotte, het thuisfront. André en Mieke, jullie waren een punt voor rust en relativering wanneer ik te erg aio-de. Bedankt voor jullie pogingen te begrijpen wat ik deed, het uitleggen daarvan was erg leuk. Floor, Pepijn: als het goed is zijn we zometeen drie doctoren. Nu wordt het toch wel tijd voor die gezamenlijke publicatie, waarin we de overlap tussen geografische informatiesystemen, probleemgedrag en fotosynthese laten opbloeien. Samen met Eduard en Barbara hebben jullie me altijd een thuisgevoel gegeven, om frustraties te laten varen, of juist om na te genieten van mooi werk. Ida, Berber, Lars: jullie zijn de volgende generatie. Hopelijk genieten jullie evenveel (of nog meer) van het leven, als dat jullie (groot)ouders en ik nu van jullie genieten.

This work is part of the research programme of the 'Stichting voor Fundamenteel Onderzoek der Materie (FOM)', which is financially supported by the 'Nederlandse Organisatie voor Wetenschappelijk Onderzoek (NWO)'.

List of publications

Peer reviewed journals

- B. van Oort, A. Amunts, J.W. Borst, A. van Hoek, N. Nelson, H. van Amerongen, R. Croce, 2008. Picosecond fluorescence of intact and dissolved PSI-LHCI crystals. *Biophysical Journal, in press.*
- B. van Oort, A. van Hoek, A.V. Ruban, H. van Amerongen, 2007. Aggregation of light-harvesting complex II leads to formation of efficient excitation traps in monomeric and trimeric complexes. *FEBS Letters, vol. 581, p. 3528-3532.*
- B. van Oort, A. van Hoek, A.V. Ruban, H. van Amerongen, 2007. Equilibrium between quenched and nonquenched conformations of the major plant light harvesting complex studied with high-pressure time-resolved fluorescence. *Journal of Physical Chemistry B, vol. 111, p. 7631-7637.*
- M.M.A.E. Claessens, B.F. van Oort, F.A.M. Leermakers, F.A. Hoekstra, M.A. Cohen Stuart, 2007. Bending rigidity of mixed phospholipid bilayers and the equilibrium radius of corresponding vesicles. *Physical Review E, vol. 76, p. 011903-1-6.*
- M.A. Palacios, J. Standfuss, M. Vengris, B.F. van Oort, I.H.M. van Stokkum, W. Kühlbrandt, H. van Amerongen, R. van Grondelle, 2006. A comparison of the three isoforms of the light-harvesting complex II using transient absorption and time-resolved fluorescence. *Photosynthesis Research, vol. 88, p. 269-285.*
- A.A. Pascal, Z. Liu, K. Broess, B. van Oort, H. van Amerongen, C. Wang, P. Horton, B. Robert, W. Chang, A. Ruban, Molecular basis of photoprotection and control of photosynthetic light-harvesting, 2004. *Nature, vol. 436, p. 134-137.*
- M.M.A.E. Claessens, B.F. van Oort, F.A.M. Leermakers, F.A. Hoekstra, M.A. Cohen Stuart, 2004. Charged lipid vesicles: Effects of salts on bending rigidity, stability and size. *Biophysical Journal, vol. 87, p. 3882-3893.*
- B.F. van Oort, E. Tangen, A. Ghosh, 2004. Electronic structure of transition metal isocorrole complexes: A first quantum chemical study. *European Journal of Inorganic Chemistry, vol. 12, p. 2442-2445*

Submitted to peer reviewed journals

- B. van Oort, S. Murali, W. Wientjes, R.B.M. Koehorst, , R.B. Spruijt, A. van Hoek, R. Croce, H. van Amerongen, 2008. Ultrafast resonance energy transfer from a site-specifically attached fluorescent chromophore reveals the folding of the N-terminal domain of CP29.

Book chapter

- I.H.M. van Stokkum, B. van Oort, F. van Mourik, B. Gobets, H. van Amerongen, 2008. (Sub)-Picosecond spectral evolution of fluorescence studied with a synchroscan streak-camera system and target analysis. In *"Biophysical Techniques in Photosynthesis, Volume II",* editors: Aartsma, T. J. and Matysik, J. Springer, Dordrecht. p. 223-240.

Curriculum Vitae

My name is Bart Frederik van Oort. I was born on the first of March 1980, in Oirschot, NL. In 1998 I graduated from Jacob Roelandslyceum, Boxtel. From 1998 to 2004 I studied Molecular Sciences at Wageningen University. My first MSc. thesis was at Physical Chemistry and Colloid Science, where I studied stability and curvature of lipid vesicles. In 2003 I went to the University of Tromsø, Norway. Under the northern lights and the midnight sun, I used quantum chemical calculations to study electronic properties of porphyrin-like molecules, which carry a promise of artificial photosynthesis and novel catalysts. Back in Wageningen, I started work on photosynthesis, with the new professor in biophycics and my future PhD, supervisor Herbert van Amerongen. In 2004 I graduated, and started my PhD project, of which you are now reading the result .

From 2004 to 2008 I carried out my PhD study in the Laboratory of Biophysics, at Wageningen University. I studied various photosynthetic complexes with a variety of optical spectroscopic methods, In addition I built a setup to measure time-resolved fluorescence (streak camera). The results were published as a book chapter and in several peer-reviewed journals. I presented them at several national and international conferences. I took courses on photosynthesis and spectroscopy, supported by the graduate school “Experimental Plant Sciences” and by the EU Marie Curie Training Network “Intro2”. I defended my thesis on 28 October 2008.

Education Statement of the Graduate School
Experimental Plant Sciences

Issued to: Bart van Oort
Date: 28 October 2008
Group: Laboratory of Biophysics, Wageningen University

1) Start-up phase	date
► **First presentation of your project**	
Problems and corrections for measurements on the streak camera setup	Jan 24, 2005
► **Writing or rewriting a project proposal**	
NPQ and supramolecular organisation of PSII: Topics of investigation	Sep 14, 2004
► **Writing a review or book chapter**	
(Sub)-Picosecond Spectral Evolution of Fluorescence Studied with a Synchroscan Streak-Camera System and Target Analysis	Jan 12, 2006
Subtotal Start-up Phase	*13.5 credits**

2) Scientific Exposure	date
► **EPS PhD student days**	
Radboud University Nijmegen	Jun 02, 2005
Wageningen University	Sep 19, 2006
Wageningen University	Sep 13, 2007
► **EPS theme symposia**	
EPS Theme 3 Symposium 2007	Nov 06, 2007
► **NWO Lunteren days and other National Platforms**	
Annual ALW/FOM/VvBF&BT Meeting on Molecular and Cellular Biophysics §	Sep 27-28, 2004
Annual Dutch Meeting on Cellular and Molecular Biophysics §	Oct 11-12, 2005
Biological Dynamics: from Molecules to Cell (KNAW) §	Nov 07-09, 2005
Annual Dutch Meeting on Cellular and Molecular Biophysics §,‡	Oct 09-10, 2006
Annual Dutch Meeting on Cellular and Molecular Biophysics §	Oct 01-02, 2007
ALW Meeting Experimental Plant Sciences §	Apr 07-08, 2008
► **Seminars (series), workshops and symposia**	
Time-Resolved Multispectral Imaging: From Single-Molecule Spectroscopy to Single-Pair FRET	Sep 22, 2005
Charge Separation in Photosystem II (Workshop)	Oct 28-30,2005
Existing models for charge separation in PSII are not consistent with fluorescence data	Nov 18,2005
A study of the structure of spin-labeled photosynthetic reaction centers from Rhodobacter sphaeroides by EPR and molecular dynamics simulations	Dec 19, 2005
Biophysics Day (symposium)	Dec 20, 2005
Global and Target Analysis in Photobiophysics	Apr 13, 2006
Molecular crowding in photosynthetic membranes	May 18, 2006
Seminar series: Structure and dynamics of biomolecules in vitro en in vivo (6 seminars)	Nov 03-Dec 15, 2006
Simulation-based analysis of time-dependent fluorescence measurements	May 23, 2007
Time domain and CP-MAS NMR to study water as a plasticizer in starch based food materials	Jun 18, 2007
Feasibility study on research programs concerning solar based fuel	Jul 12, 2007
From molecule to morphology - Biomechanical principles governing cell morphogenesis	Sep 21, 2007
Physical-chemical aspects of vesicles and vesicles formation & Modulation of membrane organization and function by proteins	Nov 02, 2007
Protein folding in the secretory pathway & Protein folding at the single-molecule level	Nov 09, 2007
Physical aspects of the photosynthesis process	Nov 16, 2007
Photosynthesis as a potential source of direct and efficient fuel production	Nov 16, 2007
The Time and Space Correlated Single Photon Counting Method: Multi-Anode and Crossed-DL Detectors	Nov 19, 2007
Biophysics Day (symposium)	Dec 19, 2007
Membrane protein structure by EPR	Feb 18, 2008
Clean Solar Fuels (workshop)	Jan 31, 2008
► **International symposia and congresses**	
Nonphotochemical Quenching and Photoprotection in Photosystem II (Parsberg, Germany) §	Sep 24-27, 2006
SingleMotor-FLIN - MidTerm Meeting (Magdeburg, Germany) ‡	Mar 23-25, 2007
PS2007 Drymen Satellite meeting: Light Harvesting Systems (Drymen, Scotland) §,‡	Jul 19-22, 2007
14th International Congress of Photosynthesis (Glasgow, Scotland) §	Jul 22-27, 2007
Patterns in Biology: Organisation of Life in Space and Time (Heidelberg, Germany) §	Oct 27-29, 2007
Final meeting Intro2 Marie Curie network (Lanzarote, Spain) ‡	Feb 07-11, 2008
► **Presentations**	
Fluorescence quenching in LHCII can be caused by structural variations §	Sep 27-28, 2004
Structural variations regulate fluorescence lifetimes in photosynthesis §	Oct 11-12 and Nov 07-09, 2005
Protective fluorescence quenching of LHCII ‡	Dec 20, 2005
Conformational transitions cause fluorescence quenching in LHCII §	Sep 24-27, 2006
LHCII can be a conformational switch to regulate fluorescence in photosynthesis ‡	Oct 09, 2006
Simultaneous atomic-force and two-photon fluorescence imaging of biological specimens in vivo ‡	Dec 15, 2006
Fluorescence Lifetime Imaging of crystals of photosynthetic pigment-protein complexes ‡	Mar 23-25, 2007
Fluorescence Lifetime Imaging of crystals of Photosystem I §	Jul 19-27 and Oct 01-02, 2007
Fluorescence Lifetime Imaging of crystals of Photosystem I ‡	Jul 22, 2007
Effect of antenna size on excited state dynamics in photosynthetic membranes §	Oct 27-29, 2007
LHCII: a versatile collector of light ‡	Dec 19 2007
Picosecond fluorescence of photosynthetic crystals ‡	Feb 10, 2008
Effect of antenna size on excited state dynamics in photosynthetic membranes §	Apr 07-08, 2008
Time- and wavelength-resolved fluorescence spectroscopy using synchroscan streak camera system ‡	Jul 01, 2008
► **IAB interview**	Sep 18, 2006
Subtotal Scientific Exposure	*26.6 credits**

3) In-Depth Studies	date
► **EPS courses or other PhD courses**	
Optical and Laser Spectroscopy (VU Laser Centre)	Oct 24-28, 2005
Nonphotochemical Quenching and Photoprotection in Photosystem II (Parsberg, Germany)	Sep 22-24, 2006
Single Particle Electron Microscopy (RUG)	Jan 24-26, 2007
Photophysics, Photochemistry & Photobiology 2007 (HRSMC)	Jun 04-06, 11-12,15, 2007
2nd Hyper-i-net Summer School 2008 (WUR)	Sep 15-19, 2008
► **Individual research training**	
PAM fluorimetry and npq induction and fixation (5 days, Sheffield University)	2005
single-molecule experiments in Klaus Kemnitz' group (Berlin)	Mar 26-27, 2007
Subtotal In-Depth Studies	*7.6 credits**

4) Personal development	date
► **Skill training courses**	
Scientific publishing: An introductory workshop for PhD students and young authors	Oct 12, 2004
Doelgericht werken en plannen	Nov 16 and Dec 09, 2004
Career perspectives	Sep-Oct 2005
Afstudeervak organiseren en begeleiden	Oct 19-20, 2005
Techniques for writing and presenting a scientific paper	Jun 27-30, 2006
Marie Curie individuele beurzen training (SenterNovem/EG-Liaison)	Jun 26, 2008
Loopbaanplanning (several sessions of 1-2 hours)	Jun-Aug 2008
Subtotal Personal Development	*5.4 credits**

TOTAL NUMBER OF CREDIT POINTS*	**52.1**

Herewith the Graduate School declares that the PhD candidate has complied with the educational requirements set by the Educational Committee of EPS which comprises of a minimum total of 30 credits

** A credit represents a normative study load of 28 hours of study*
‡ oral presentation, § poster presentation